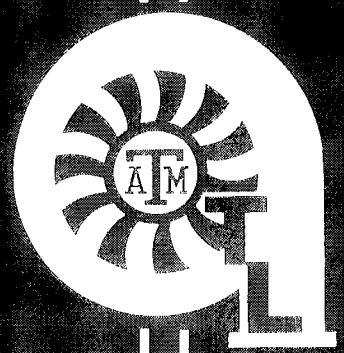

A COMPARISON OF EXPERIMENTAL AND THEORETICAL RESULTS FOR LABYRINTH GAS SEALS WITH HONEYCOMB STATORS

by

Lawrence Allen Hawkins

MASTER OF SCIENCE

TL-SEAL-2-88

May 1988

RECEIVED FEBRUARY 1988

(NASA-CR-182441) A COMPARISON OF EXPERIMENTAL AND THEORETICAL RESULTS FOR LABYRINTH GAS SEALS WITH HONEYCOMB STATORS M.S. Thesis (Texas A&M Univ.) 150 p

N88-16006

Unclas

CSCL 13I G3/37 0121647

Turbomachinery Laboratories
Mechanical Engineering Department
Texas A&M University

A COMPARISON OF EXPERIMENTAL AND THEORETICAL RESULTS FOR LABYRINTH GAS SEALS WITH HONEYCOMB STATORS

A Thesis

by

LAWRENCE ALLEN HAWKINS

Submitted to the Graduate College of
Texas A&M University
in partial fulfillment of the requirements for the degree of

MASTER OF SCIENCE

May 1988

received Feb. 1988

Major Subject: Mechanical Engineering

ABSTRACT

A Comparison of Experimental and Theoretical Results for Labyrinth Gas Seals with Honeycomb Stators. (May 1988)

Lawrence Allen Hawkins, B.S., Auburn University;

Chair of Advisory Committee: Dr. Dara Childs

Experimental results for the rotordynamic stiffness and damping coefficients of a labyrinth-rotor/honeycomb-stator seal are presented. The coefficients are compared to the coefficients of a labyrinth-rotor/smooth-stator seal having the same geometry. The coefficients are also compared to analytical results from a two-control-volume compressible flow model. The experimental results show that the honeycomb stator configuration is more stable than the smooth stator configuration at low rotor speeds. At high rotor speeds and low clearance, the smooth stator seal is more stable. The theoretical model predicts the cross-coupled stiffness of the honeycomb stator seal correctly within 25% of measured values. The model provides accurate predictions of direct damping for large clearance seals. Overall, the model does not perform as well for low clearance seals as for high clearance seals.

PRECEDING PAGE BLANK NOT FILMED

TABLE OF CONTENTS

LIST OF TABLES

LIST OF FIGURES

Page

Page

NOMENCLATURE

A_i	Cross sectional area of control volume (L^2)
B_i	Height of labyrinth seal strip (L)
C, c	Direct and cross-coupled damping coefficients (Ft/L)
Cr	Radial clearance (L)
D	Rotor diameter (L)
D_h	Hydraulic diameter of cavity (L)
F	Seal reaction-force magnitude (F)
K, k	Direct and cross-coupled stiffness coefficients (F/L)
L	Pitch of seal strips (L)
$\dot{m}$	Leakage mass flow rate (M/Lt)
mr, nr	Friction coefficients
ms, ns	
P	Fluid pressure (F/L^2)
R	Gas constant for air (L^2/Tt^2)
Rs_1, Rs_2	Radius of control volumes I & II (L)
T	Fluid temperature (T)
U_1, U_2	Average axial velocity for control volumes I & II (L/t)
W_{1i}, W_{2i}	Average circumferential velocity for control volumes I & II (L/t)
X, Y	Rotor to stator relative displacement components (L)
ν	Kinematic viscosity (L^2/t)
ρ	Density of fluid (M/L^2)
Ω	Shaft precessional velocity $(1/t)$
ω	Shaft angular velocity $(1/t)$

Subscripts

1	Control volume I value
2	Control volume II value
i	i_{th} chamber value
r	Reservoir value, radial component
s	Sump value

CHAPTER I

INTRODUCTION

Modern turbomachines are often subject to the problems of synchronous vibration and instability. Synchronous vibration is caused by an unbalanced rotor. An unbalanced rotor, which whirls at a frequency coincident with its running speed, produces a vibration in the turbomachine at the same (synchronous) frequency. The amplitude of vibration increases as the rotor speed approaches one of its critical speeds. A critical speed is a speed that is coincident with a damped natural frequency of the rotor. The critical speeds and the response of the rotor to unbalance are influenced by forces developed in the rotor bearings and to a limited extent by forces developed in labyrinth seals.

A second, less frequent type of vibration that can occur in high-performance turbomachines is subsynchronous vibration. This vibration is characterized by a rotor whirling at a natural frequency that is less than the rotational speed. Subsynchronous vibration is usually *unstable* or *self-excited*. This type of motion typically appears suddenly at some threshold speed with large amplitude which sustains or grows as running speed is increased. This type of vibration often results in catastrophic failure. The excitation mechanism for subsynchronous vibration is a tangential force acting on the rotor in its whirl direction. Labyrinth gas seals can produce this type of force.

Forces developed in labyrinth seals are characterized by the rotordynamic stiffness and damping coefficients. The first systematic test program for measuring these coefficients was performed at at the Technical University of Stuttgart

by Benckert and Wachter [1,2,3]. Stiffness data were published for three types of seals: a) teeth-on-stator, b) teeth on the rotor and stator, and c) teeth on the stator and steps or grooves on the rotor. Wright [4] has published data on equivalent radial and tangential stiffnesses for single-cavity teeth-on-stator seals. Childs and Scharrer [5] have investigated teeth-on-rotor and teeth-on-stator labyrinth seals at Texas A&M University. They measured stiffness and damping coefficients while varying inlet tangential velocity, rotor speed, inlet pressure, and clearance.

The first analysis of the labyrinth seal was performed by Alford [6]. Kostyuk [7] performed the first comprehensive analysis – using a control volume approach to derive governing equations for flow in the seal. Several authors, notably Iwatsubo [8], Gans [9], and Childs and Scharrer [10] added various refinements to the Kostyuk analysis in order to account for unmodeled effects. A two control volume analysis of the labyrinth seal was introduced by Fujikawa et al. [11]. Refinements to this model have been added by Wyssmann et al. [12] and Scharrer [13].

This report presents experimental measurements of stiffness and damping coefficients for a teeth-on-rotor labyrinth seal with a honeycomb stator. Inlet circumferential velocity, inlet pressure, rotor speed, and seal clearance are varied. Collected data are compared to the data of Scharrer [13] for teeth-on-rotor labyrinth seals with smooth stators. The data are also compared to theoretical predictions using Scharrer's analysis.

The labyrinth-rotor/honeycomb-stator configuration was chosen for several reasons. This combination is a common industrial application, particularly for gas turbine engine hot-section seals. No test data for this combination exists in

the published literature. Finally, the results of Elrod and Childs [14] indicate that seals with honeycomb stators may have a stability advantage over smooth stator seals.

CHAPTER II

SEAL ANALYSIS

SEAL ANALYSIS OVERVIEW

As related to rotordynamics, seal analysis has the objective of determining the reaction forces acting on the seal rotor arising from shaft motion within the seal. For small motion about a centered position, as shown in figure 1, the model of equation (1) describes the force-motion relationship

$$-\begin{Bmatrix} F_X \\ F_Y \end{Bmatrix} = \begin{bmatrix} K & k \\ -k & K \end{bmatrix} \begin{Bmatrix} X \\ Y \end{Bmatrix} + \begin{bmatrix} C & c \\ -c & C \end{bmatrix} \begin{Bmatrix} \dot{X} \\ \dot{Y} \end{Bmatrix} \tag{1}$$

where the rotordynamic coefficients K, k, C, and c represent the direct stiffness, cross-coupled stiffness, direct damping, and cross-coupled damping respectively. The cross-coupling terms result when motion in one plane results in a reaction in an orthogonal plane. These cross-coupling terms depend on the magnitude and direction of the fluid circumferential velocity relative to the rotor's surface velocity. This velocity may exist at entry to the seal or may develop as the fluid passes through the seal.

Stability Analysis

Figure 2 shows the relationship of the seal forces for the simple case of a rotor in a circular synchronous whirl orbit of amplitude A. The X and Y components of force in the seal model of equation (1) may be resolved into radial and tangential forces

$$F_r = \quad F_X \cos \omega t + F_Y \sin \omega t$$

$$F_t = -F_X \sin \omega t + F_Y \cos \omega t$$

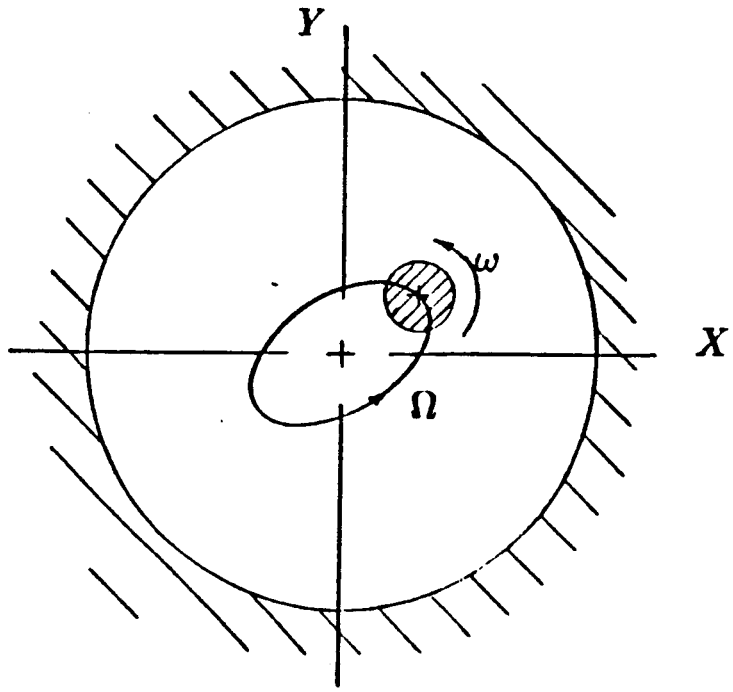

Figure 1. Small motion of a seal rotor about a centered position. The rotor spin speed is ω and the precessional frequency is Ω.

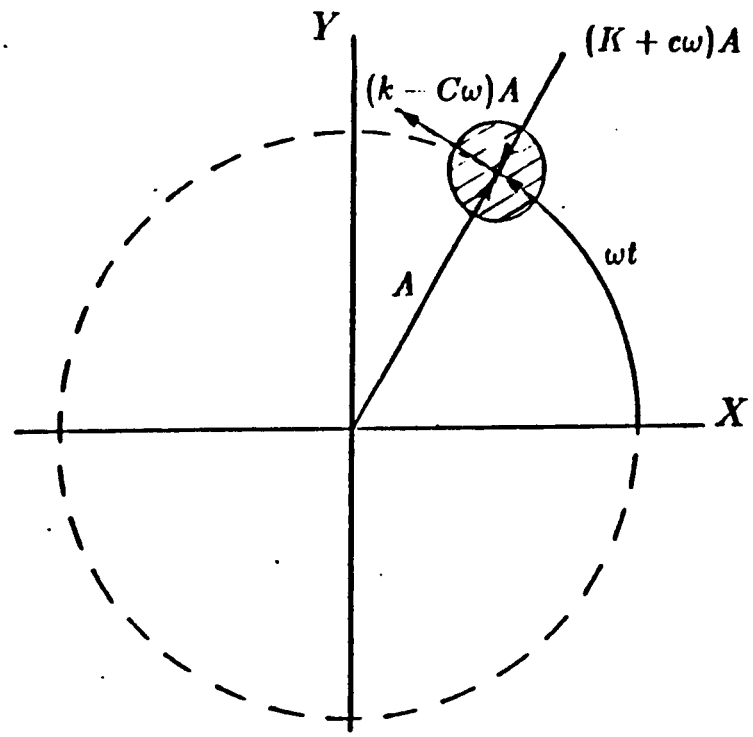

Figure 2. Forces on a precessing seal rotor.

Expressing the rotor motion as

$$X = A\cos\omega t \qquad \dot{X} = -A\omega\sin\omega t$$

$$Y = A\sin\omega t \qquad \dot{Y} = \quad A\omega\cos\omega t$$

and using equation (1), the resultant radial and tangential forces are illustrated in the figure and are defined by

$$-F_r/A = K + c\omega$$

$$F_t/A = k - C\omega$$

If F_t/A is a positive quantity, the tangential force is destabilizing since it supports the whirling motion of a forward whirling rotor. Conversely, if F_t/A is negative, it opposes the whirling motion of a forward whirling rotor, and is therefore stabilizing. Both k and C are positive for most practical labyrinth seal applications; hence, the most compelling reason for determining the rotordynamic seal coefficients is to determine the relative values of k and C. The whirl frequency ratio, defined by

$$Whirl\ frequency\ ratio = k/C\omega,$$

is the parameter commonly used to compare k and C. From the above discussion, if the whirl frequency ratio is less than one, the tangential force on the rotor is stabilizing.

If the sum, $K+c\omega$, is positive then the radial seal force increases the stiffness of the system, raising the critical speeds. This improves the stability of the system. The direct stiffness of a labyrinth seal is usually negative and considerably larger than $c\omega$; therefore, the radial force in a labyrinth seal decreases system stability. Fortunately, the effect of labyrinth seal stiffness on critical speeds is usually small, but there are situations in which seal stiffness is of consequence.

SCHARRER'S ANALYSIS

Most early attempts to model the flow field in a labyrinth seal used a single control volume, concentrating on the circumferential flow components. However, Iwatsubo [15] has shown that the labyrinth seal has two distinct flow regimes: a jet flow region in the leakage path and a recirculation region in the cavity (see figure 3). Hence, Fujikawa et al. [11], Wyssmann et al. [12], and Scharrer [13] have developed two-control-volume models to take advantage of the known physics of the flow. Scharrer's model is used in this report to generate theoretical predictions to compare to experimental data.

Scharrer modeled the flow using the two-control-volume model shown in figures 4 and 5. Scharrer's model includes the recirculation velocity (U_2) as shown in figure 4. The governing equations are derived using the following assumptions:

1) The fluid is an ideal gas.

2) Pressure variations within a chamber are small compared to the pressure difference across a seal strip.

3) The lowest frequency of acoustic resonance in the cavity is much higher than that of the rotor speed.

4) The eccentricity of the rotor is small compared to the radial seal clearance.

5) Although the shear stress is significant in the determination of the flow parameters (velocity, etc.), the contribution of the shear stress to the force on the rotor is negligible when compared to the pressure force.

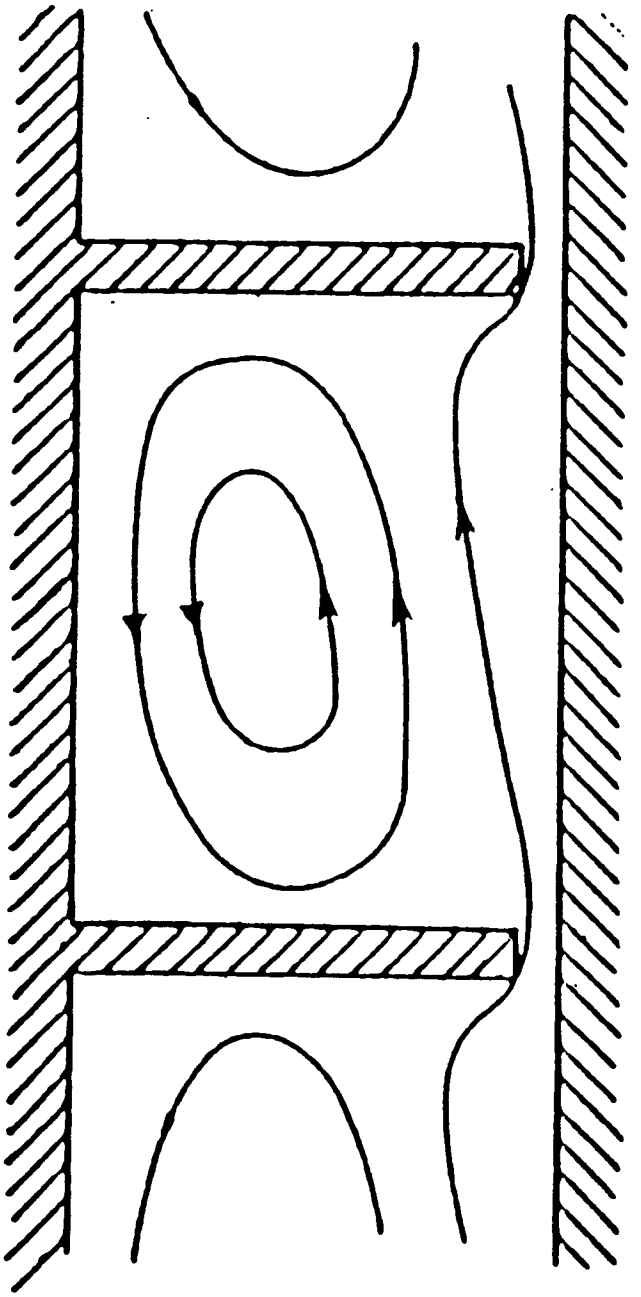

Figure 3. Flow pattern in a labyrinth seal cavity.

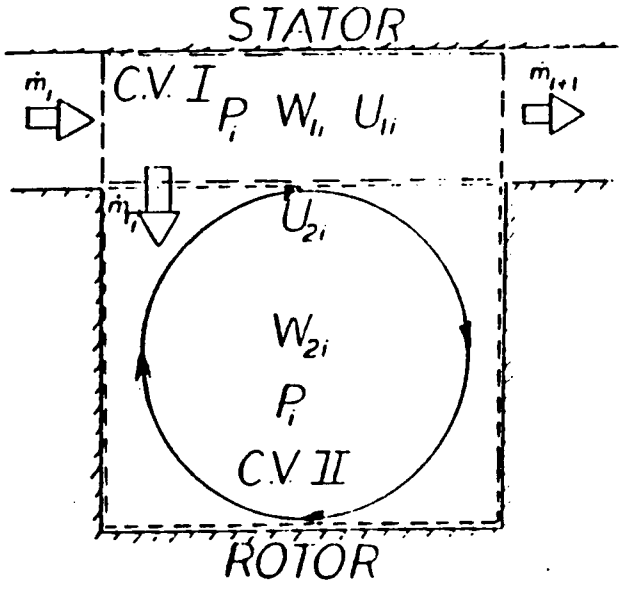

Figure 4. Two-control-volume model of Scharrer [13].

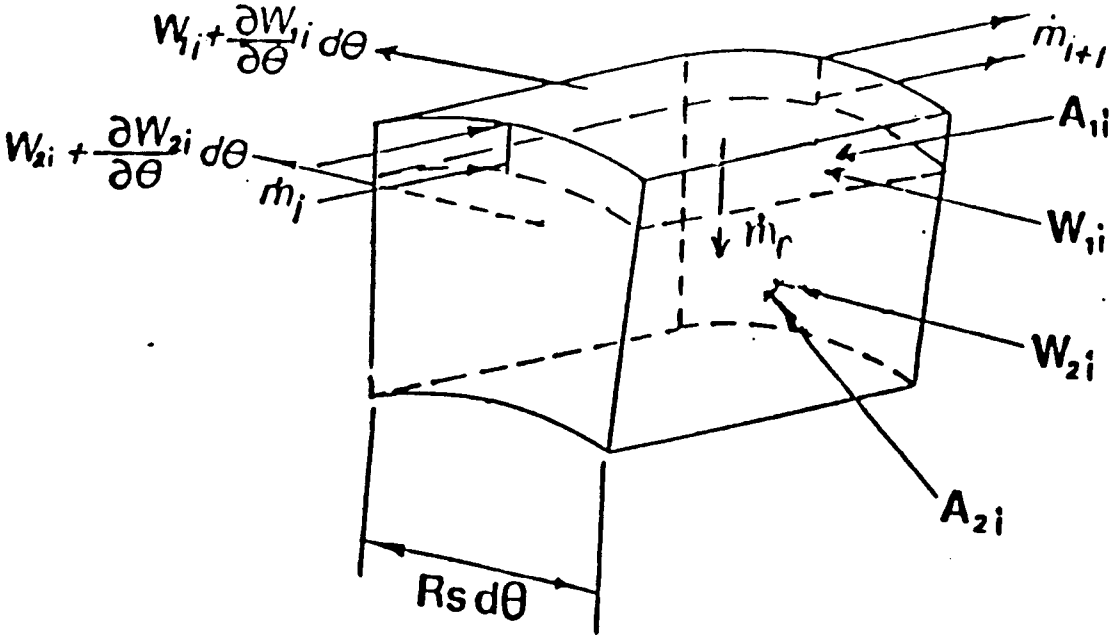

Figure 5. Isometric view of control volumes.

6) The cavity flow is turbulent and isoenergetic.

7) The recirculation velocity, U_2, is unchanged by viscous stresses as it swirls within a cavity.

The continuity equations for control volumes I and II are derived using figures 4 and 5; they are:

$$\frac{\partial \rho A_1}{\partial t} + \frac{\partial \rho W_1 A_1}{Rs_1 \partial \theta} + \dot{m}_{i+1} - \dot{m}_i + \dot{m}_r = 0$$

$$\frac{\partial \rho A_2}{\partial t} + \frac{\partial \rho W_2 A_2}{Rs_2 \partial \theta} - \dot{m}_r = 0.$$

The quantity $\dot{m}_r$ is the mass flow rate from control volume I to control volume II. The momentum equations for control volumes I and II are derived using figures 6 and 7; they are :

$$\frac{\partial \rho W_1 A_1}{\partial t} + \frac{2\rho W_1 A_1}{Rs_1}\frac{\partial W_1}{\partial \theta} + \frac{\rho W_1}{Rs_1}\frac{\partial A_1}{\partial \theta} + \frac{W_1 A_1}{Rs_1}\frac{\partial \rho}{\partial \theta} + \dot{m}_r W_{oi}$$
$$+ \dot{m}_{i+1} W_{1i} - \dot{m}_i W_{i-1} = -\frac{A_1}{Rs_1}\frac{\partial P_i}{\partial \theta} + \tau_{ji} L_i - \tau_{si} as_i L_i$$

$$\frac{\partial \rho W_2 A_2}{\partial t} + \frac{2\rho W_2 A_2}{Rs_2}\frac{\partial W_2}{\partial \theta} + \frac{\rho W_2}{Rs_2}\frac{\partial A_2}{\partial \theta} + \frac{W_2 A_2}{Rs_2}\frac{\partial \rho}{\partial \theta}$$
$$+ \dot{m}_r W_{oi} = -\frac{A_2}{Rs_2}\frac{\partial P_i}{\partial \theta} - \tau_{ji} L_i + \tau_{ri} ar_i L_i$$

where as and ar are the dimensionless length upon which the shear stresses act and are defined by

$$as_i = 1 \qquad ar_i = (2B_i + L_i)/L_i.$$

W_{oi} is the circumferential velocity between the control volumes, and τ_{ji} is the free shear stress at the interface of the two control volumes.

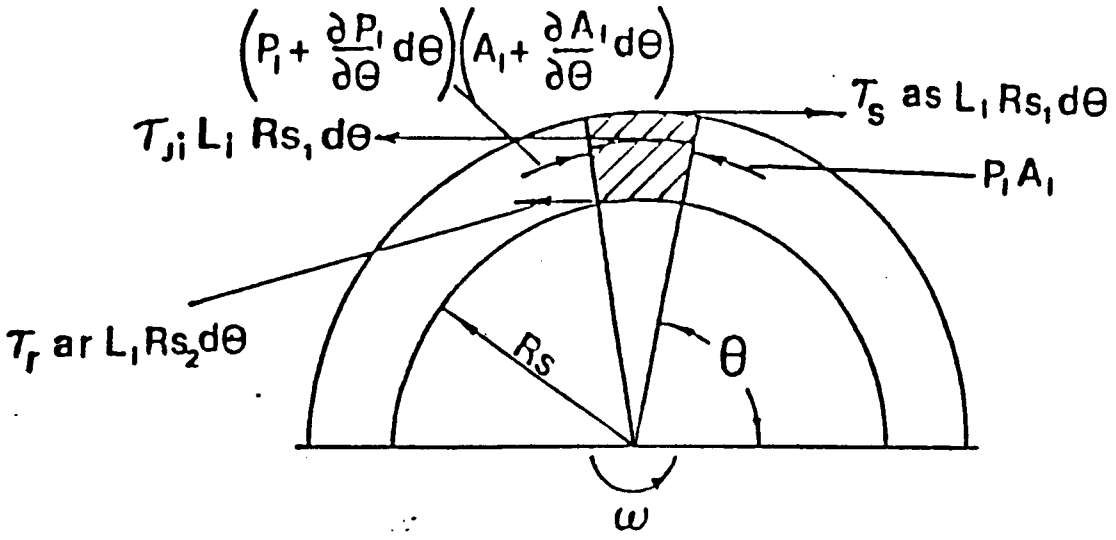

Figure 6. Forces on control volumes.

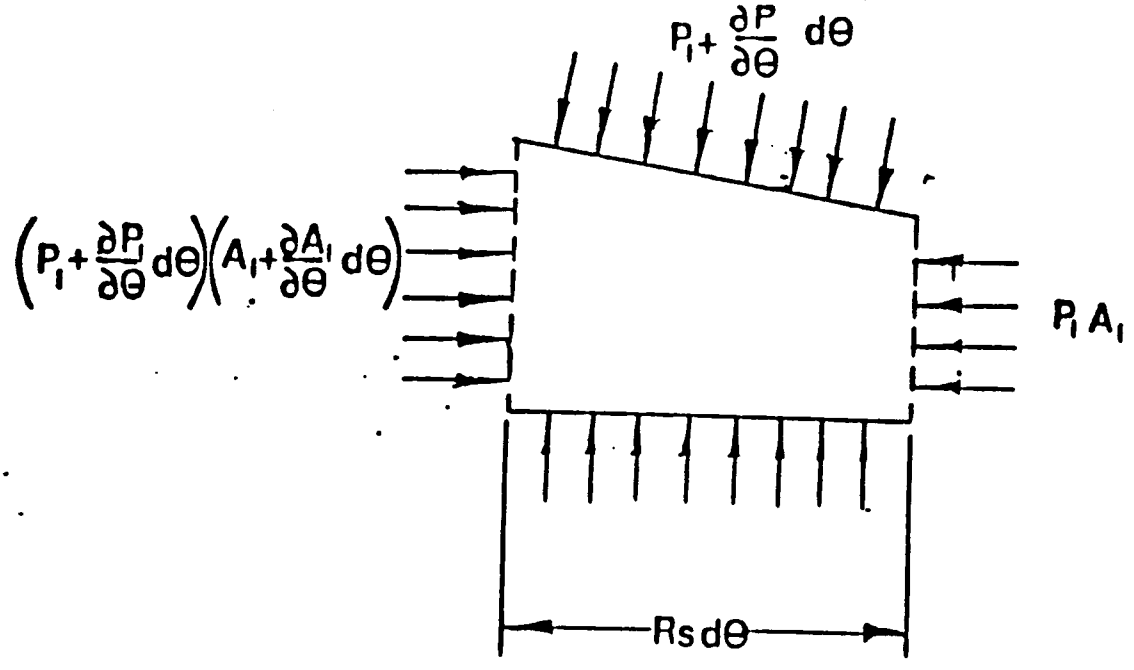

Figure 7. Pressure forces on control volume I.

The shear stresses at the rotor and stator surfaces (τ_s and τ_r) are modeled using the Blasius formula for turbulent pipe flow

$$\tau = \frac{1}{2}\rho U_m^2 no \left(\frac{U_m D_h}{\nu}\right)^{mo}$$

where U_m is the mean flow velocity relative to the surface upon which the shear stress is acting, and D_h is the hydraulic diameter of the particular control volume. For the constants mo and no, Scharrer used the values given by Yamada [16] for turbulent flow between smooth, annular surfaces:

$$mo = -0.25 \qquad no = 0.079.$$

Since no published data are available for the honeycomb stator surface used in the tests reported here, the values were determined empirically from pressure drop versus flow tests [17]. For the honeycomb surface, the values obtained were:

$$mo = -0.1083 \qquad no = 0.2820.$$

Smooth surface coefficients were obtained by the same procedure and they are:

$$mo = -0.2417 \qquad no = 0.0942.$$

These smooth surface coefficients are similar to those of Yamada. Using either Yamada's values or the empirical values produces essentially the same results in Scharrer's model. The empirical values for the smooth and honeycomb surfaces are used to obtain the respective values of the rotor and stator shear stresses for the theoretical results presented later in this report.

Scharrer uses a perturbation analysis to linearize the governing equations. This approach is only valid for small motion about a centered position. Expanding the governing equations in the perturbation variables yields a system of

twelve linear algebraic equations per cavity. Solution of these equations yields the pressure distribution along and around the seal. Integration of the pressure distribution leads to the solutions for the rotordynamic coefficients.

Required input for Scharrer's analysis is as follows:

1) reservoir pressure, temperature, and kinematic viscosity,

2) sump pressure,

3) gas constant and ratio of specific heats,

4) inlet circumferential velocity and rotor speed,

5) seal radius, radial clearance, tooth pitch, height and tip width,

6) rotor and stator friction coefficients (mr,nr,ms,ns), and

7) number of teeth.

CHAPTER III

TEST APPARATUS AND PROCEDURE

TEST APPROACH

The test method employed at the TAMU facility is the same as that used by Iino and Kaneko [18]. An external hydraulic shaker is used to impart translatory motion to the rotating seal, while rotor motion relative to the stator and reaction force components acting on the stator are measured.

Figure 8 shows the manner in which the rotor is positioned and oscillated in order to identify the dynamic coefficients of the seal for small motion about a centered position. Equation (1), rewritten here,

$$-\begin{Bmatrix} F_X \\ F_Y \end{Bmatrix} = \begin{bmatrix} K & k \\ -k & K \end{bmatrix} \begin{Bmatrix} X \\ Y \end{Bmatrix} + \begin{bmatrix} C & c \\ -c & C \end{bmatrix} \begin{Bmatrix} \dot{X} \\ \dot{Y} \end{Bmatrix} \tag{2}$$

defines the force-motion relationship. Small harmonic motion of the rotor in the X direction about a centered position is described by

$$\begin{aligned} X &= A \sin \Omega t + B \cos \Omega t \\ \dot{X} &= A\Omega \cos \Omega t - B\Omega \sin \Omega t \\ Y &= \dot{Y} = 0 \end{aligned} \tag{3}$$

where Ω is the shake frequency. Similarly, the X and Y direction force components of equation (2) can by expressed

$$\begin{aligned} F_X &= -F_{XS} \sin \Omega t - F_{XC} \cos \Omega t \\ F_Y &= -F_{YS} \sin \Omega t - F_{YC} \cos \Omega t \end{aligned} \tag{4}$$

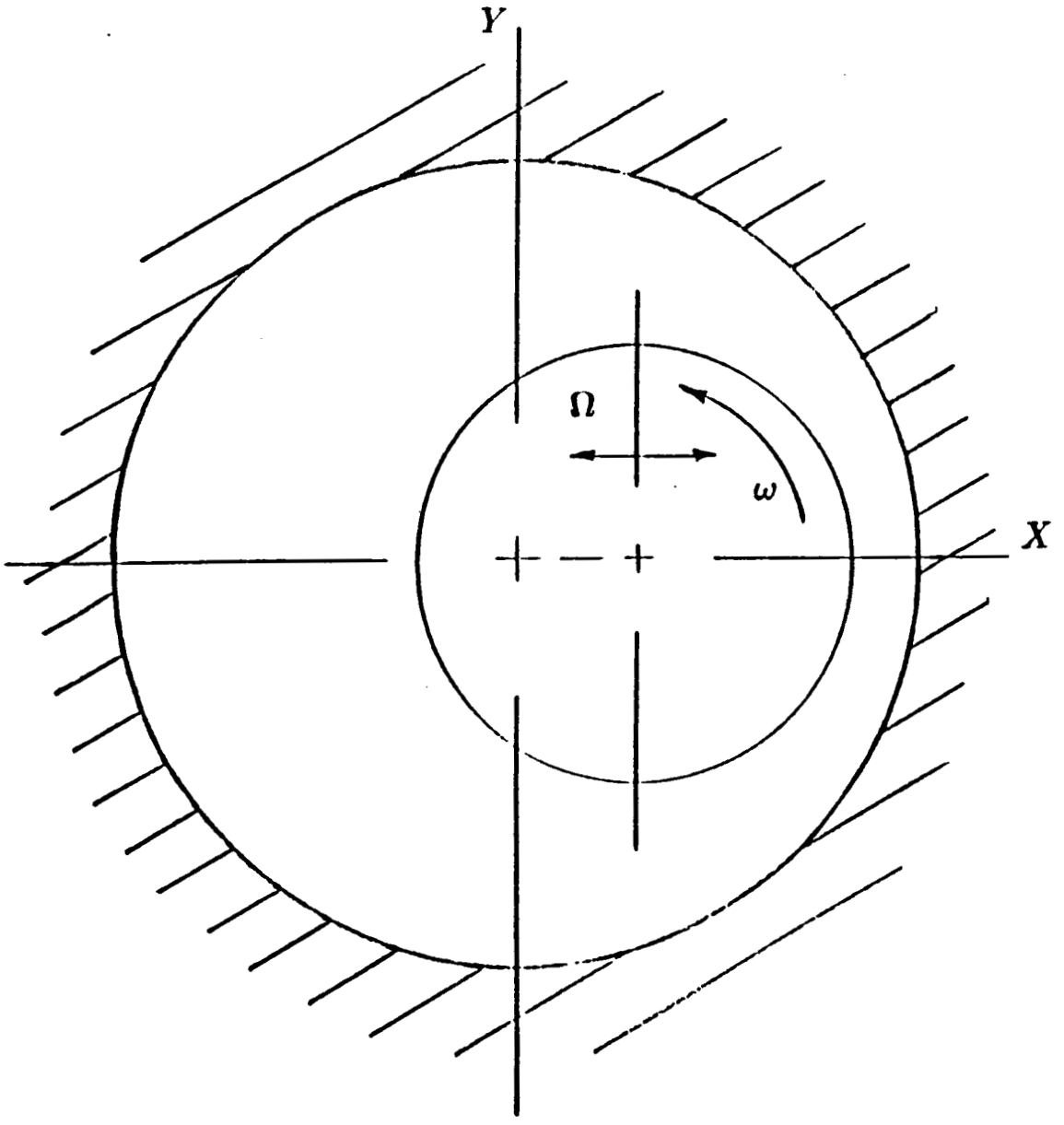

Figure 8. External shaker method used for coefficient identification.

where F_{XS}, F_{XC}, F_{YS}, and F_{YC} are Fourier coefficients of the reaction force components on the stator. Substituting equations (3) and (4) into equation (2) and equating coefficients of sine and cosine terms yields the following four equations for the dynamic coefficients

$$\begin{aligned} F_{XS} &= KA - CB\Omega \\ F_{XC} &= KB + CA\Omega \\ F_{YS} &= -kA + cB\Omega \\ F_{YC} &= -kB - cA\Omega \end{aligned} \tag{5}$$

Solving this system of four equations in four unknowns defines the dynamic coefficients as

$$\begin{aligned} K &= (F_{XS}A + F_{XC}B)/(A^2 + B^2) \\ k &= (-F_{YS}A - F_{YC}B)/(A^2 + B^2) \\ C &= (F_{XC}A - F_{XS}B)/(A^2 + B^2)\Omega \\ c &= (F_{YS}B + F_{YC}A)/(A^2 + B^2)\Omega \end{aligned} \tag{6}$$

Therefore, by measuring the reaction forces due to known rotor motion, determining the Fourier coefficients, and substituting into the above definitions, the rotordynamic coefficients can be identified independently.

APPARATUS OVERVIEW

Detailed design of the TAMU gas seal apparatus was carried out by J.B. Dressman of the University of Louisville. The test apparatus, shown in figure 9, was designed to identify the rotordynamic coefficients for various inlet pressures, inlet swirl velocities, rotor speeds, and seal configurations. Each of these parameters can be varied in the theoretical analysis as well. Thus, the influence of each independent parameter can be measured and compared to theoretical predictions.

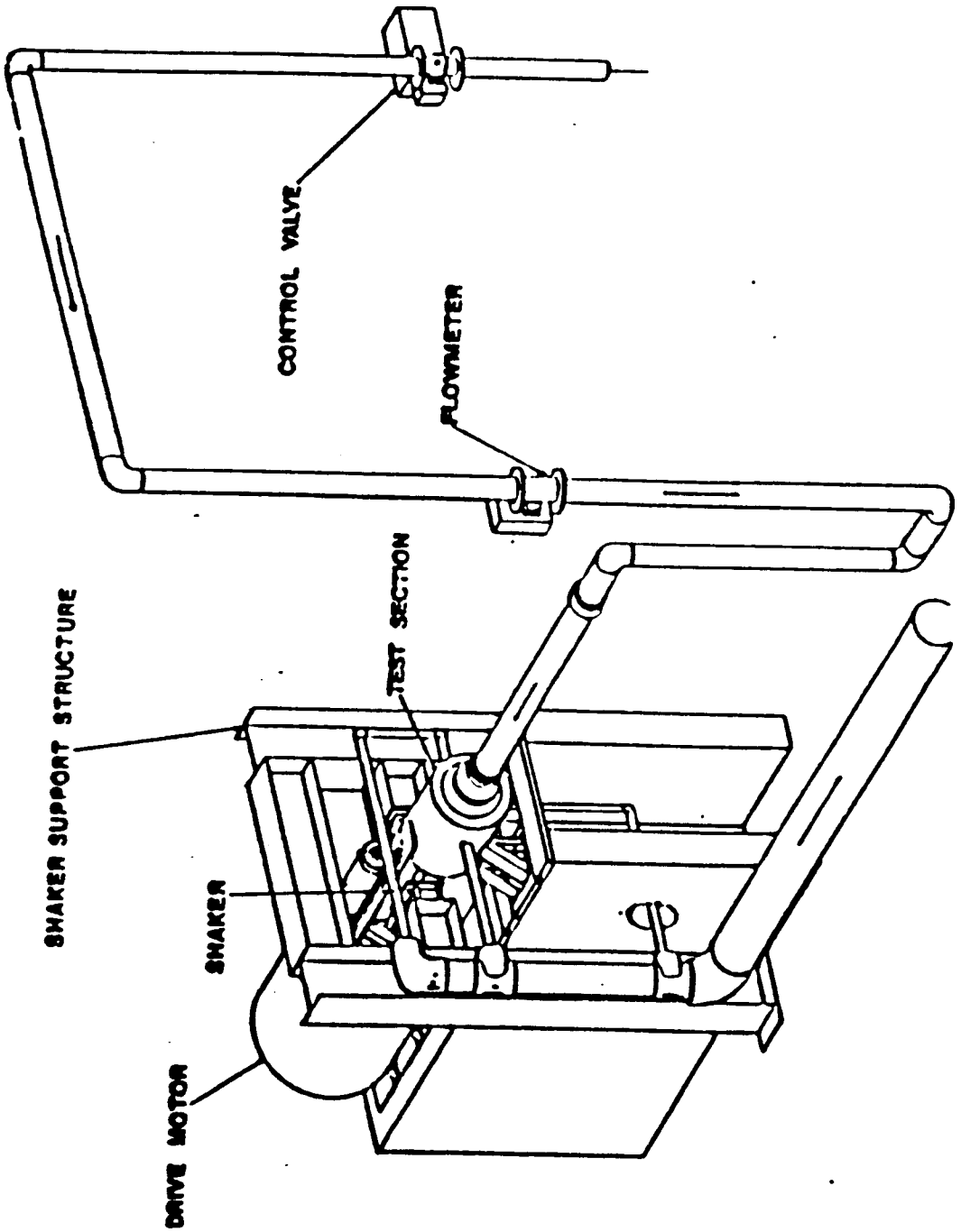

Figure 9. Test apparatus assembly.

A discussion of the apparatus is presented in three sections. The first section, Test Hardware, describes how the various seal parameters are physically executed and controlled. The second section, Instrumentation, describes how these controlled parameters are measured. Finally, the Data Acquisition and Reduction section explains how these measurements are used to provide the desired information.

TEST HARDWARE

Static Displacement Control

The test apparatus is designed to provide control over the static eccentricity position both horizontally and vertically within the seal. The rotor shaft is suspended pendulum-fashion from an upper, rigidly mounted pivot shaft, as shown in figures 10 and 11. This arrangement controls the side-to-side motion of the rotor, and a cam within the pivot shaft controls the vertical position of the rotor.

The cam which controls the vertical position of the rotor is driven by a remotely-operated DC gearhead motor, allowing accurate positioning of the rotor during testing. Horizontal positioning of the rotor is accomplished by a Zonic hydraulic shaker head and master controller, which provide independent static and dynamic displacement or force control. The shaker head is mounted on an I-beam support structure, and can supply up to 4450 N (1000 lbf) static and 4450 N dynamic force at low frequencies. The dynamic force decreases as frequency is increased. As illustrated in figure 10, the shaker head output shaft acts on the rotor shaft bearing housing, and works against a return spring mounted on the opposite side of the bearing housing. The return spring maintains contact

ORIGINAL PAGE IS
OF POOR QUALITY

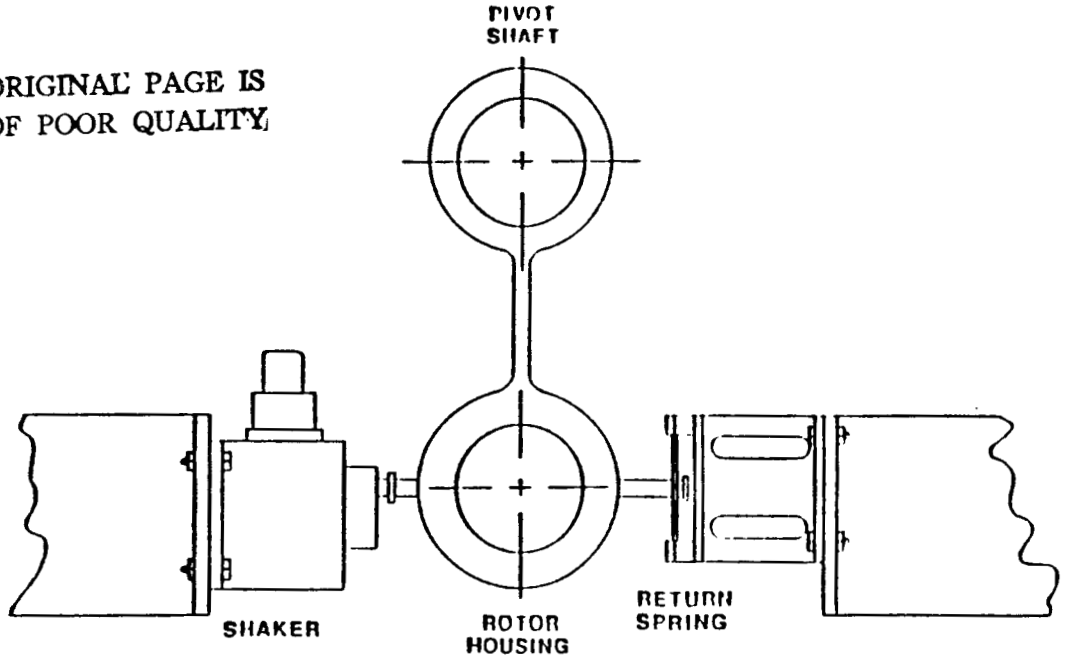

Figure 10. Components used for static and dynamic displacement of seal rotor.

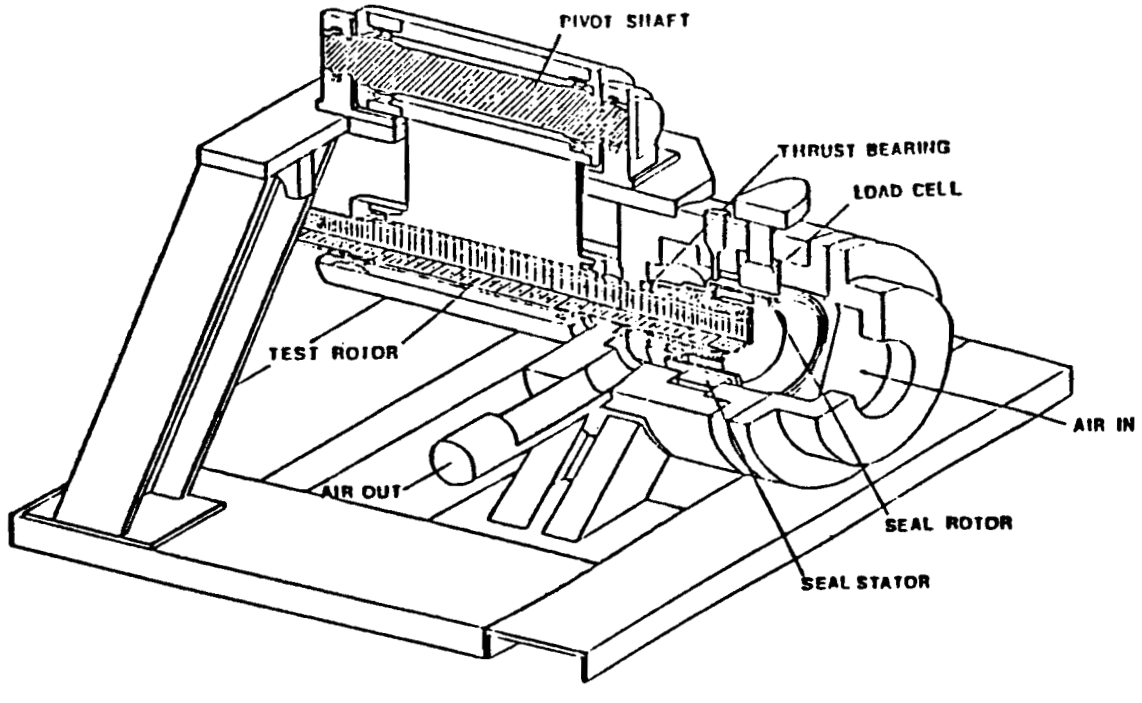

Figure 11. Test apparatus.

between the shaker head shaft and the bearing housing, thereby preventing hammering of the shaker shaft and the resulting loss of control over the horizontal motion of the rotor.

Dynamic Displacement Control

The dynamic motion of the seal rotor within the stator is horizontal. In addition to controlling the static horizontal position of the rotor, the Zonic shaker head moves the rotor through horizontal harmonic oscillations as the test is run. A Wavetek function generator provides the sinusoidal input signal to the Zonic controller, and both the amplitude and frequency of the rotor oscillations are controlled.

In addition to providing control over the rotor's static position and dynamic motion, the test apparatus allows other seal parameters to be controlled independently, providing insight into the influence these parameters have on seal behavior. These parameters coincide with the variable input parameters for the analysis, and they include:

1) pressure ratio across the seal,
2) prerotation of the incoming fluid,
3) seal configuration, and
4) rotor rotational speed.

Pressure Ratio

The inlet air pressure and attendant mass flow rate through the seal are controlled by an electric-over-pneumatically actuated Masonelian Camflex II flow control valve located upstream of the section. An Ingersoll-Rand SSR-2000 single

stage screw compressor rated at 34 m^3/min @ 929 kPa (1200 scfm @ 120 psig) provides compressed air, which is then filtered and dried before entering a surge tank. Losses through the dryers, filters, and piping result in an actual maximum inlet pressure to the test section of approximately 825 kPa (105 psig) at a flow rate of 10 m^3/min (350 scfm). A four inch inlet pipe from the surge tank supplies the test rig, and after passing through the seal, the air exhausts to atmosphere through a manifold with muffler.

Inlet Circumferential Velocity

In order to determine the effects of fluid rotation on the rotordynamic coefficients, the test rig design also allows for prerotation of the incoming air as it enters the seal. This prerotation introduces a circumferential component to the air flow direction, and is accomplished by guide vanes which direct and accelerate the flow towards the annulus of the seal. Figure 12 illustrates the vane configuration. Three sets of guide vanes were used; two rotate the flow in the direction of rotor rotation at different speeds, and a third introduces no fluid rotation. The important difference between the first two vanes is the gap height, A. The vanes with a smallest gap height produce the highest inlet tangential velocity.

Seal Configuration

The design of the test section, figure 13, permits the installation of various rotor/stator combinations. The stator is supported in the test section housing by three Kistler quartz load cells in a trihedral configuration, as shown in figure 14. Different seal stator designs are obtained by the use of inserts. The smooth and honeycomb inserts used for the 0.4 mm (0.016 in) radial clearance seal tests are shown in figure 15. The labyrinth rotor and the tooth detail are shown in figures

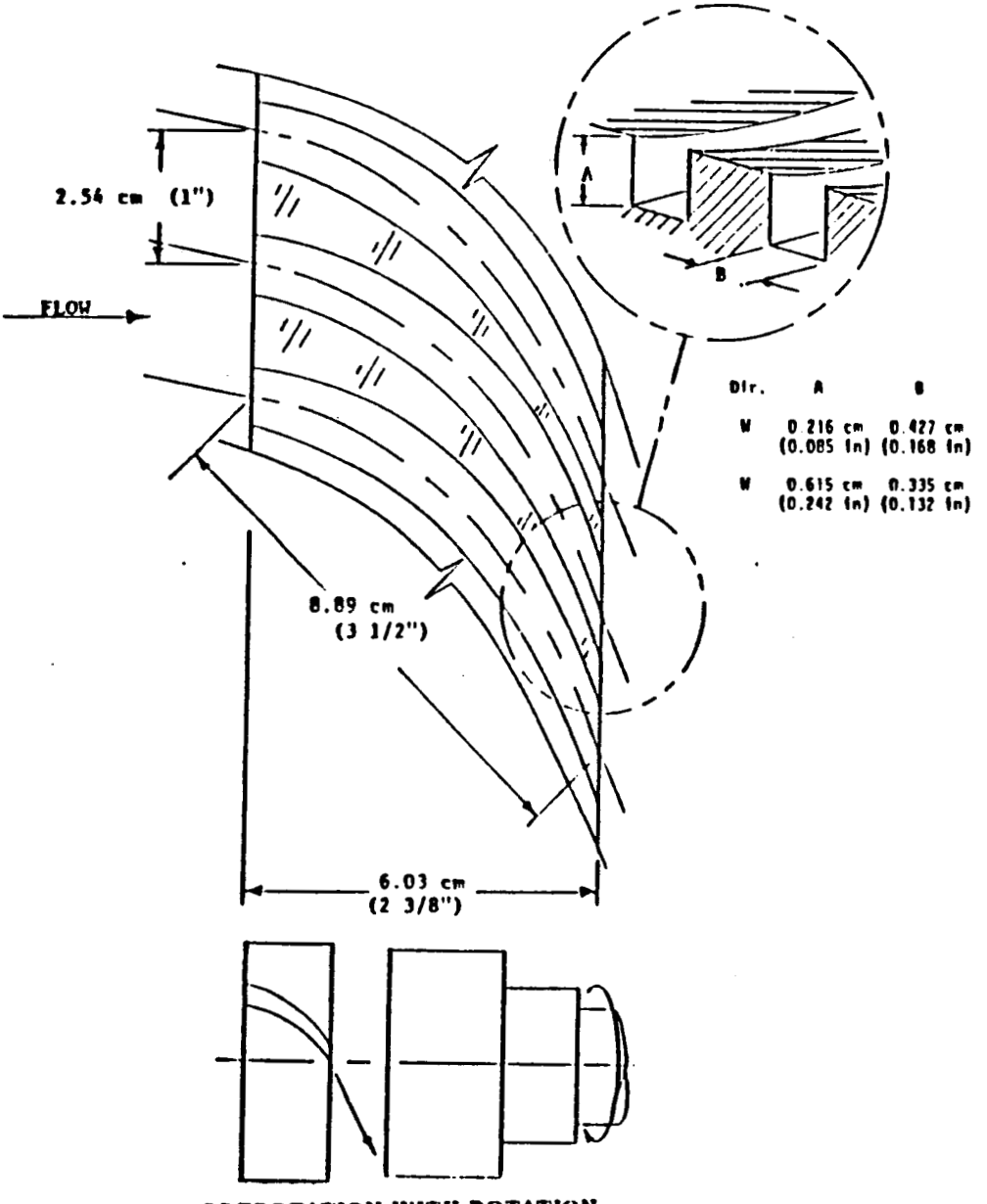

Figure 12. Inlet-guide-vane detail.

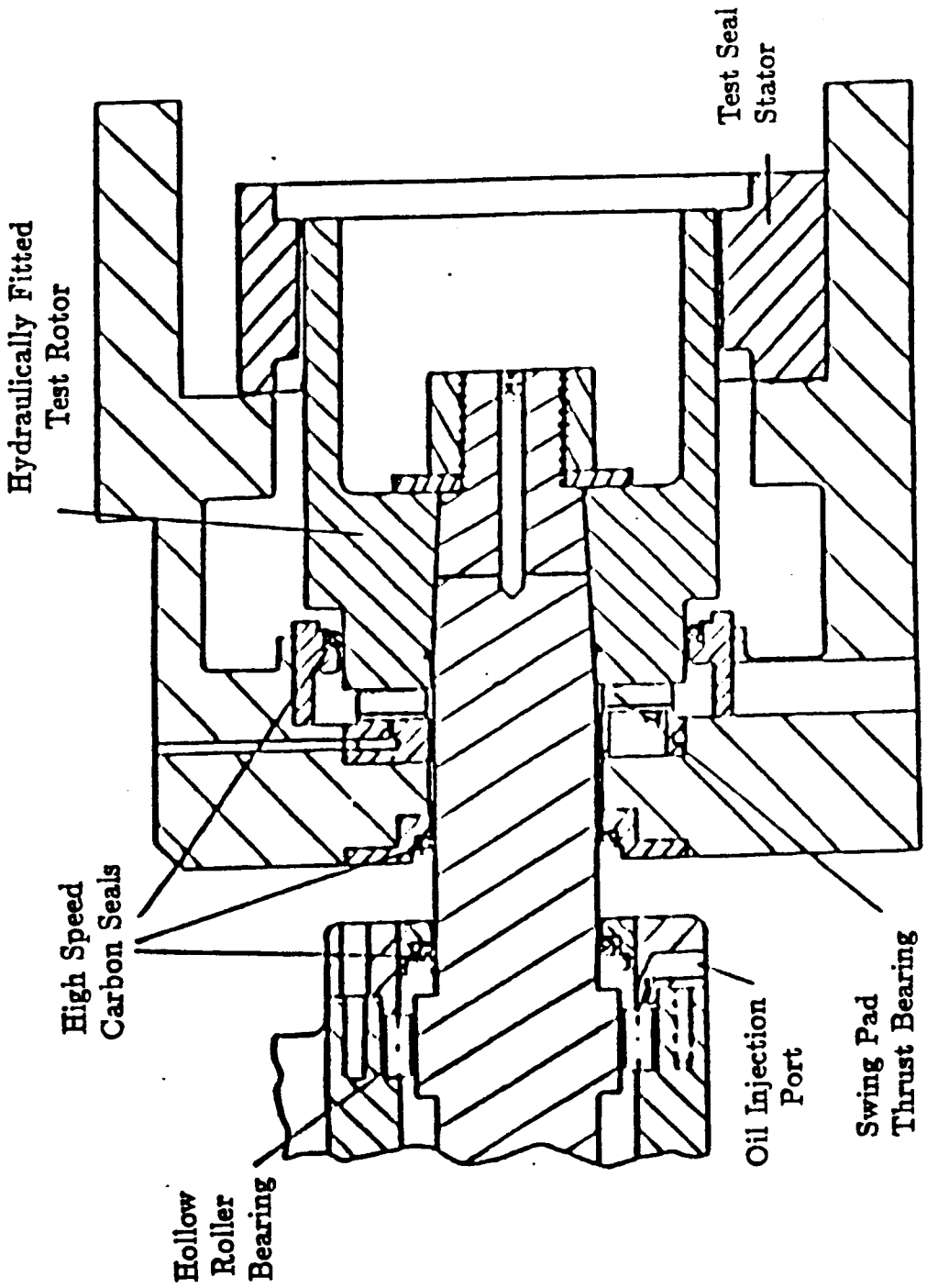

Figure 13. Cross-sectional view of test section showing rotor-shaft assembly.

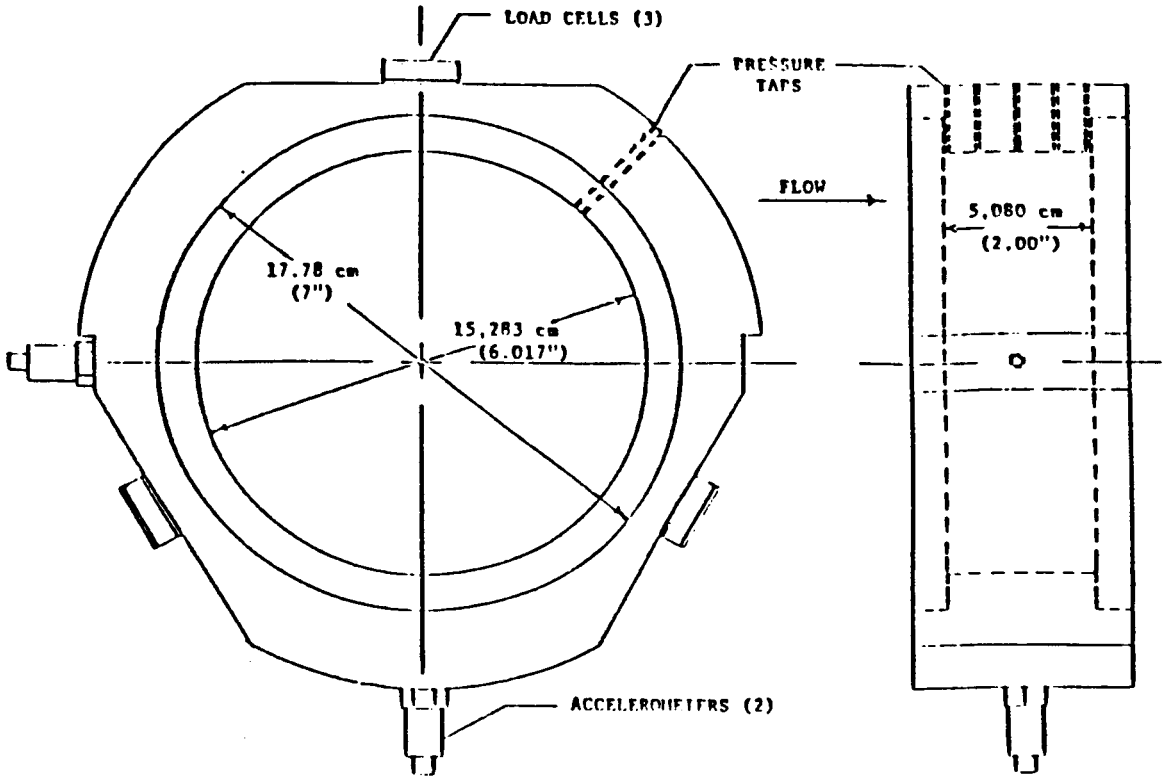

Figure 14. Detail of smooth stator.

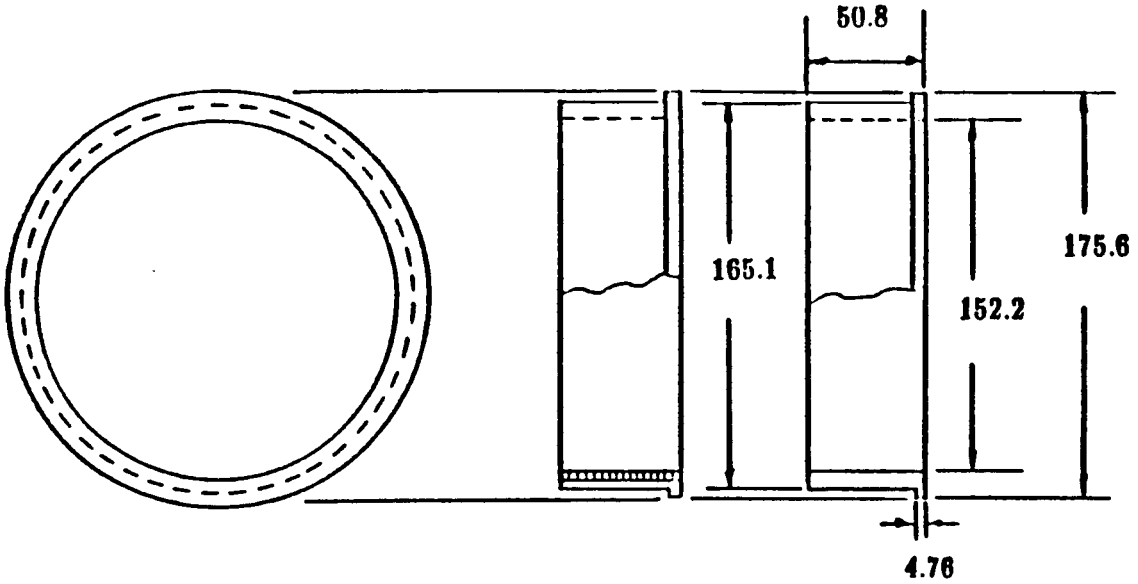

Figure 15. Honeycomb and smooth inserts for 0.4 mm (0.016 in) radial seal clearance. Drawing dimensions are millimeters.

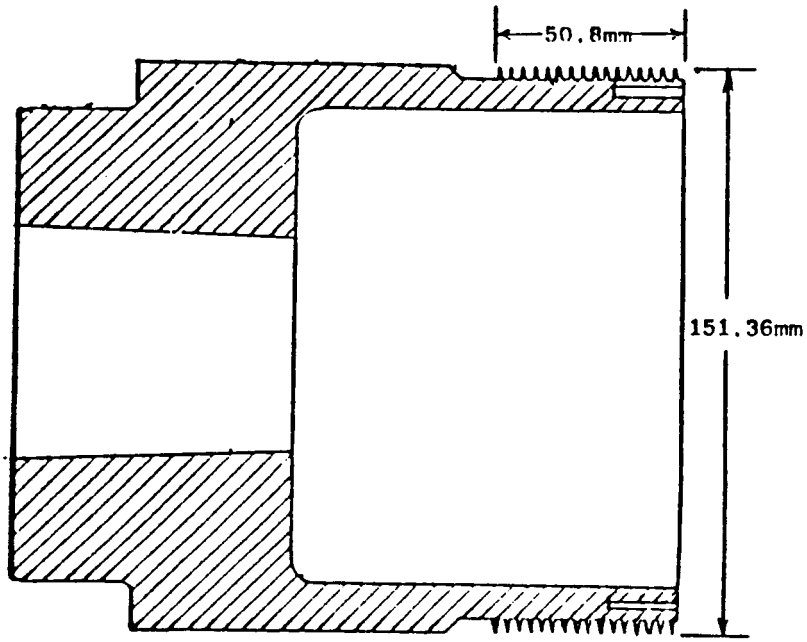

Figure 16. Detail of labyrinth rotor.

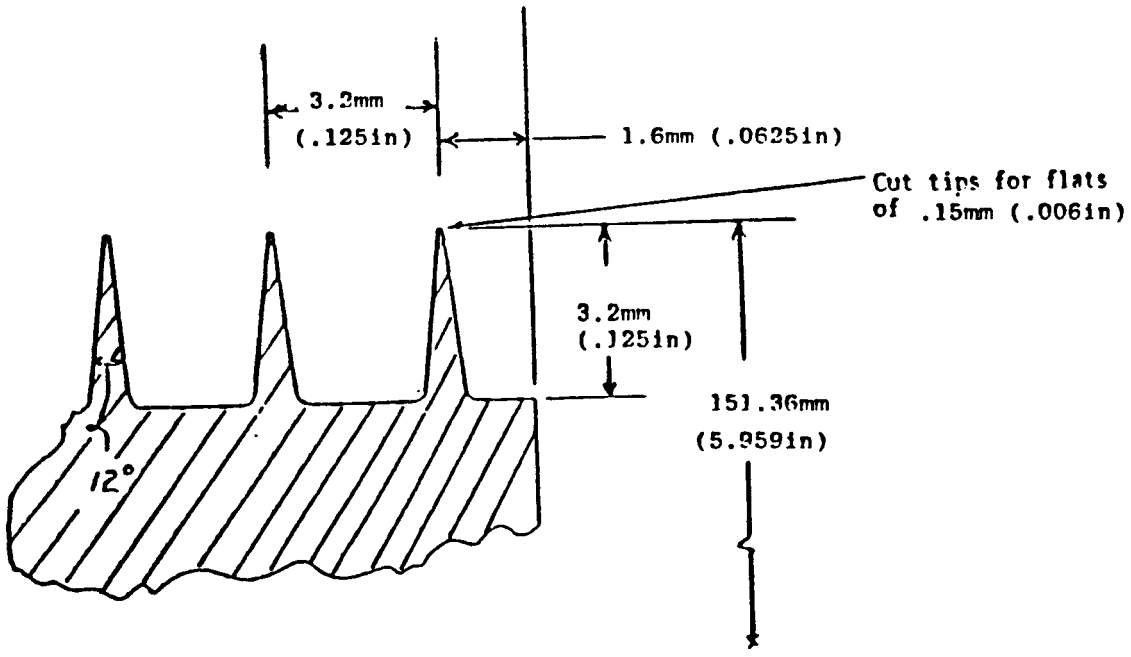

Figure 17. Detail of labyrinth tooth.

16 and 17. Seals with different geometries (i.e., clearances, tapers, lengths) can be tested, as well as seals with different surface roughnesses.

Rotor Speed

A Westinghouse 50-hp variable-speed electric motor drives the rotor shaft through a belt-driven jackshaft arrangement. A Square D Omegapak 1500 frequency controller provides speed control from 0 - 16,000 cpm. The shaft is supported by two sets of Torrington hollow- roller bearings. These bearings, described by Bowen and Bhateje [19], are extremely precise, radially preloaded, and have a predictable and repeatable radial stiffness. The shaft bearings are lubricated by positive-displacement gear-type oil pump.

INSTRUMENTATION

Three types of measurements are necessary to obtain the desired data:

1) rotor motion
2) reaction-force measurements, and
3) fluid flow measurements.

Each of these categories is described below.

Rotor Motion Measurements

The position of the seal rotor within the stator is monitored by four Bently-Nevada eddy-current proximity probes mounted in the test section housing. These probes are located 90 degrees apart, and correspond to the X and Y directions. The proximity probes are used to determine the static position and dynamic motion of the rotor, and their resolution is 0.0025 mm (0.1 mil).

Reaction-Force Measurements

Reaction forces arise due to the motion of the seal rotor within the stator. The reaction forces (F_X, F_Y) exerted on the stator are measured by the three Kistler quartz load cells which support the stator in the test section housing. When the rotor is shaken, vibration is transmitted to the test section housing, both through the thrust bearing and through the housing mounts. The acceleration of the housing and stator generates unwanted inertial *ma* forces which are sensed by the load cells, in addition to those pressure forces developed by the relative motion of the seal rotor and stator. For this reason, PCB piezoelectric accelerometers with integral amplifiers are mounted in the X and Y directions on the stator, as shown in figure 14. These accelerometers allow a (*stator mass*) $\times$ (*stator acceleration*) subtraction to the forces (F_X, F_Y) indicated by the load cells. With this correction, which is described more fully in the next section, only the pressure forces due to relative seal motion are measured.

Force measurement resolution is a function of the stator mass and the resolution of the load cells and accelerometers. Accelerometer resolution is 0.005 g, which must be multiplied by the stator mass in order to obtain an equivalent force resolution. The mass of the stator used in the test program reported here is 11.5 kg (25.3 lb). Hence, the force resolution for the accelerometers is 0.560 N (0.126 lb). Resolution of the load cells is 0.089 N (0.02 lb). Therefore, the resolution of the force measurement is limited by the accelerometers.

Fluid Flow Measurements

Fluid flow measurements include the leakage (mass flow rate) of air through

the seal, the pressure gradient along the seal axis, and the inlet fluid circumferential velocity.

Leakage is measured with a Flow Measurement Systems Inc. turbine flowmeter located in the piping upstream of the test section. Resolution of the flowmeter is 0.0005 acf, and pressures and temperatures up and downstream of the meter are measured for mass flow rate determination.

For measurement of the axial pressure gradient, the stator has pressure taps drilled along the length of the seal in the axial direction. These pressures, as well as all others, are measured with a 0-1.034 MPa (0-150 psig) Scanivalve differential-type pressure transducer through a 48 port, remotely-controlled Scanivalve model J scanner. Transducer resolution is 0.552 kPa (0.08 psi). Overall accuracy of the pressure measurements is limited by the resolution of the 12 bit A/D converter which can only resolve the pressure signal to ±0.62 kPa (0.09 psi). Combined linearity and hysteresis error for the pressure transducer is 0.06%.

In order to determine the circumferential velocity of the air as it enters the seal, the static pressure at the guide vane exit is measured. This pressure, in conjunction with the measured flow rate and inlet air temperature, is used to calculate a guide vane exit Mach number. The compressible flow continuity equation

$$\dot{m} = P_{ex} A_{ex} M_{ex} \left[\frac{\gamma}{RT_t} \left(1 + \frac{(\gamma - 1) M_{ex}^2}{2} \right) \right]^{1/2}$$

is rearranged to provide a quadratic equation for M_{ex}

$$M_{ex}^2 = \frac{-1 + \sqrt{1 + \frac{4(\gamma - 1)}{2} \frac{RT_t}{\gamma} \left(\frac{\dot{m}}{P_{ex} A_{ex}} \right)^2}}{\gamma - 1}$$

where γ is the ratio of specific heats and R is the gas constant for air, T_t is the stagnation temperature of the air, P_{ex} is the static pressure at the vane exit, and A_{ex} is the total exit area of the guide vanes. Since all of the variables in the equation are either known or measured, the vane exit Mach number, and therefore the velocity, can be found.

In order to determine the circumferential component of this inlet velocity, a flow turning angle correction, in accordance with Cohen [20] is employed. The correction has been developed from guide vane cascade tests, and accounts for the fact that the fluid generally is not turned through the full angle provided by the shape of the guide vanes. With this flow deviation angle calculation, the actual flow direction of the air leaving the vanes (and entering the seal) can be calculated. Hence, the magnitude and direction of the inlet velocity is known, and the appropriate component is the measured inlet circumferential velocity.

DATA ACQUISITION AND REDUCTION

Data acquisition is directed from a Hewlett-Packard 9816 (16-bit) computer. The computer controls an H-P 6940B multiprogrammer which has 12-bit A/D and D/A converter boards. The multiprogrammer transfers control commands to and test data from the instrumentation.

As previously stated, the major data groups are seal motion/reaction force data and fluid flow data. The motion/reaction force data are used for dynamic coefficient identification. The fluid flow data are used as input parameters for the theoretical analysis.

The hardware involved in obtaining the force/motion data includes the load cells, accelerometers, X direction motion probe, a Sensotec analog filter unit, a tuneable bandpass filter, and the A/D converter. The operation of these components is illustrated in figure 18, and their outputs are used in a serial sampling scheme which provides the computer with the desired data for reduction. Recalling the discussion of the reaction force measurements in the preceding section, a (*stator mass*) $\times$ (*stator acceleration*) subtraction from the indicated loadcell forces is necessitated due to vibration of the stator and test section housing. This subtraction is performed with an analog circuit, and results in corrected F_X and F_Y force components due to relative seal motion. The forced oscillatory shaking motion of the seal rotor is the key to the operation of the serial synchronous sampling (SSS) routine which is employed. The frequency of the rotor oscillations is set by a function generator, and rotor motion is sensed by the X direction motion probe. The motion signal is filtered by the narrow bandpass filter, and is used as a trigger signal for the SSS routine. Upon the operator's command, the SSS routine is enabled, and the next positive- to-negative crossing of the filtered motion signal triggers a quartz crystal clock/timer. Ten cycles of the corrected $F_X(t)$ signal are sampled, at a rate of 100 samples/cycle. The second positive-to-negative crossing of the filtered motion signal triggers the timer and initiates the sampling of ten cycles of the $F_Y(t)$ signal. Finally, the third positive-to-negative crossing triggers the timer again, and ten cycles of the corrected $X(t)$ signal are sampled. Thus, at every test condition, 1000 data points are obtained for $F_X(t_i)$, $F_Y(t_i)$, and $X(t_i)$, and the data arrays are stored in computer memory.

Note that the bandpass filter is used only to provide a steady signal to trigger the timer/clock. Any modulation of the motion signal due to rotor runout is eliminated by this filter, provided the rotational frequency and shake frequency

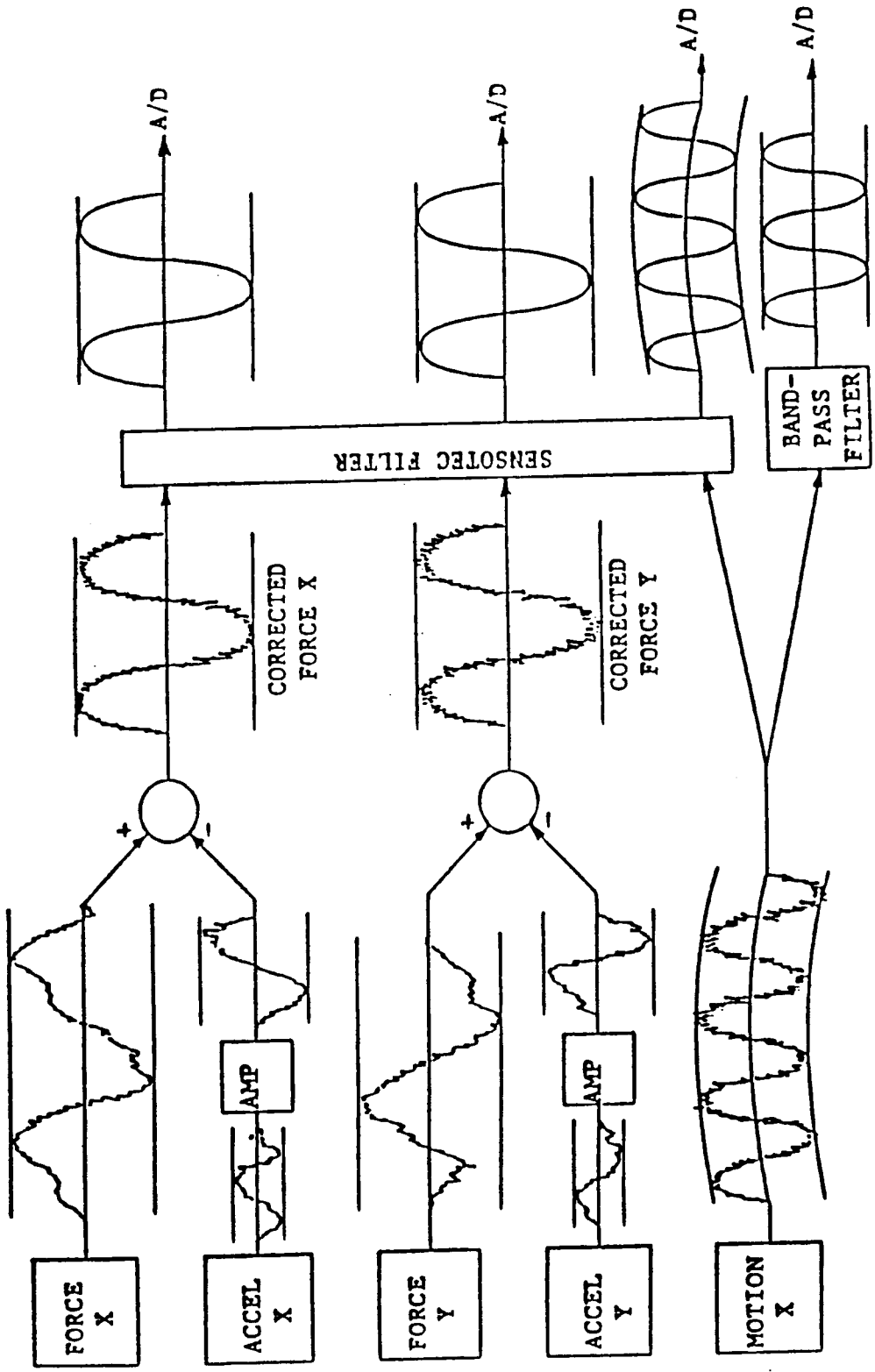

Figure 18. Signal conditioning schematic for data acquisition.

are adequately separated, and the shake frequencies are selected to provide adequate separation with running speeds. However, the rotor motion and corrected force signals which are sampled and captured for coefficient identification are filtered only by a low-pass filter (500 Hz cutoff), and the effects of runout as well as shaking motion are present in the recorded data. A second point worth noting is that the sample rate depends directly on the shake frequency. As the shake frequency is increased, the sample rate (samples/second) also increases. In order to get the desired 100 samples/cycle, shake frequencies must be chosen to correspond to discrete sample rates which are available. Hence, the frequency at which the rotor is shaken is carefully chosen to provide the desired sampling rate and a steady trigger signal. The uncertainty in the shake frequency is 0.13 Hz for the 74.6 Hz case.

PROCEDURE

At the start of each day's testing, the force, pressure, and flowmeter systems are calibrated. The total system, from transducer to computer, is calibrated for each of these variables. The force system calibration utilizes a system of pulleys and known weights applied in the X and Y directions. An air-operated deadweight pressure tester is used for pressure system calibration, and flowmeter system calibration is achieved with an internal precision clock which simulates a known flow rate.

A typical test begins by centering the seal rotor in the stator with the static capability of the Zonic hydraulic shaker, starting the air flow through the seal, setting the rotor speed, and then beginning the shaking motion of the rotor. Data points are taken at rotor speeds of 3000, 6000, 9500, 13,000, and 16,000

cpm with a tolerance of ±10 cpm. At each rotor speed, data points are taken at pressures of 3.08 bar (30 psig), 4.46 bar (50 psig), 5.84 bar (70 psig), 7.22 bar (90 psig), and 8.25 bar (105 psig), as measured upstream of the flowmeter with a tolerance of ± 0.069 bar (1.0 psig). For each test case (i.e., one particular rotor speed, shake frequency, inlet pressure, and prerotation condition), the measured leakage, rotordynamic coefficients, and axial pressure distribution are determined and recorded.

This test sequence is followed for each of two different shake frequencies, and for three inlet swirl directions. Therefore, twenty-five data points are taken per test with a total of six tests per seal.

CHAPTER IV

INTRODUCTION TO TEST RESULTS

Test results for six teeth-on-rotor labyrinth gas seal configurations are presented. Three of the seals have honeycomb stators, each with a different rotor-to-stator clearance. The other three seals have smooth stators, each with a different clearance, corresponding to one of the honeycomb-stator seals. The seals are described in figure 19 and table 1. As noted in table 1, seals 1, 2 and 3 have honeycomb stators with nominal radial clearances of .008, .012 and .016 inch respectively. Seals 4, 5 and 6 have smooth stators and nominal radial clearances of .008, .012 and .016 inch respectively. Throughout this report, the seals will be referred to by their number designations. Seals 1, 2, 3 and 4 were tested for this study, and the data for these seals is reported here for the first time. Seals 5 and 6 were tested previously and documented by Scharrer [13]. The data are presented here again to provide comparison to the corresponding honeycomb stator seals (seals 2 and 3).

The objectives of this study were as follows:

1) Test three labyrinth-rotor/honeycomb-stator gas seals with different clearances for stiffness and damping rotordynamic coefficients as a function of rotor speed, pressure drop, and inlet circumferential velocity.

2) Compare the rotordynamic stability of labyrinth-rotor/honeycomb-stator gas seals to labyrinth-rotor/smooth-stator gas seals by comparing the measured rotordynamic coefficients to previously measured rotordynamic coefficients for labyrinth-rotor/smooth-stator gas seals.

Honeycomb Stator Seals

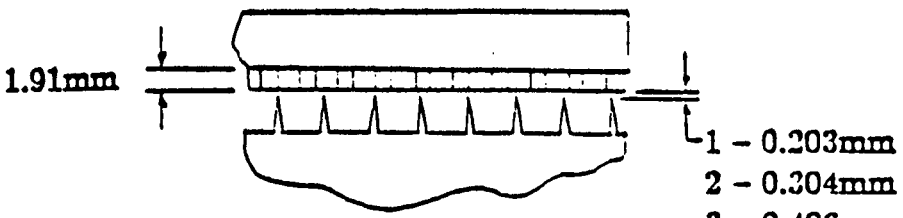

Seal 1, Seal 2, Seal 3

Smooth Stator Seals

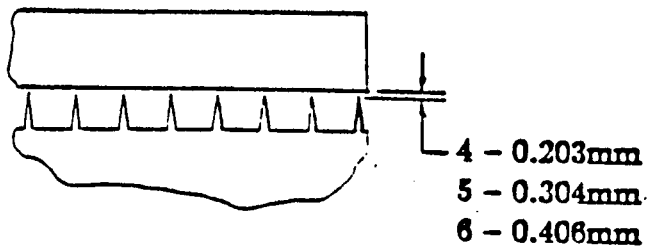

Seal 4, Seal 5, Seal 6

Honeycomb Cell Pattern

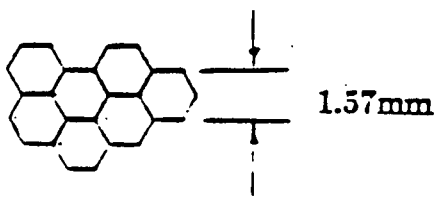

Figure 19. Seal configurations.

Table 1. Seal descriptions.

	Honeycomb Stator	Smooth Stator
Seal Designation	Seal 1	Seal 4
Number of Teeth	16	16
Nominal Radial Clearance	0.203mm (0.008in)	.203mm (0.008in)
Stator Inside Diameter	151.71mm (5.973in)	151.71mm (5.973in)
Seal Length	50.8mm (2.00in)	50.8mm (2.00in)
Seal Designation	Seal 2	Seal 5
Number of Teeth	16	16
Nominal Radial Clearance	0.304mm (0.012in)	.203mm (0.012in)
Stator Inside Diameter	151.92mm (5.981in)	151.92mm (5.981in)
Seal Length	50.8mm (2.00in)	50.8mm (2.00in)
Seal Designation	Seal 3	Seal 6
Number of Teeth	16	16
Nominal Radial Clearance	0.406mm (0.016in)	.406mm (0.016in)
Stator Inside Diameter	152.2mm (5.989in)	152.2mm (5.989in)
Seal Length	50.8mm (2.00in)	50.8mm (2.00in)

3) Use the experimental data to evaluate the validity of theoretical predictions for the rotordynamic coefficients of labyrinth-rotor/honeycomb-stator gas seals.

The parameters varied during the tests were rotor speed, reservoir pressure, circumferential velocity of the inlet air, frequency of translatory rotor motion, and seal configuration. Two shake frequencies, 56.8 and 74.6 Hz, were used during testing with essentially the same results. The results presented here were obtained using the 74.6 Hz shake frequency at an amplitude between 0.0025 and 0.0035 inches. The seal configurations are identified in table 1. The actual test points for rotor speed, supply pressure and inlet circumferential velocity are shown in table 2.

Figures 20–22 show the inlet circumferential velocity ratio for the configurations described in table 2. The inlet circumferential velocity ratio is the ratio of inlet circumferential velocity to rotor surface velocity. Calculation of circumferential velocity is described in the previous section. Note that curve 1 (representing zero inlet circumferential velocity) lies on the horizontal axis in each figure. Inlet circumferential velocity ratio ranged from 0 to about 3.5. When reviewing the following data, table 1, table 2 and figures 20–22 should be consulted for the definitions of symbols used.

One data point that appears in several figures of the following two chapters is obviously erroneous. The data point of concern is the value of direct stiffness for seal 4 at 16,000 cpm, 3.08 bar, and inlet circumferential velocity 1. Figure 23 shows the erroneous data point clearly. Both plots in figure 23 show direct stiffness versus rotor speed for seal 4. The left hand plot contains data taken at

Table 2. Definition of symbols used in figures.

Supply Pressure	Rotor Speeds	Inlet Circumferential Velocities
1 - 3.03 bar	1 - 3,000 cpm	1 - Zero tangential velocity
2 - 4.46 bar	2 - 6,000 cpm	2 - Low velocity with rotation
3 - 5.84 bar	3 - 9,500 cpm	3 - High velocity with rotation
4 - 7.22 bar	4 - 13,000 cpm	
5 - 8.25 bar	5 - 16,000 cpm	

Table 3. Growth of rotor with rotational speed.

Rotor speed (cpm)	Diametrical Growth (mm) (inches × 1000)	
3,000	0.01	0.3
6,000	0.02	0.8
9,500	0.03	1.2
13,000	0.05	1.8
16,000	0.11	4.4

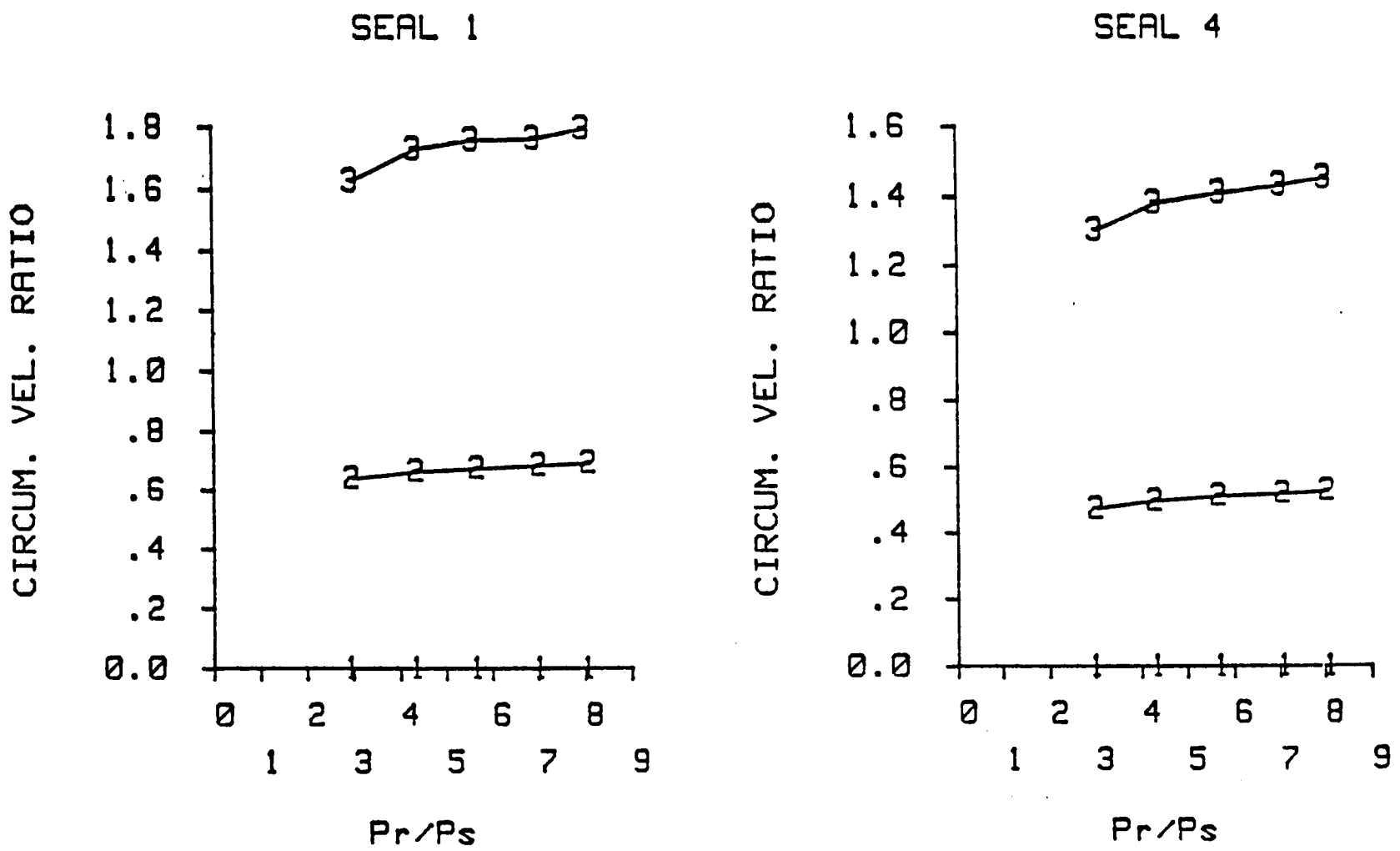

Figure 20. Inlet circumferential velocity ratios for seals 1 & 4. Inlet circumferential velocities 1–3 are plotted (see Table 2). Honeycomb stator (left), smooth stator (right).

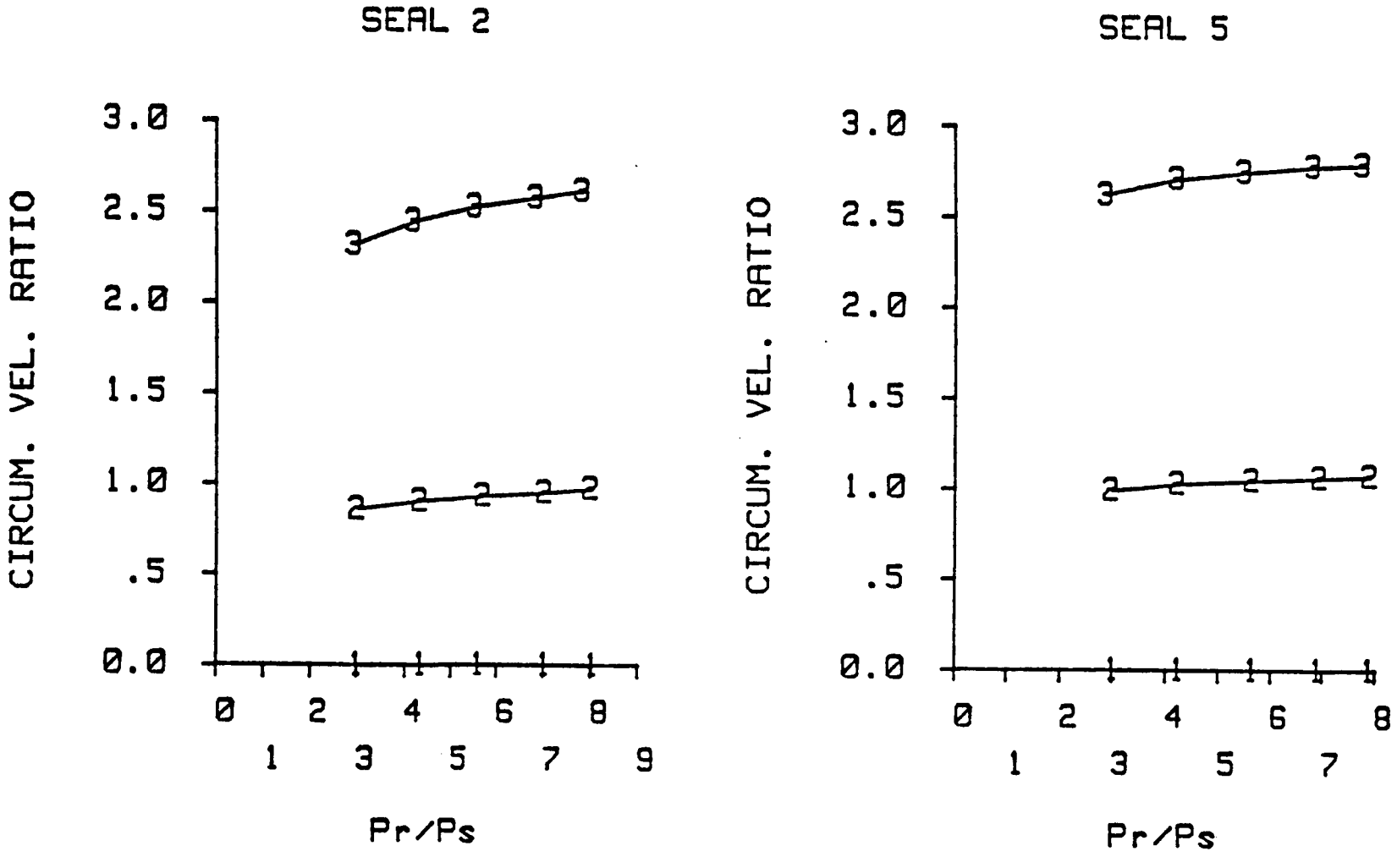

Figure 21. Inlet circumferential velocity ratios for seals 2 & 5. Inlet circumferential velocities 1–3 are plotted (see Table 2). Honeycomb stator (left), smooth stator (right).

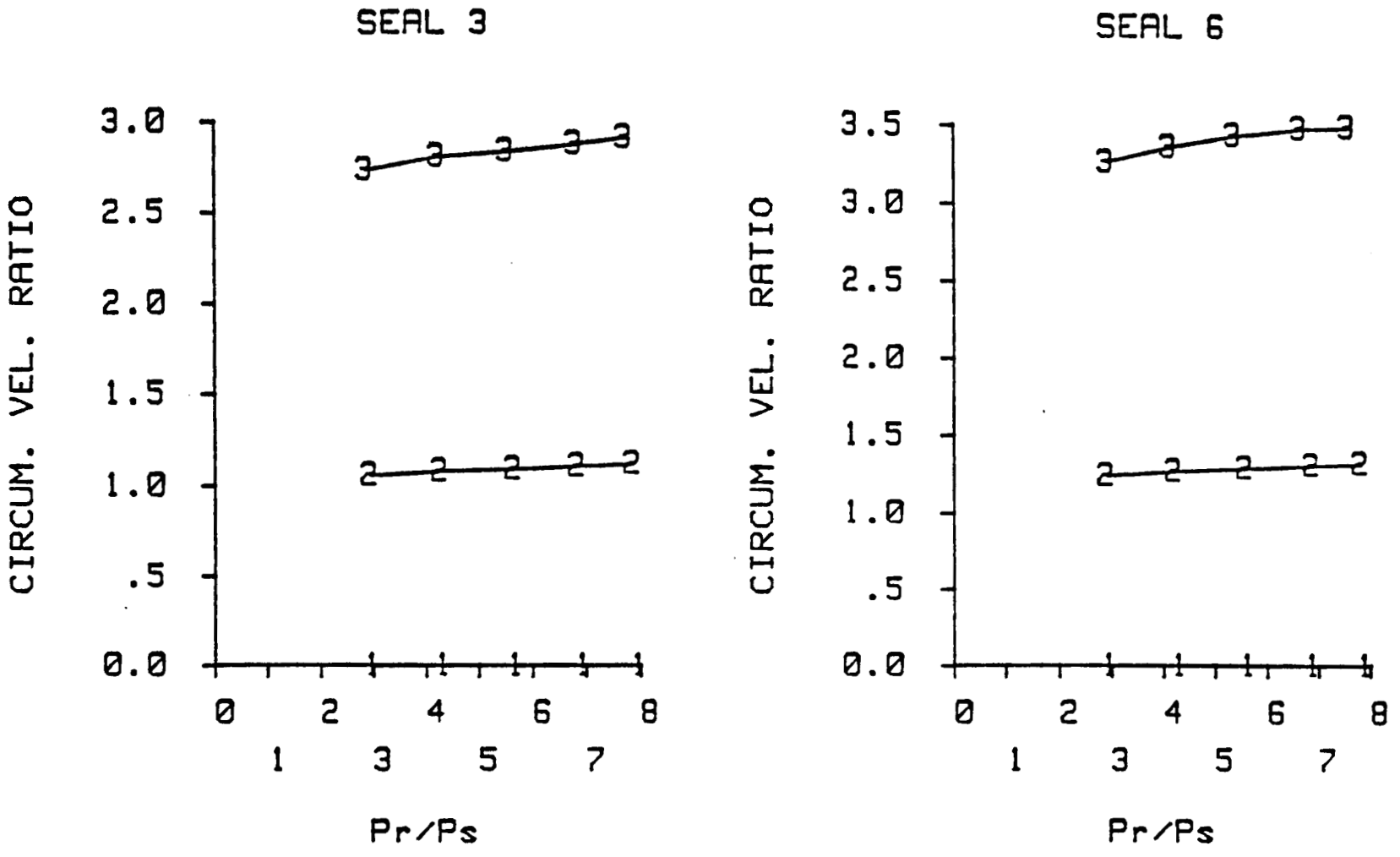

Figure 22. Inlet circumferential velocity ratios for seals 3 & 6. Inlet circumferential velocities 1–3 are plotted (see Table 2). Honeycomb stator (left), smooth stator (right).

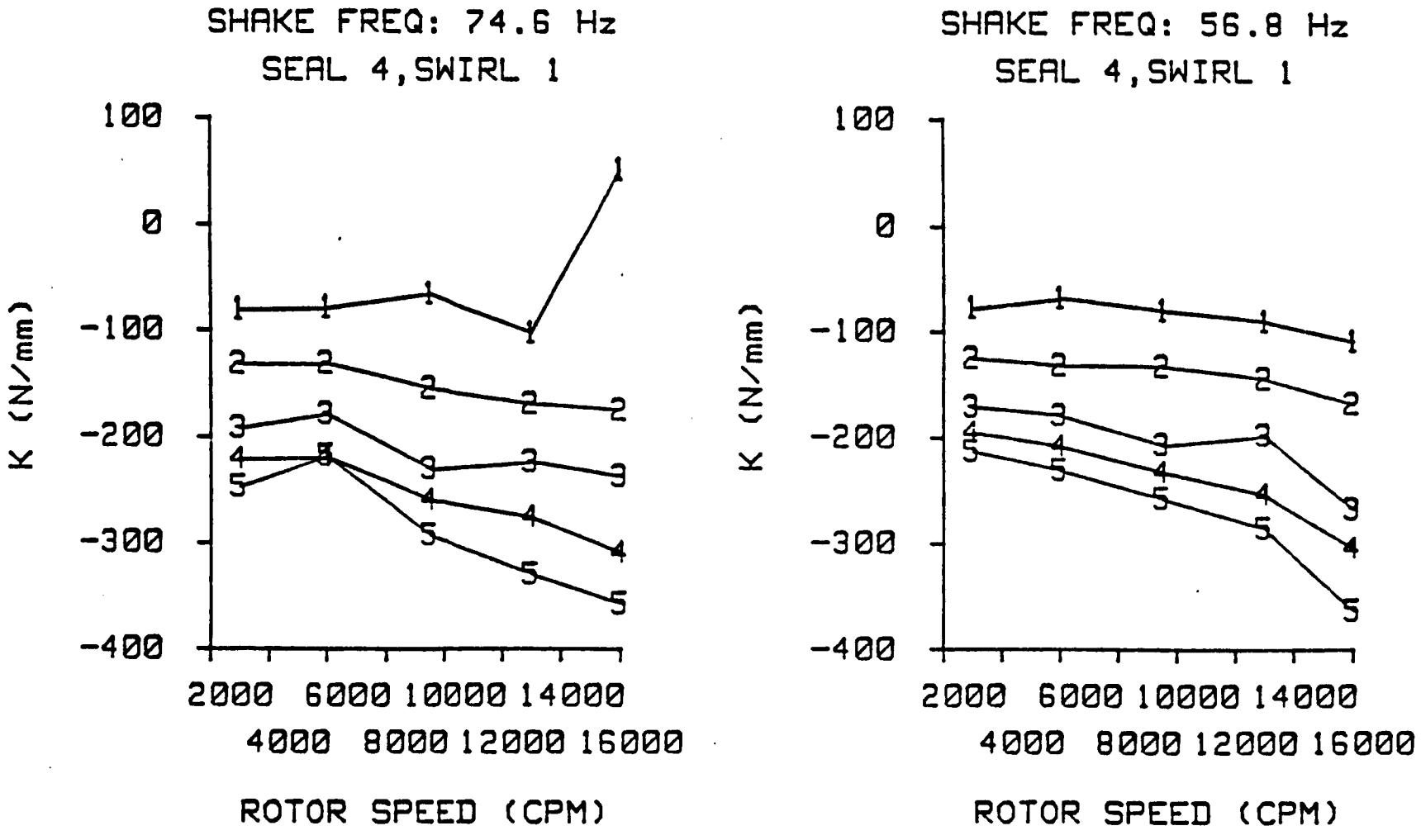

Figure 23. Direct stiffness versus rotor speed for seal 4 and inlet circumferential velocity 1. Shake frequency 74.6 Hz (left), shake frequency 56.8 Hz (right).

the 74.6 Hz shake frequency. The right hand plot contains data taken at the 56.8 Hz shake frequency. Corresponding data points in the two plots are essentially the same, except for the data point mentioned above.

INTERDEPENDENCE OF PRIMARY VARIABLES

In any experiment, each primary variable should be varied independently and any other parameters that might affect the result should be controlled. In this study, rotor speed, supply pressure, inlet circumferential velocity, shake frequency, and clearance are primary variables. Rotor speed, supply pressure and shake frequency can be adjusted independently as desired and therefore are not of concern. Inlet circumferential velocity is set by using different inlet swirl vane configurations. The vane configurations are fixed; therefore, inlet circumferential velocity is adjusted by installing different swirl vanes in the test rig. Unfortunately, this prevents adjustment of inlet velocity during a test. Seal clearance is adjusted by using different seal stators having different inside diameters. As with inlet circumferential velocity, seal clearance can only be varied over fixed values. Figures 24 and 25 show the effect of changing the seal clearance on circumferential velocity ratio. The change is quite substantial over the range that clearance is varied in these tests. Clearance also changes with rotor speed, due to rotor centrifugal and thermal growth. Table 3 shows the effect of rotor speed on rotor diameter. This effect begins to be important only at the highest rotor speed.

The rotordynamic coefficients cannot be plotted versus clearance because the inlet circumferential velocity changes substantially when the clearance is changed. The effect of clearance is displayed by plotting the coefficients versus

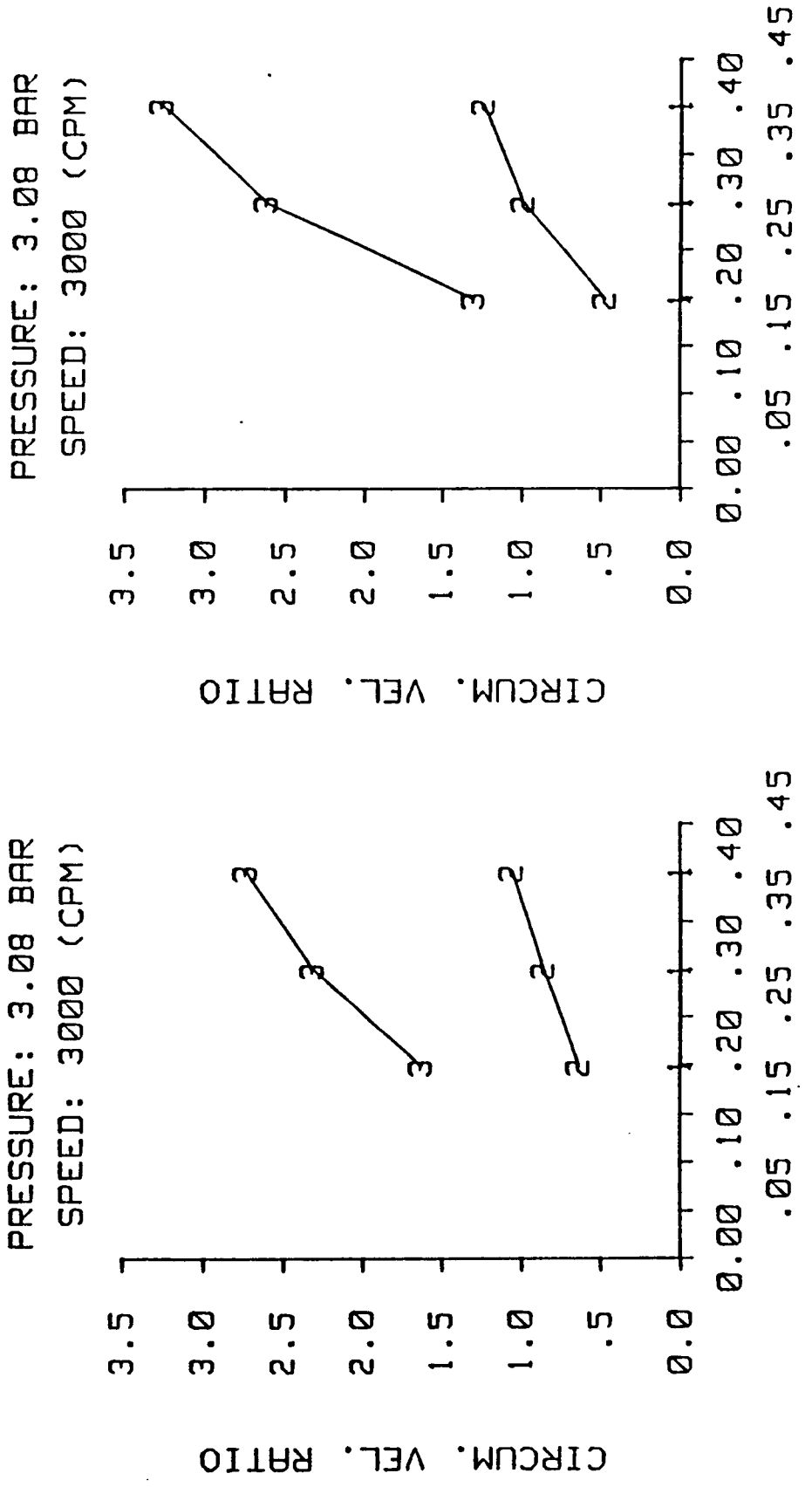

Figure 24. Inlet circumferential velocity ratio versus radial seal clearance for inlet pressure of 3.08 bar and rotor speed of 3000 cpm. Inlet circumferential velocities 1–3 are plotted (see Table 2). Honeycomb stator (left), smooth stator (right).

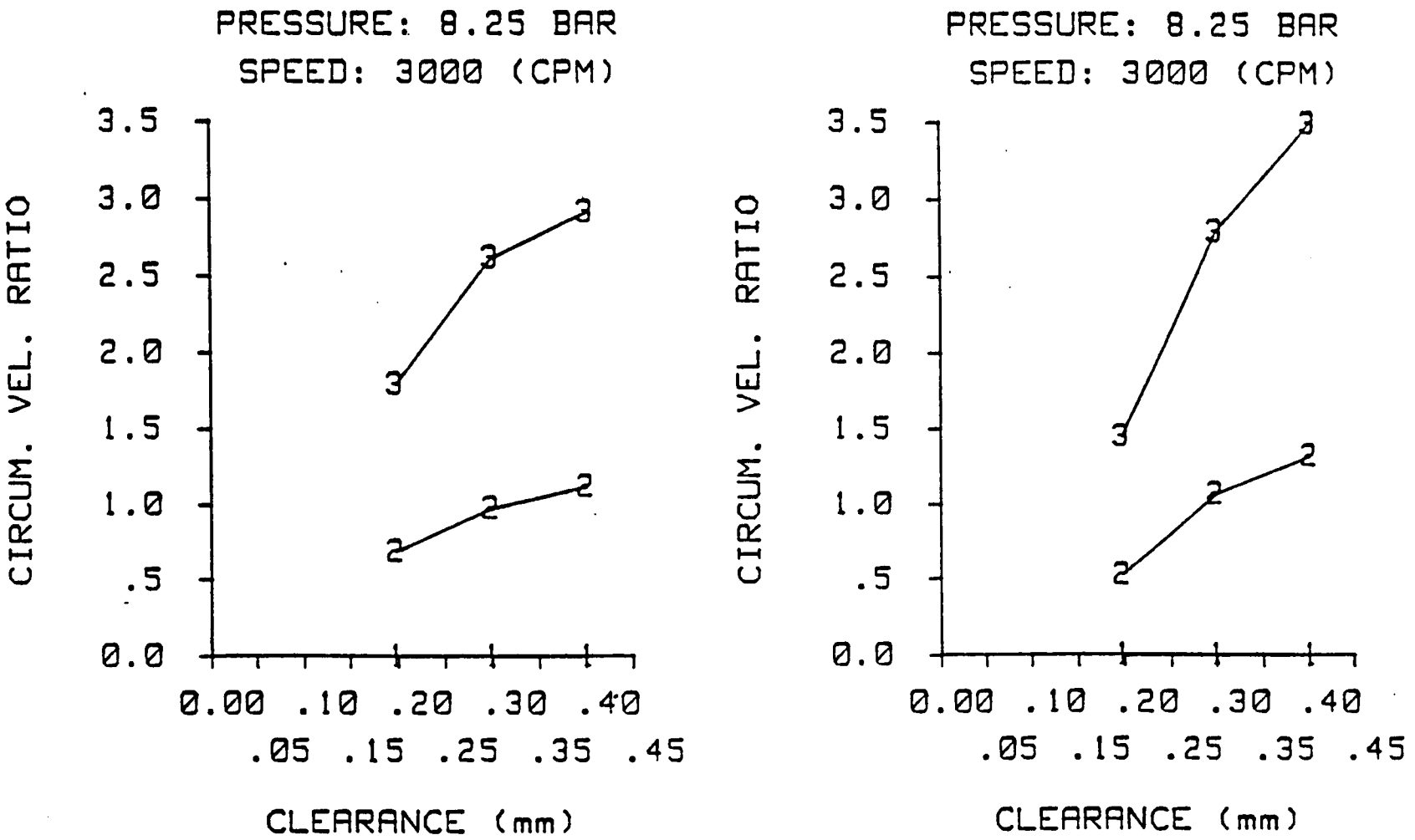

Figure 25. Inlet circumferential velocity ratio versus radial seal clearance for inlet pressure of 8.25 bar and rotor speed of 3000 cpm. Inlet circumferential velocities 1–3 are plotted (see Table 2). Honeycomb stator (left), smooth stator (right).

inlet circumferential velocity for each seal on the same plot. This procedure allows only one rotor speed and one supply pressure per plot. Data are presented for the highest and lowest rotor speed and the highest and lowest pressure.

UNCERTAINTY ANALYSIS

The uncertainty of the rotordynamic coefficients was calculated using the method described by Holman [21] for estimating the uncertainty in a calculated result based on the uncertainties in primary measurements. The uncertainty w_R in a result R which is a function of n primary measurements $x_1, x_2, x_3 ... x_n$ with uncertainties $w_1, w_2, w_3 ... w_n$ is

$$w_R = \left[\left(\frac{\partial R}{\partial x_1} w_1 \right)^2 + \left(\frac{\partial R}{\partial x_2} w_2 \right)^2 + \cdots + \left(\frac{\partial R}{\partial x_n} w_n \right)^2 \right]^{1/2}.$$

Since the rotordynamic coefficients are calculated using equation (6), the primary measurements are forces, displacements, and frequency. The uncertainty in these measurements on the TAMU test apparatus are 0.89 N (0.2 lb), 0.0013 mm (0.05 mils), and 0.13 Hz, respectively. For the six seals tested, the maximum uncertainties in the stiffness and damping coefficients were 15 N/mm (86 lb/in) and 32 N-s/m (0.18 lb-s/in), respectively.The uncertainty in the cross-coupled damping coefficients are of the same order of magnitude as the coefficients themselves. Since the uncertainties in the cross-coupled damping values are so high, and since the cross-coupled damping forces are of minor significance compared to other damping and stiffness forces, comparisons of the cross-coupled damping coefficients are omitted from this report.

SELECTION OF REPORT DATA

Test results are presented for the labyrinth-rotor/honeycomb-stator and labyrinth-rotor/smooth-stator seal configurations. There are 225 data points at the 74.6 Hz shake frequency for each configuration. Data were selected for the report as described below. The remaining data are included in the Appendix.

Leakage data are presented as a function of clearance. Whirl frequency ratio is presented as a function of rotor speed and seal clearance. The following four types of plots are given for each rotordynamic coefficient:

1) Rotor speed dependence – coefficient versus rotor speed for various pressures. Data are presented for smallest clearance (seals 1 & 4) and highest circumferential velocity (swirl 3).

2) Circumferential velocity dependence – coefficient versus circumferential velocity ratio for various pressures. Data are presented for smallest clearance (seals 1 & 4) and highest rotor speed (16,000 cpm).

3) Pressure dependence – coefficient versus pressure for various rotor speeds. Data are presented for smallest clearance (seals 1 & 4) and highest circumferential velocity (swirl 3).

4) Clearance dependence – coefficient versus circumferential velocity ratio for various clearances. Four plots are presented, each with a different fixed rotor speed and pressure.

Additional plots are included where they provide additional information.

CHAPTER V

TEST RESULTS

In this chapter, experimental results are presented for the labyrinth-rotor/honeycomb-stator seal configuration, and compared to the labyrinth-rotor/smooth-stator results. Leakage data are presented first, followed by direct stiffness, cross-coupled stiffness, direct damping, and whirl frequency ratio. The following rules apply to all figures except those containing leakage data: (1) honeycomb stator results are shown on the left hand side of each figure, (2) smooth stator results are shown on the right hand side of each figure, and (3) symbols in the figures are defined in table 1, table 2, and figures 20–22.

LEAKAGE

Leakage is represented by the flow coefficient,

$$\Phi = \frac{\dot{m}\sqrt{RT_r}}{\pi D C_r P_r}.$$

Figures 26–29 are plots of flow coefficient versus seal clearance for different values of pressure and rotor speed. In each plot, curve 1 represents the honeycomb stator seals and curve 4 represents the smooth stator seals. Leakage did not vary with inlet circumferential velocity ratio, thus the data presented are for inlet circumferential velocity 1 only. Examination of the four figures reveals that the honeycomb stator seal leaks more at the smallest clearance and the smooth stator seal leaks more at the largest clearance. Also, leakage increases as inlet pressure increases. These results are consistent with those of Stocker et al. [22].

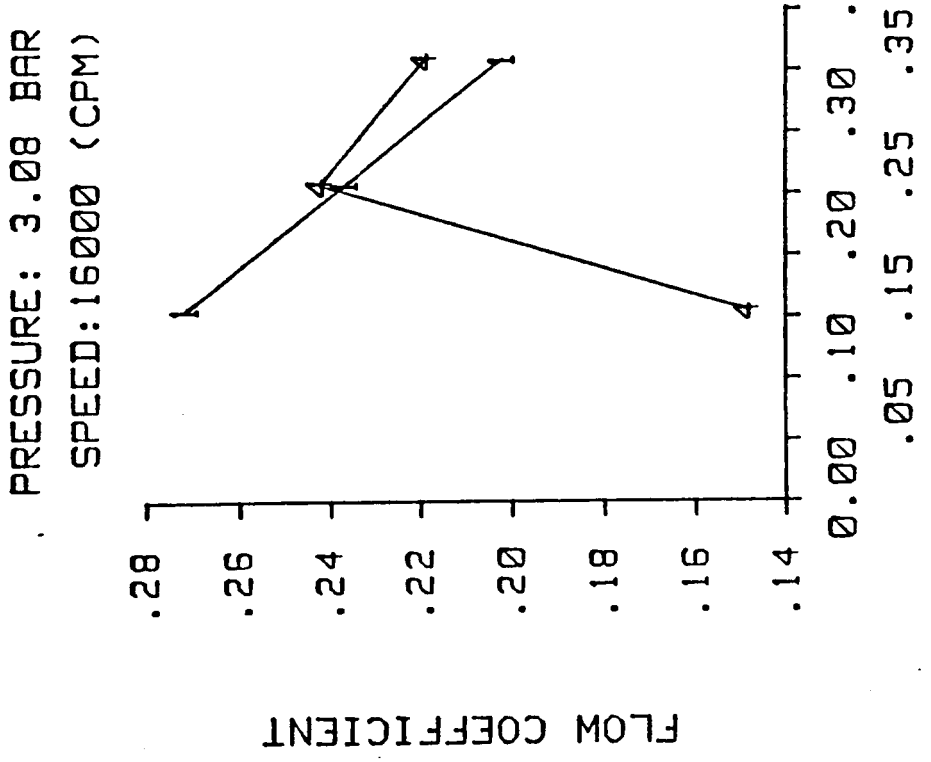

Figure 27. Flow coefficient versus radial seal clearance for inlet pressure of 3.08 bar and rotor speed of 16000 cpm. Curve 1 represents honeycomb stator seals and curve 4 represents smooth stator seals.

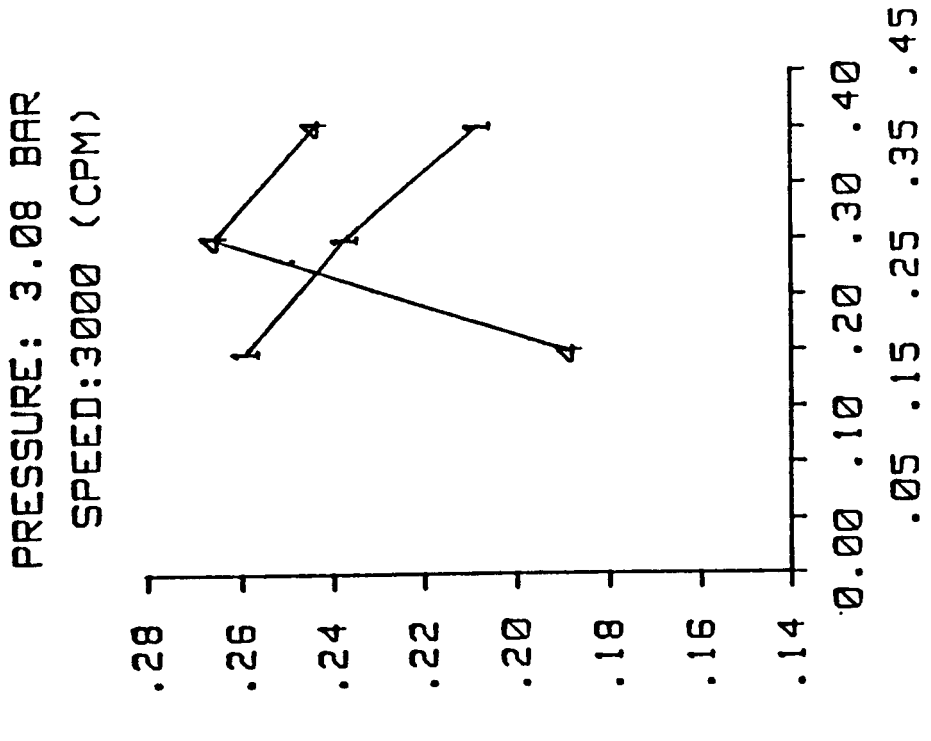

Figure 26. Flow coefficient versus radial seal clearance for inlet pressure of 3.08 bar and rotor speed of 3000 cpm. Curve 1 represents honeycomb stator seals and curve 4 represents smooth stator seals.

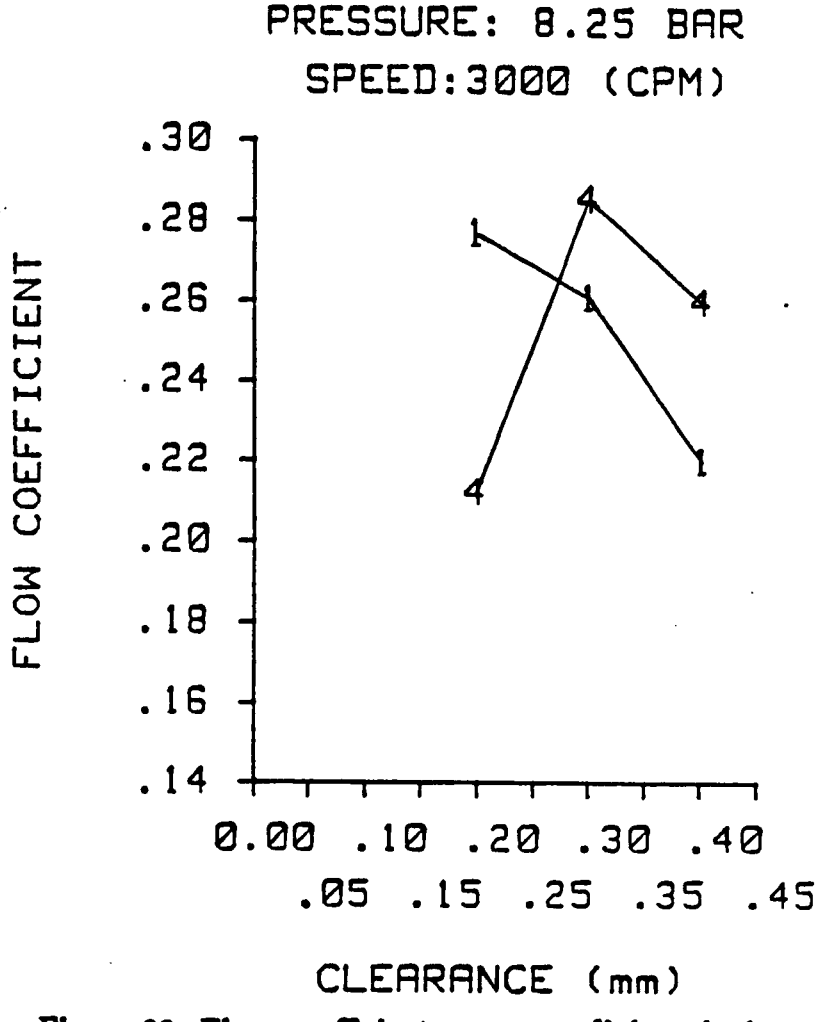

Figure 28. Flow coefficient versus radial seal clearance for inlet pressure of 8.25 bar and rotor speed of 3000 cpm. Curve 1 represents honeycomb stator seals and curve 4 represents smooth stator seals.

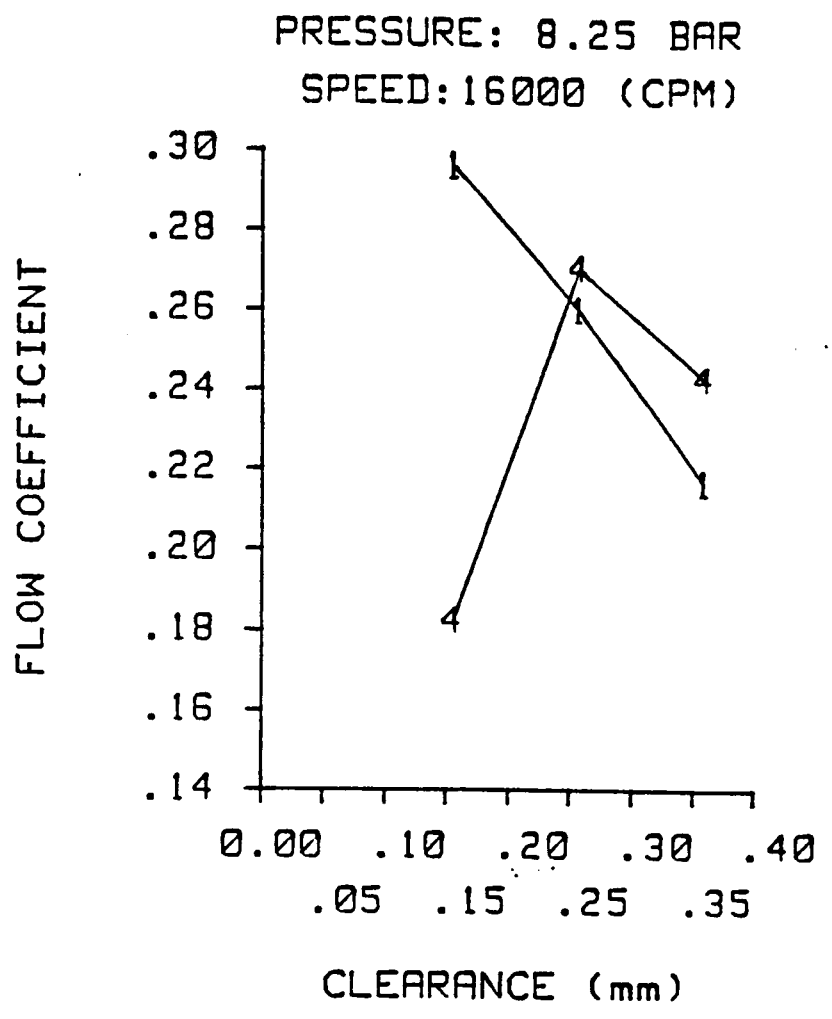

Figure 29. Flow coefficient versus radial seal clearance for inlet pressure of 8.25 bar and rotor speed of 16000 cpm. Curve 1 represents honeycomb stator seals and curve 4 represents smooth stator seals.

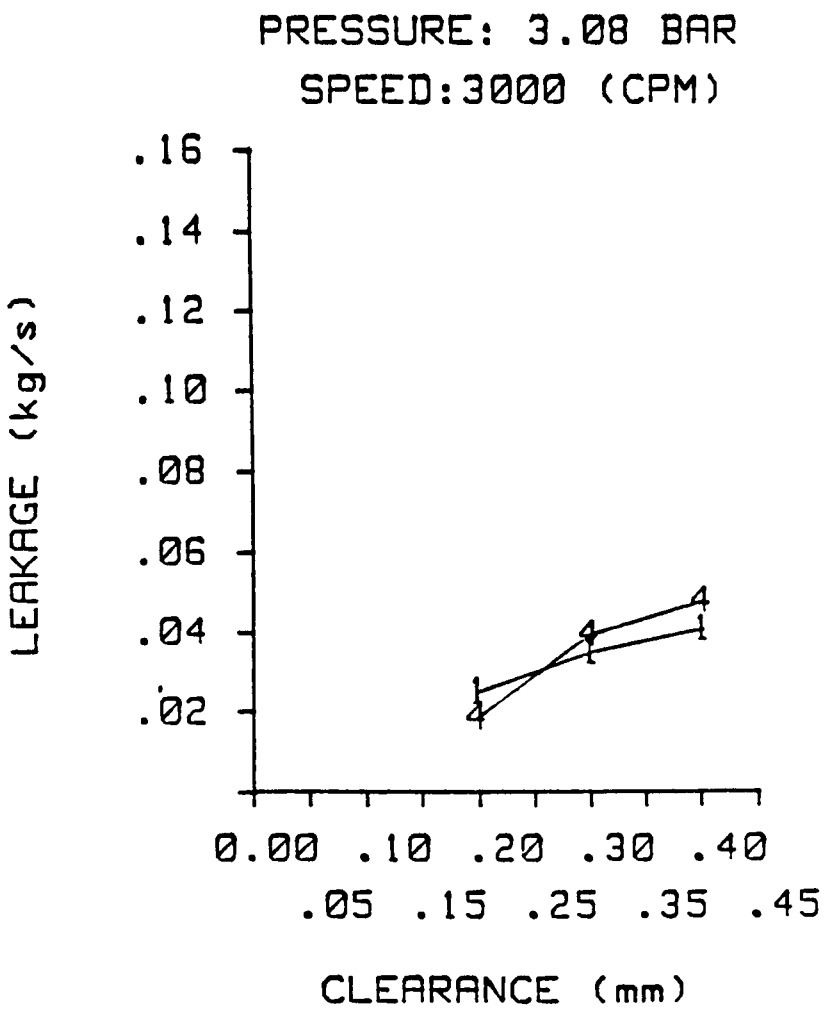

Figure 30. Leakage versus radial seal clearance for inlet pressure of 3.08 bar and rotor speed of 3000 cpm. Curve 1 represents honeycomb stator seals and curve 4 represents smooth stator seals.

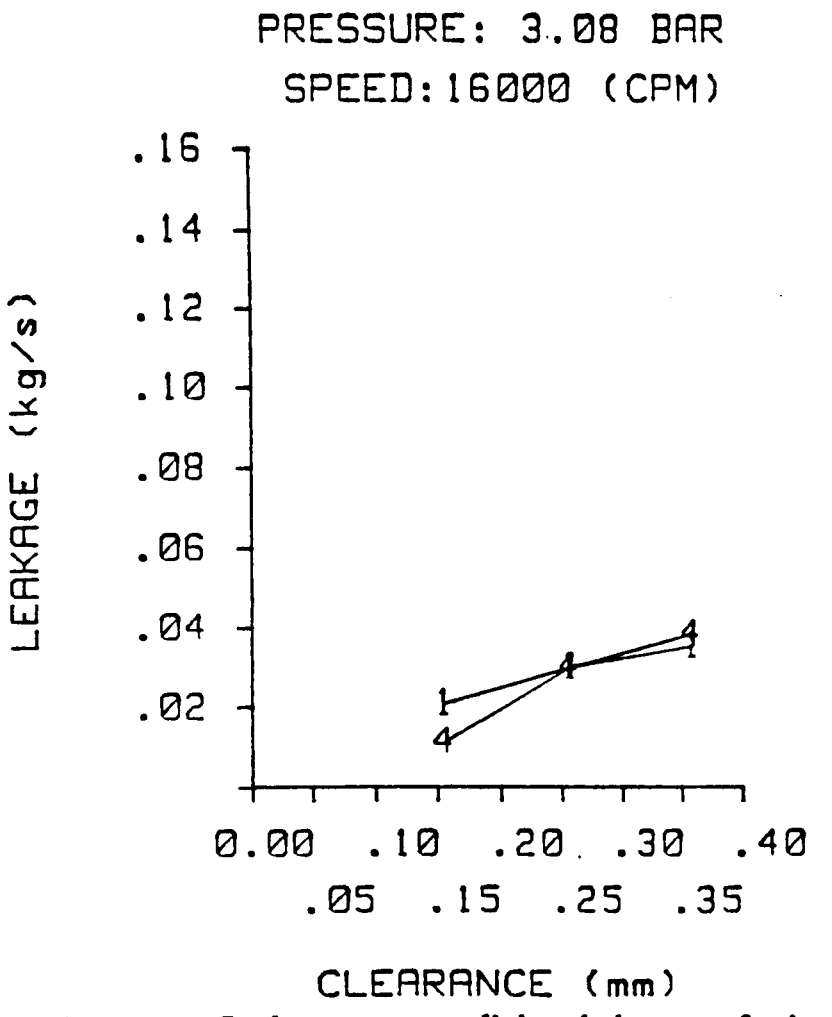

Figure 31. Leakage versus radial seal clearance for inlet pressure of 3.08 bar and rotor speed of 16000 cpm. Curve 1 represents honeycomb stator seals and curve 4 represents smooth stator seals.

Figure 30 and 31 are similar to figures 26 and 27, except they represent leakage by the dimensional mass flow rate. These figures show that leakage increases as clearance increases. Leakage also decreases slightly as rotor speed increases because of the loss of clearance with rotor speed discussed previously.

DIRECT STIFFNESS

Direct stiffness is plotted versus rotor speed for various pressures in figure 32. The left hand plot is for seal 1, the honeycomb stator seal with the smallest clearance. The right hand plot is for seal 4, the smooth stator seal with the smallest clearance. The direct stiffness is negative and shows a small increase in magnitude with rotor speed. The smooth stator seal has a similar characteristic, but has a larger direct stiffness magnitude. Direct stiffness is plotted versus circumferential velocity ratio for various pressures in figure 33. Direct stiffness evidently does not depend on the magnitude of inlet circumferential velocity for either stator surface. Direct stiffness is plotted versus pressure ratio across the seal for various rotor speeds in figure 34. Magnitude of direct stiffness increases as pressure increases for both stator surfaces. The trends in direct stiffness are the same for all three clearances tested. Data for seals 2,3,5 and 6 are given in the Appendix.

The next four plots, figures 35–38, show direct stiffness versus circumferential velocity ratio. Data for three seals are shown on each plot. These plots are used to show the effect of clearance on direct stiffness. Figure 35, for a pressure of 3.08 bar and a rotor speed of 3000 cpm, shows that the direct stiffness magnitude increases as clearance increases for the honeycomb stator seals. However, for the smooth stator seals, direct stiffness decreases in magnitude as clearance

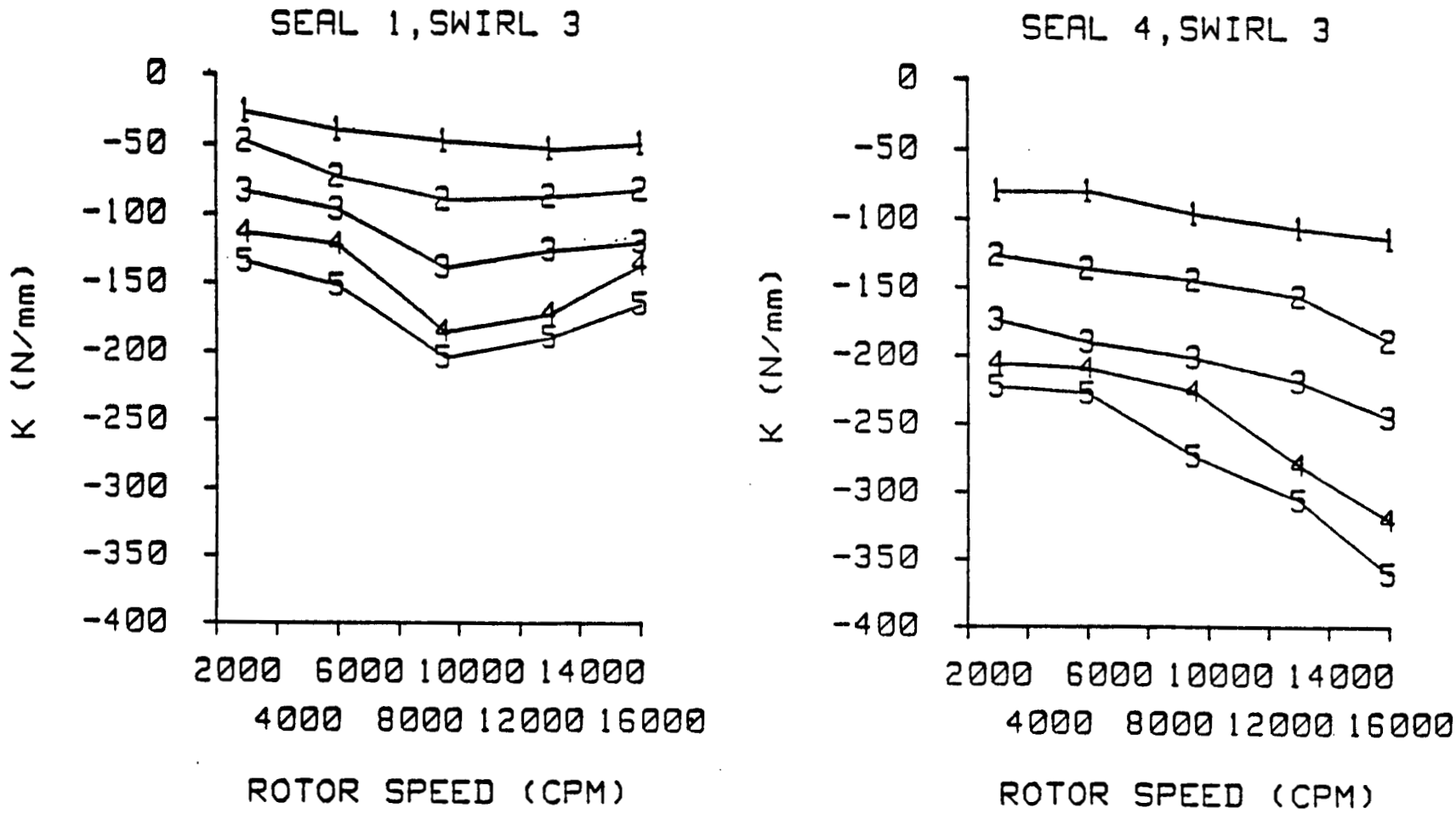

Figure 32. Direct stiffness versus rotor speed for seals 1 & 4 and inlet circumferential velocity 3. Inlet pressures 1–5 are plotted (see Table 2). Honeycomb stator (left), smooth stator (right).

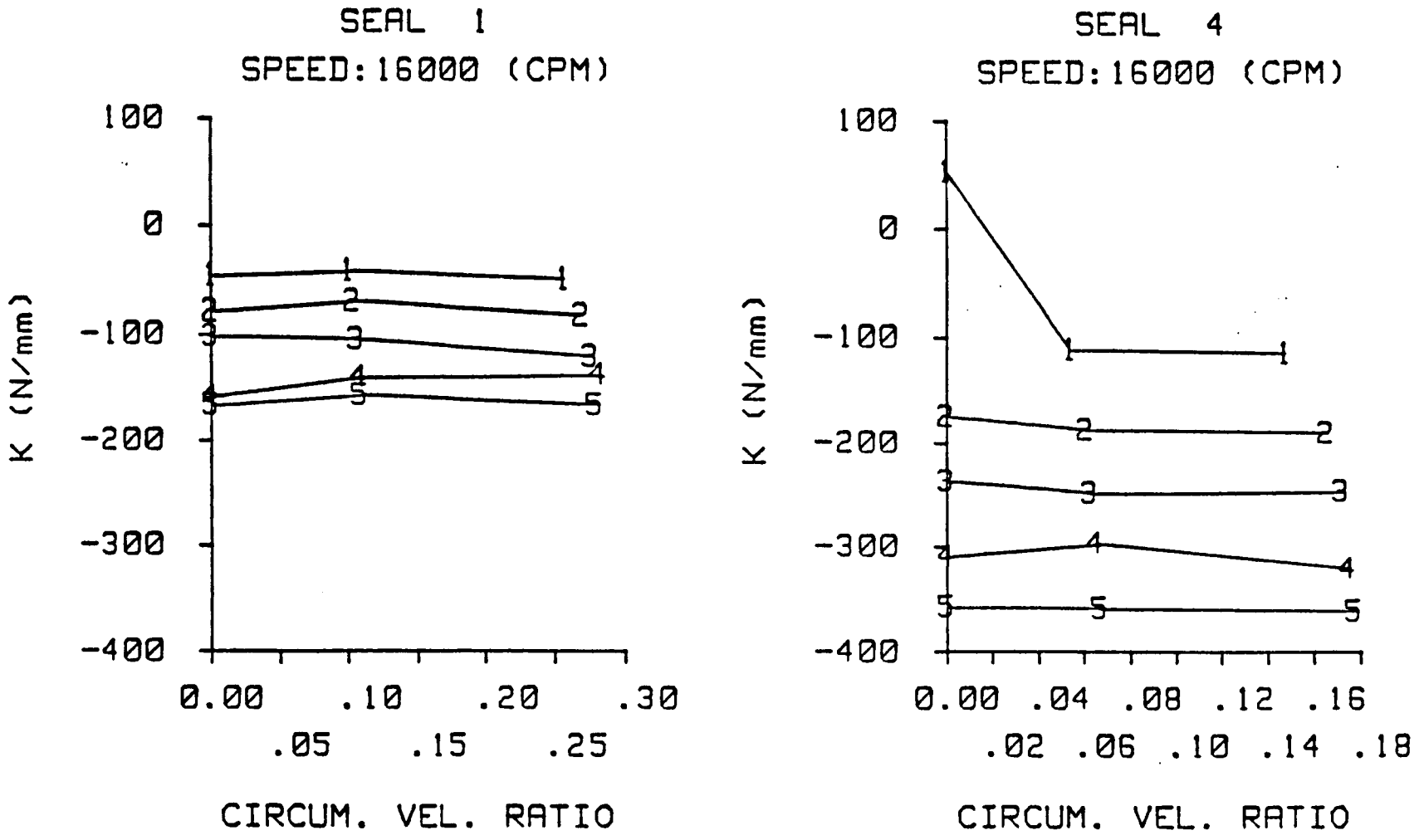

Figure 33. Direct stiffness versus inlet circumferential velocity ratio for seals 1 & 4 and rotor speed of 16000 cpm. Inlet pressures 1–5 are plotted (see Table 2). Honeycomb stator (left), smooth stator (right).

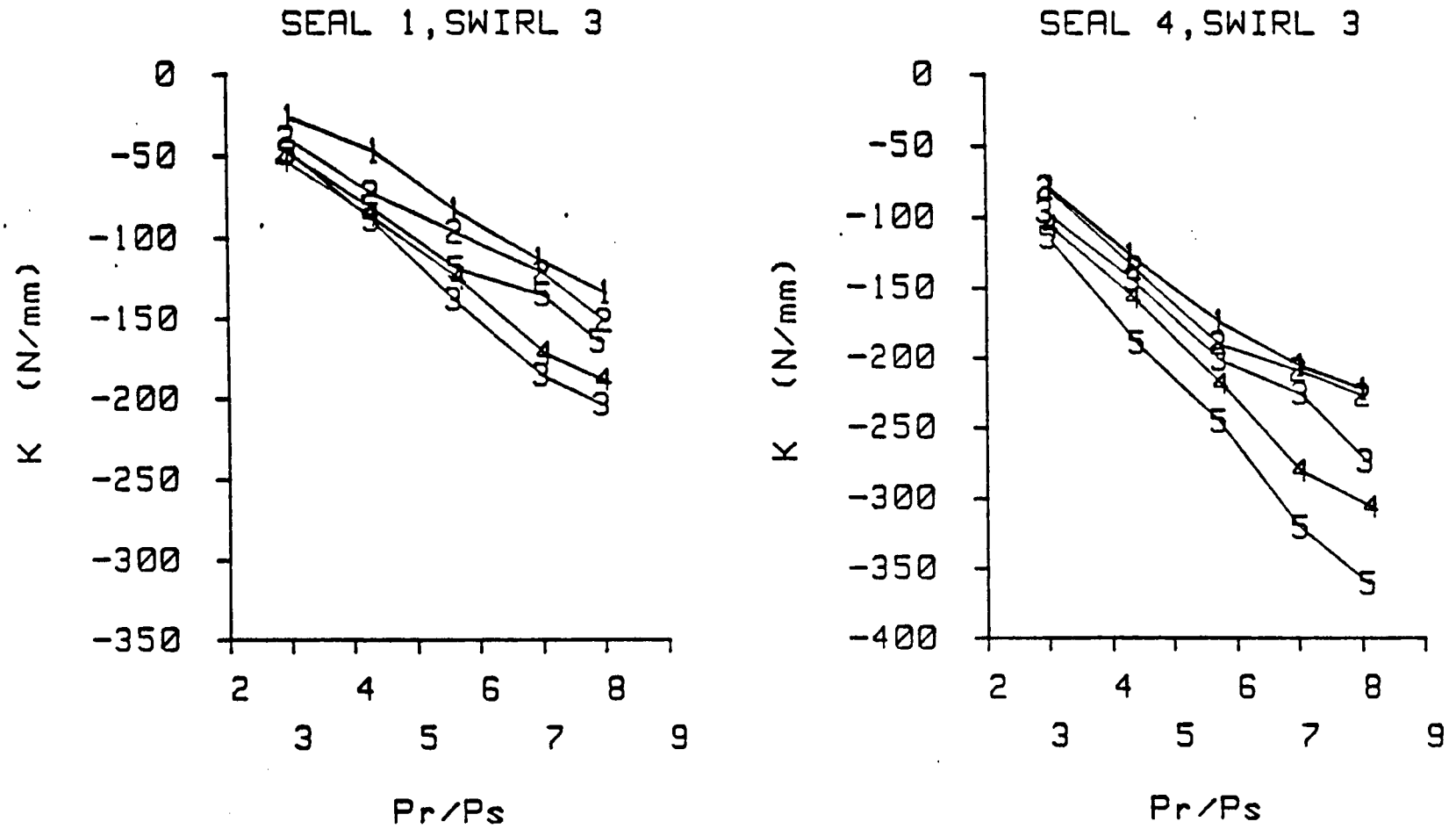

Figure 34. Direct stiffness versus inlet pressure ratio for seals 1 & 4 and inlet circumferential velocity 3. Rotor speeds 1–5 are plotted (see Table 2). Honeycomb stator (left), smooth stator (right).

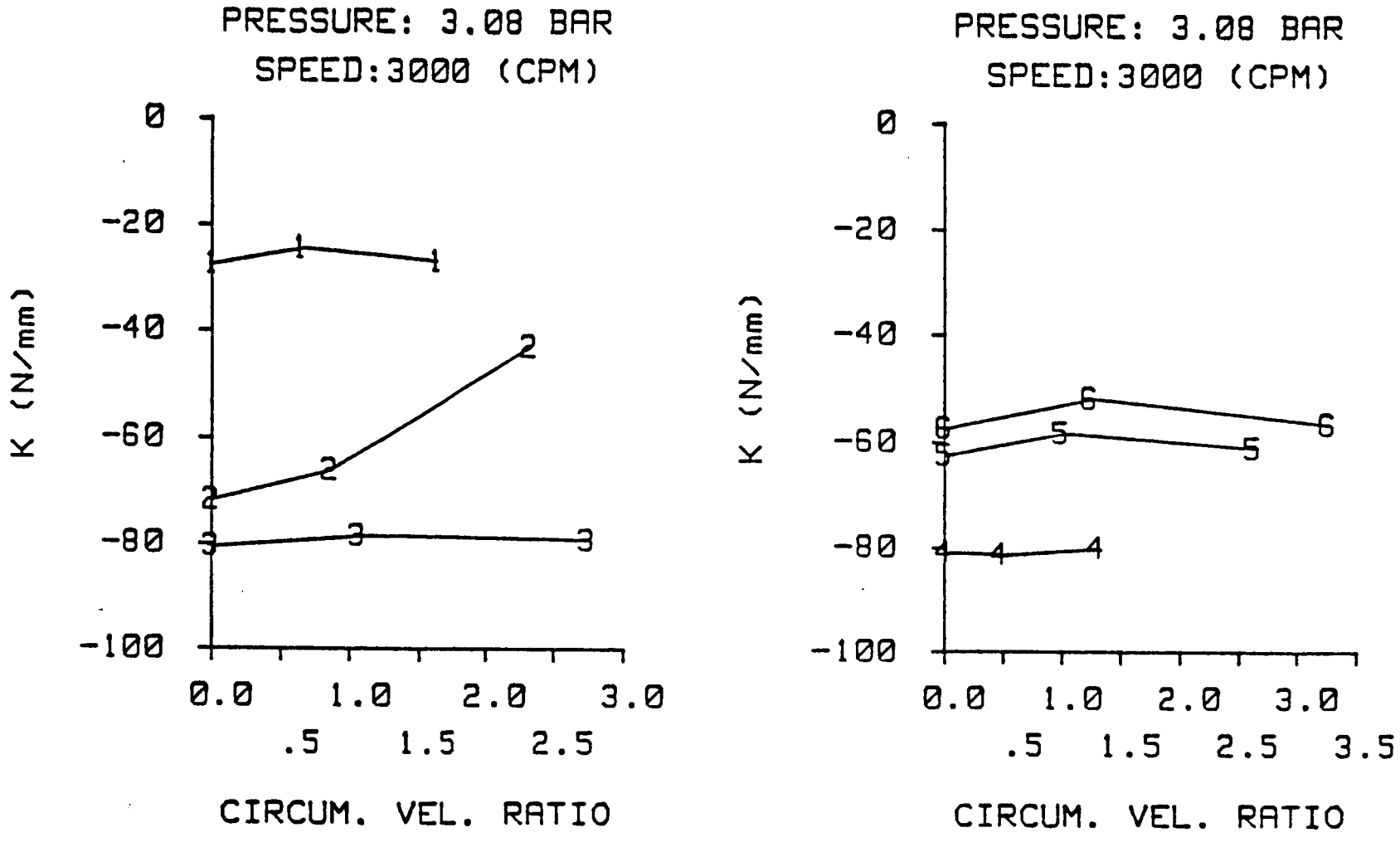

Figure 35. Direct stiffness versus inlet circumferential velocity ratio for inlet pressure of 3.08 bar and rotor speed of 3000 cpm. Three clearances are plotted (see Table 1). Honeycomb stator (left), smooth stator (right).

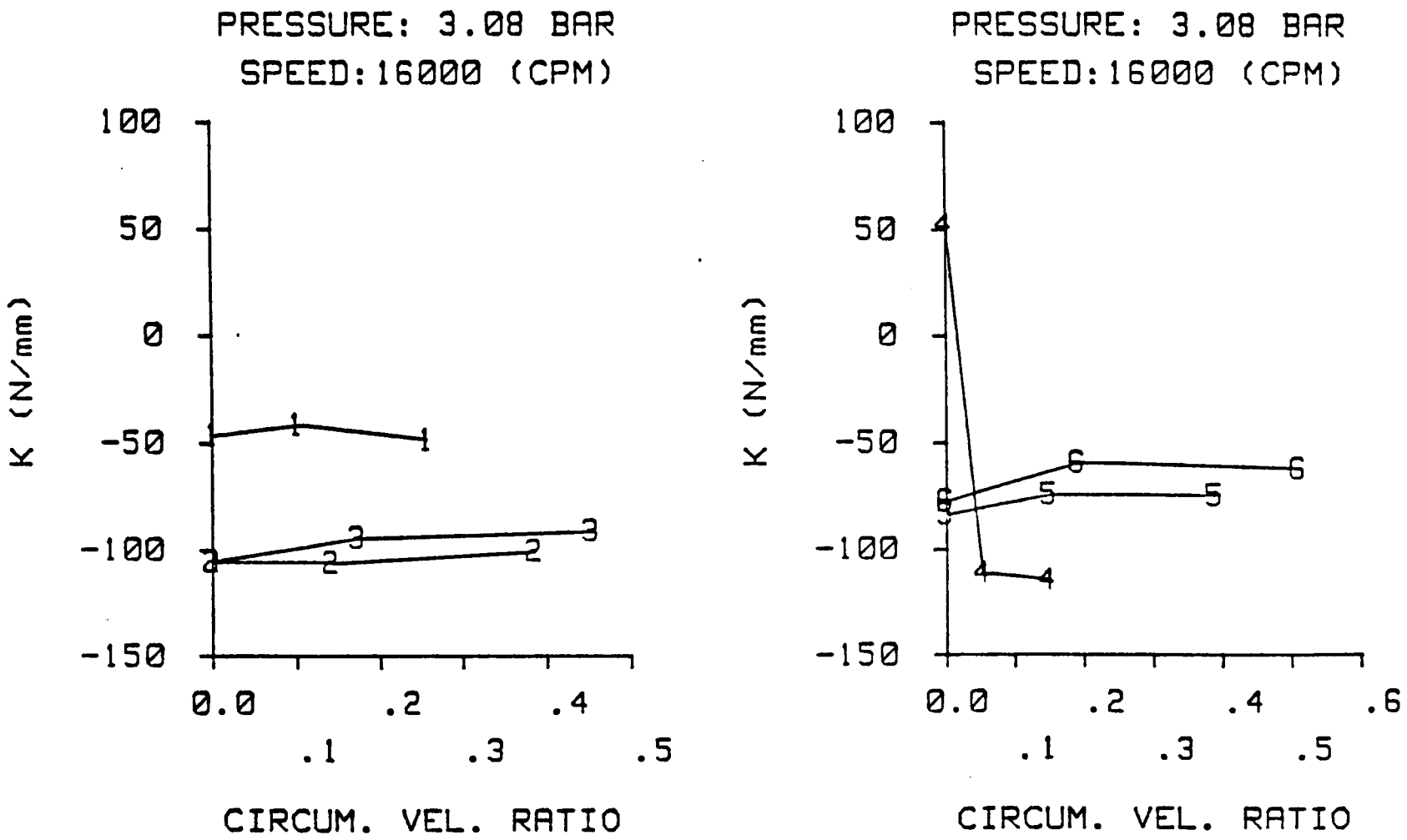

Figure 36. Direct stiffness versus inlet circumferential velocity ratio for inlet pressure of 3.08 bar and rotor speed of 16000 cpm. Three clearances are plotted (see Table 1). Honeycomb stator (left), smooth stator (right).

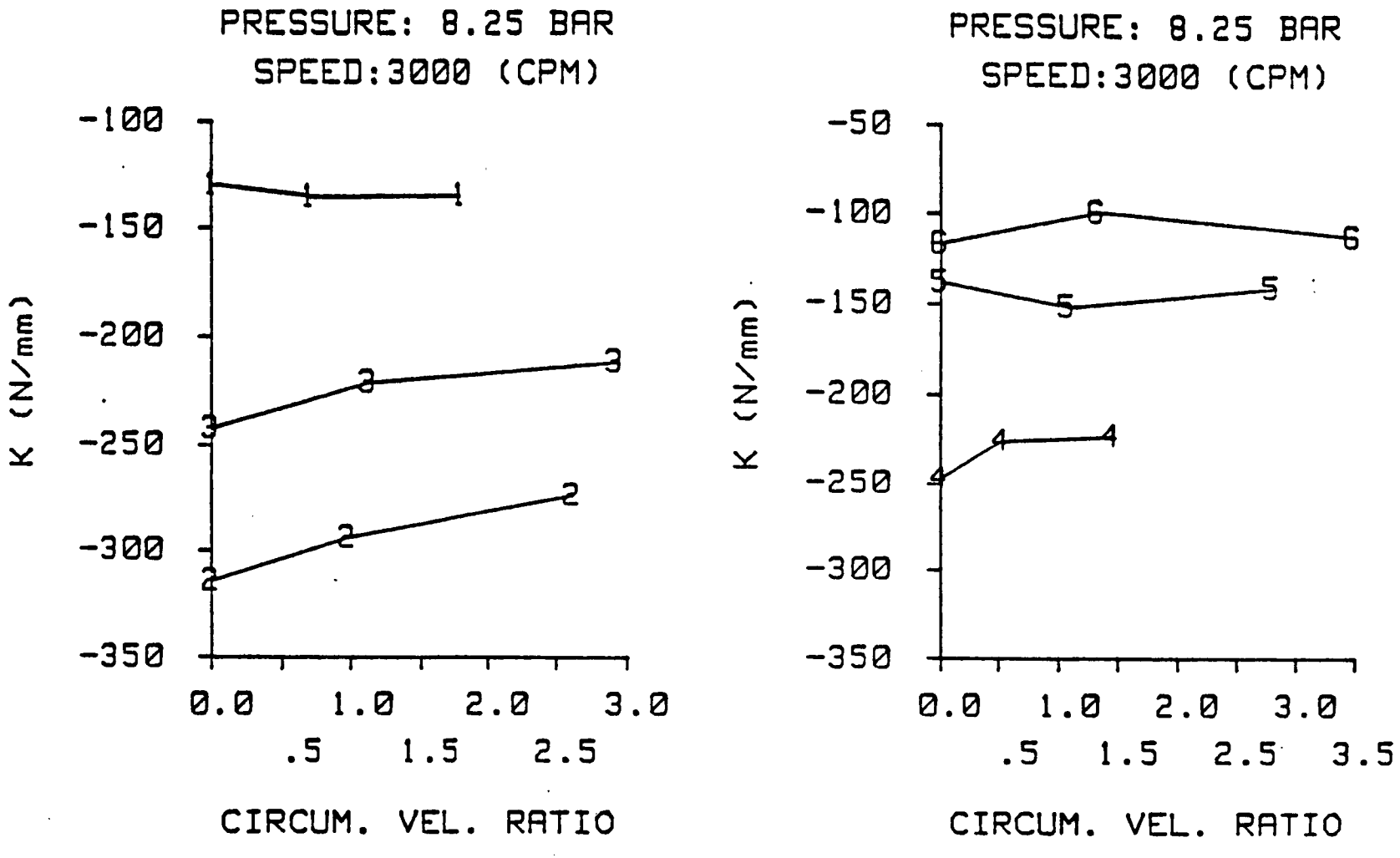

Figure 37. Direct stiffness versus inlet circumferential velocity ratio for inlet pressure of 8.25 bar and rotor speed of 3000 cpm. Three clearances are plotted (see Table 1). Honeycomb stator (left), smooth stator (right).

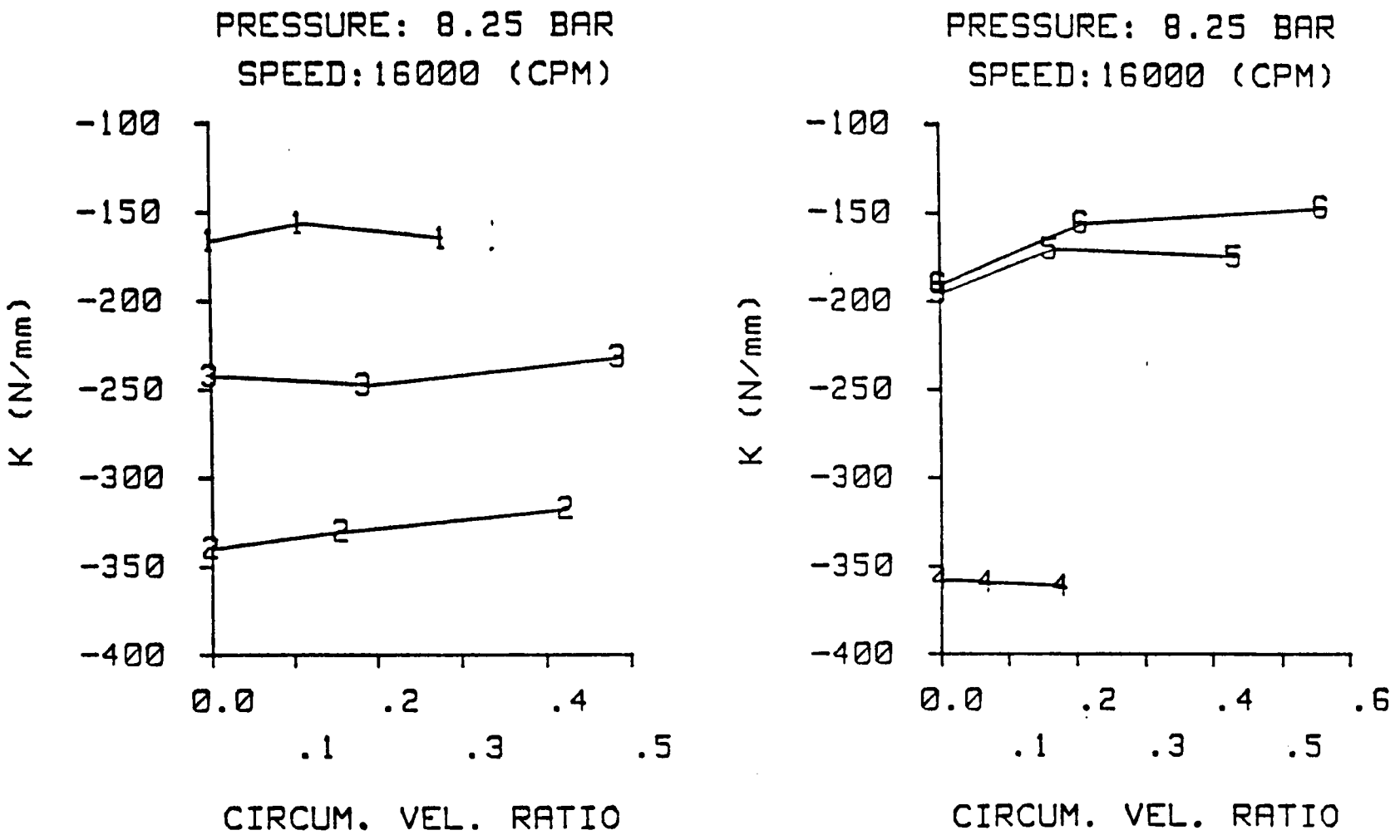

Figure 38. Direct stiffness versus inlet circumferential velocity ratio for inlet pressure of 8.25 bar and rotor speed of 16000 cpm. Three clearances are plotted (see Table 1). Honeycomb stator (left), smooth stator (right).

increases. The smooth seal result agrees with intuition; one would expect the direct stiffness to tend toward zero as clearance becomes large. Also, due to the opposing trends, the honeycomb stator seal has the larger direct stiffness magnitude at large clearance and the smooth stator seal has the larger direct stiffness magnitude at small clearance. In figure 36, for the same pressure and a rotor speed of 16,000 cpm, the trend of figure 35 for the honeycomb stator seal appears to be reversing. Seal 2 has a much larger direct stiffness than seal 1, but seal 3, the largest clearance seal, has a smaller direct stiffness than seal 2. The smooth stator seal has the same direct stiffness versus clearance trend regardless of rotor speed. Figures 37 and 38 are similar to figure 35 and 36 except that the pressure is 8.25 bar. The change in direct stiffness with clearance follows the trend of figure 36. The magnitudes of direct stiffness are larger than those in figures 35 and 36 due to the higher pressure.

CROSS-COUPLED STIFFNESS

Cross-coupled stiffness is plotted versus rotor speed for various pressures in figure 39. Cross-coupled stiffness increases with rotor speed for both seals. For the honeycomb stator seal, cross-coupled stiffness is negative at low speed and increases to about 300 N/mm at the highest rotor speed. For the smooth stator seal, cross-coupled stiffness has a small positive value at low rotor speeds, increasing to about 350 N/mm at the highest rotor speed. Due to the results of Elrod and Childs [14], cross-coupled stiffness was expected to be less positive for the honeycomb stator seal compared to the smooth stator seal for all rotor speeds. The data show that the cross-coupled stiffness of the two seals have similar magnitudes at high rotor speeds.

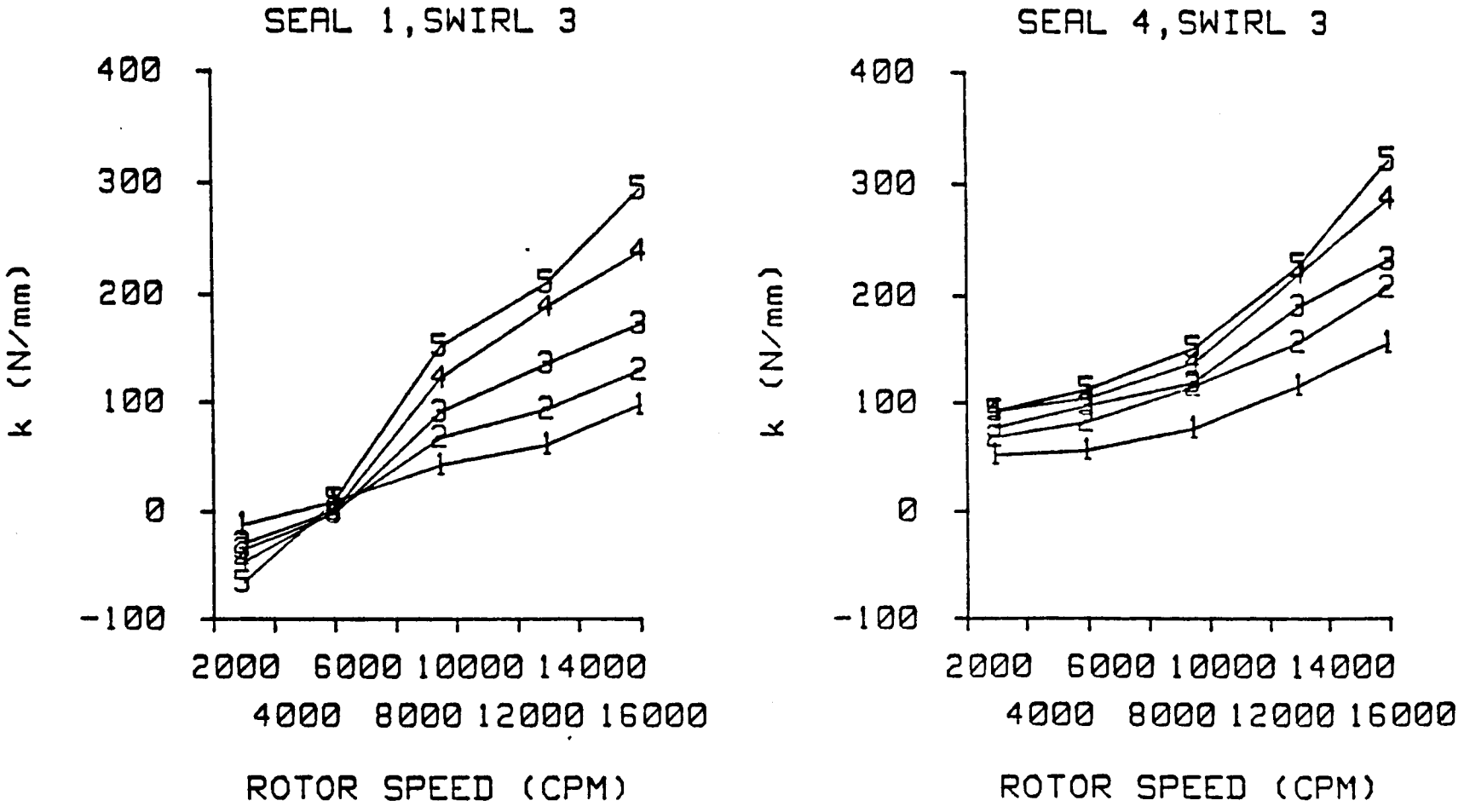

Figure 39. Cross-coupled stiffness versus rotor speed for seals 1 & 4 and inlet circumferential velocity 3. Inlet pressures 1–5 are plotted (see Table 2). Honeycomb stator (left), smooth stator (right).

The comparisons of cross-coupled stiffness versus rotor speed for seals 2 & 5 and seals 3 & 6 are somewhat different than for seals 1 & 4; therefore, these plots are included here. Figure 40 is the plot of cross-coupled stiffness versus rotor speed for seals 2 and 5. Note the cross-coupled stiffness begins to peak at 16,000 cpm for the honeycomb stator seal. The smooth stator seal shows a speed dependence only at the higher rotor speeds, whereas figure 39 (seal 4) shows a speed dependence at all rotor speeds. Again, the honeycomb stator seal has a cross-coupled stiffness that is better (negative or smaller magnitude) at low speeds, but worse (larger) at higher speeds. Figure 41 shows cross-coupled stiffness versus rotor speed for seals 3 & 6. In this plot, cross-coupled stiffness does not show a speed dependence for the smooth seal, whereas the trend for the honeycomb seal is the same as that of figure 40.

Figure 42 illustrates cross-coupled stiffness versus circumferential velocity for various pressures for seals 1 and 4.Cross-coupled stiffness increases significantly from zero inlet tangential velocity to the first positive value of inlet velocity for the honeycomb stator seal. However, from the first positive inlet velocity to the second positive inlet velocity, the cross-coupled stiffness increases only slightly or in some cases decreases. Cross-coupled stiffness in the smooth stator seal increases continuously as inlet circumferential velocity increases. Figure 43 is a plot of cross-coupled stiffness versus pressure ratio for various rotor speeds. For the honeycomb stator seal, cross-coupled stiffness decreases as pressure ratio increases at the two lowest rotor speeds. Cross-coupled stiffness increases as pressure ratio increases for the higher rotor speeds. In the smooth stator seal, cross-coupled stiffness increases as pressure ratio increases, regardless of rotor speed.

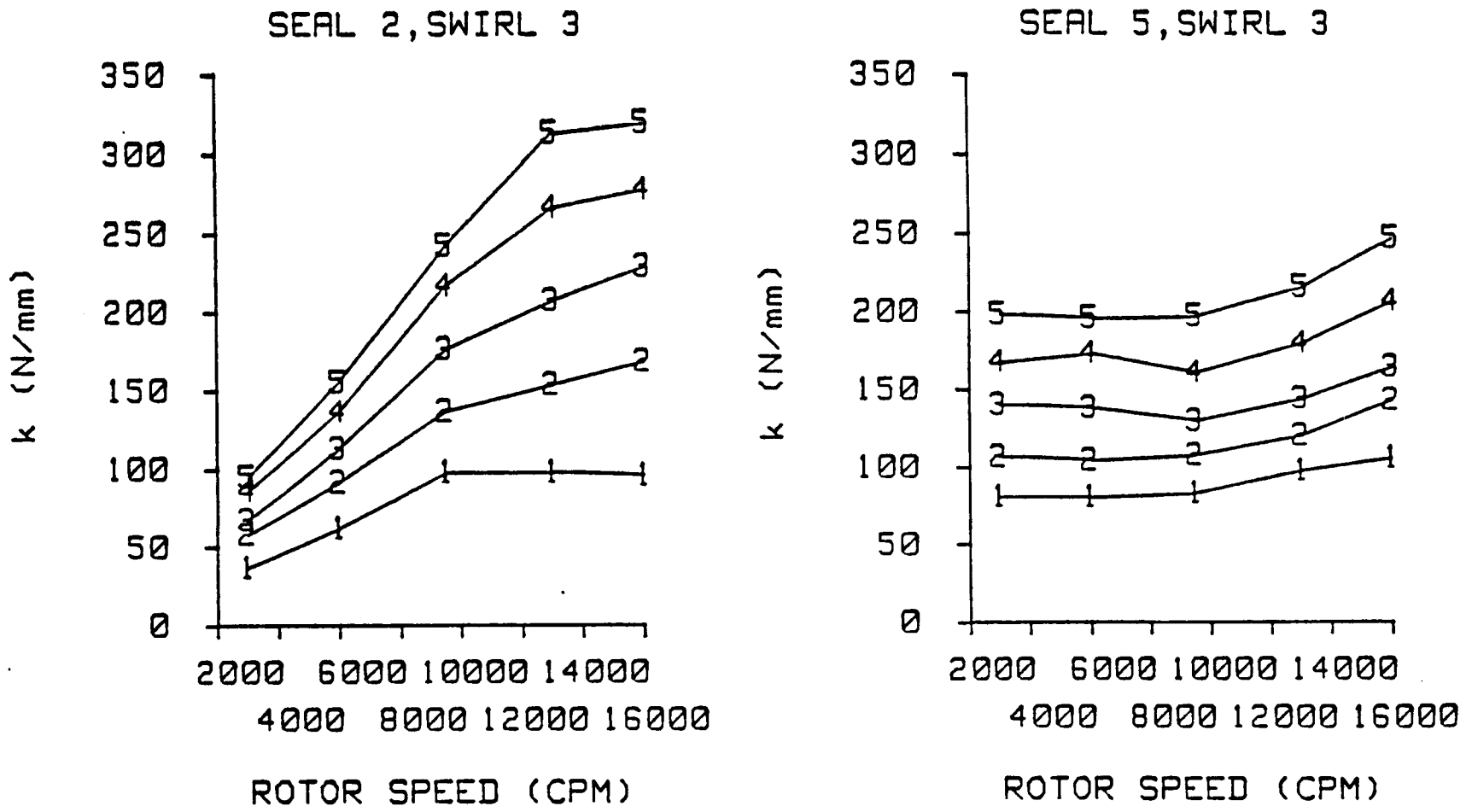

Figure 40. Cross-coupled stiffness versus rotor speed for seals 2 & 5 and inlet circumferential velocity 3. Inlet pressures 1–5 are plotted (see Table 2). Honeycomb stator (left), smooth stator (right).

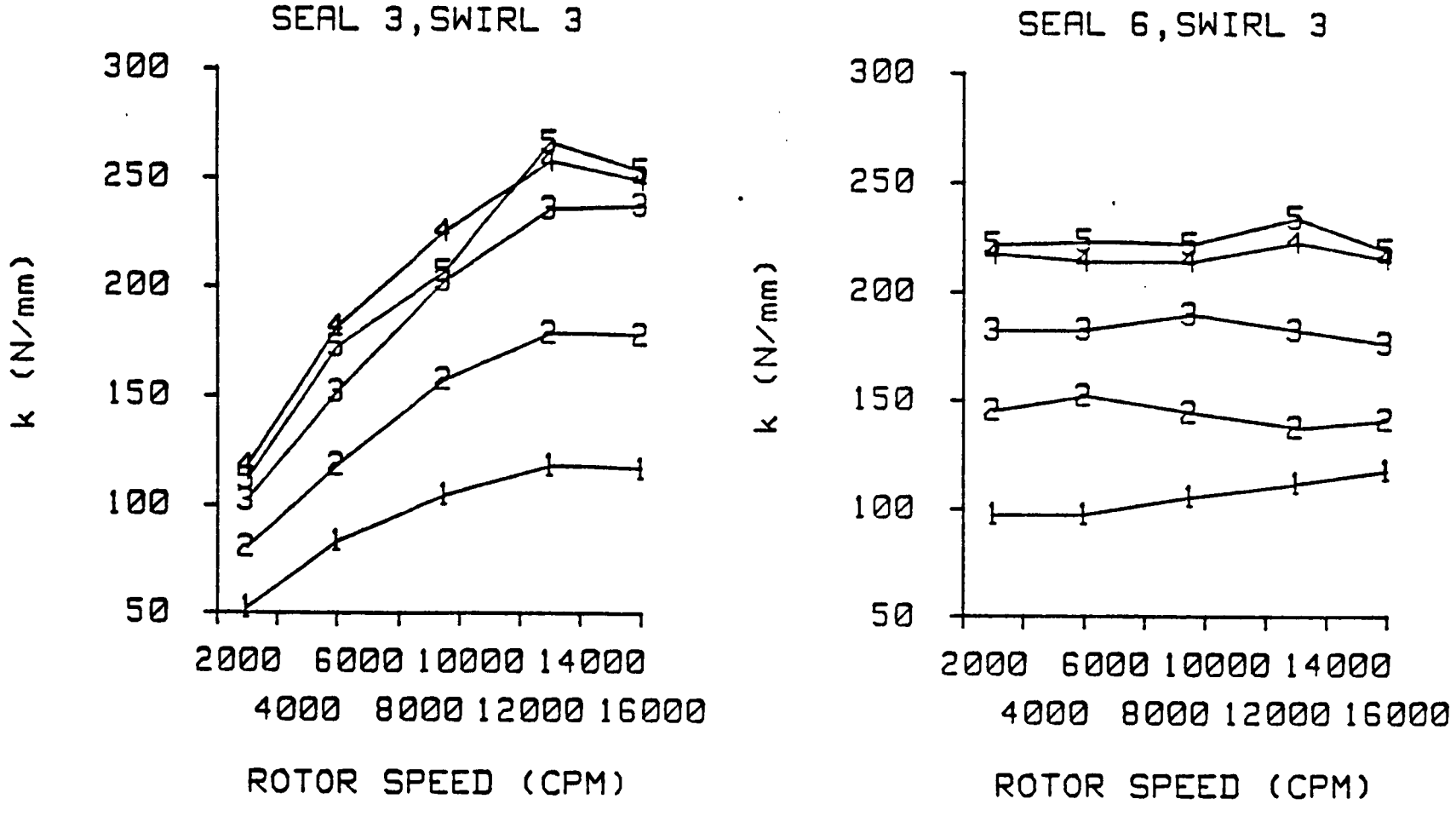

Figure 41. Cross-coupled stiffness versus rotor speed for seals 3 & 6 and inlet circumferential velocity 3. Inlet pressures 1–5 are plotted (see Table 2). Honeycomb stator (left), smooth stator (right).

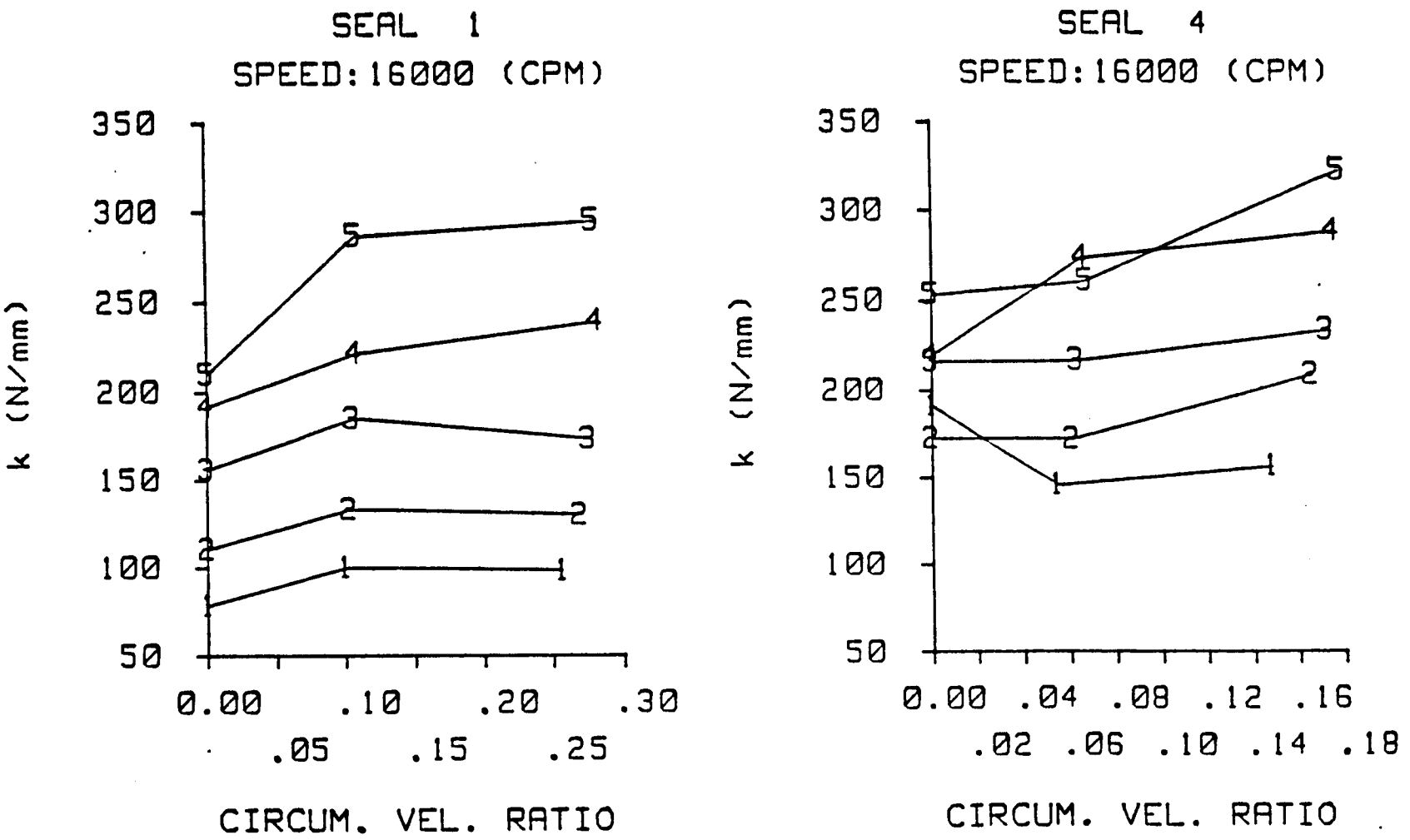

Figure 42. Cross-coupled stiffness versus inlet circumferential velocity ratio for seals 1 & 4 and rotor speed of 16000 cpm. Inlet pressures 1–5 are plotted (see Table 2). Honeycomb stator (left), smooth stator (right).

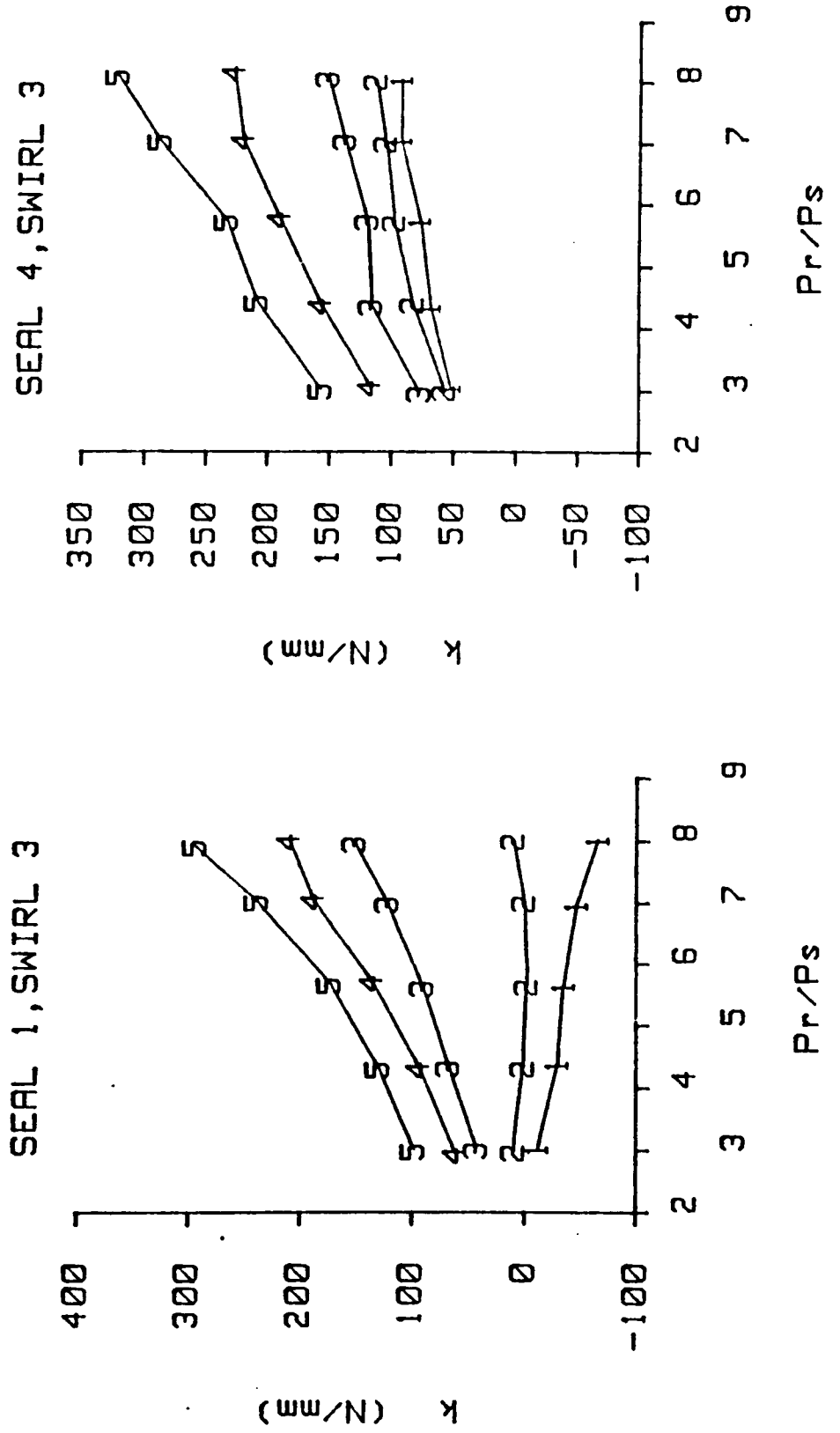

Figure 43. Cross-coupled stiffness versus inlet pressure ratio for seals 1 & 4 and inlet circumferential velocity 3. Rotor speeds 1-5 are plotted (see Table 2). Honeycomb stator (left), smooth stator (right).

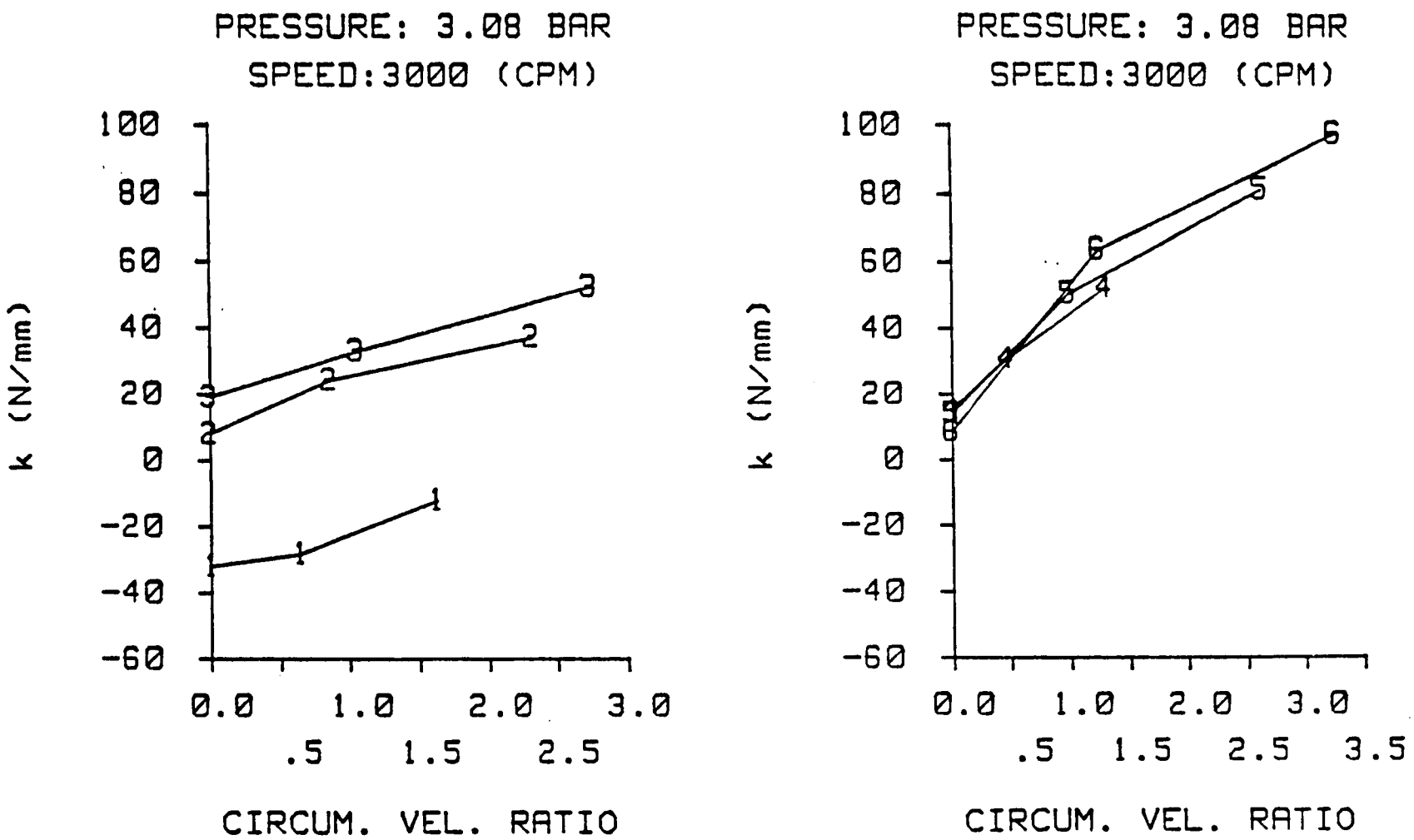

Figure 44. Cross-coupled stiffness versus inlet circumferential velocity ratio for inlet pressure of 3.08 bar and rotor speed of 3000 cpm. Three clearances are plotted (see Table 1). Honeycomb stator (left), smooth stator (right).

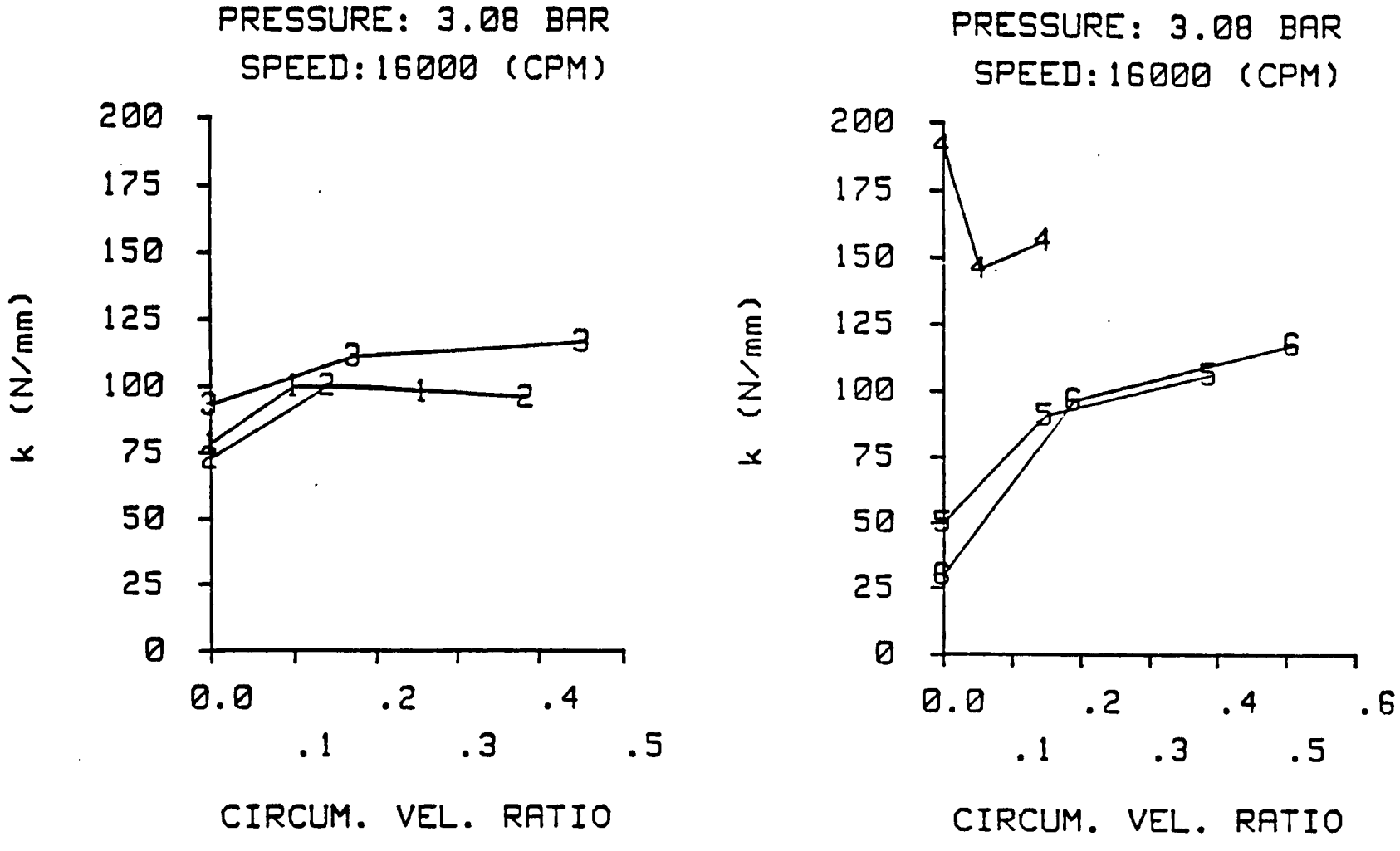

Figure 45. Cross-coupled stiffness versus inlet circumferential velocity ratio for inlet pressure of 3.08 bar and rotor speed of 16000 cpm. Three clearances are plotted (see Table 1). Honeycomb stator (left), smooth on right (see Table 1).

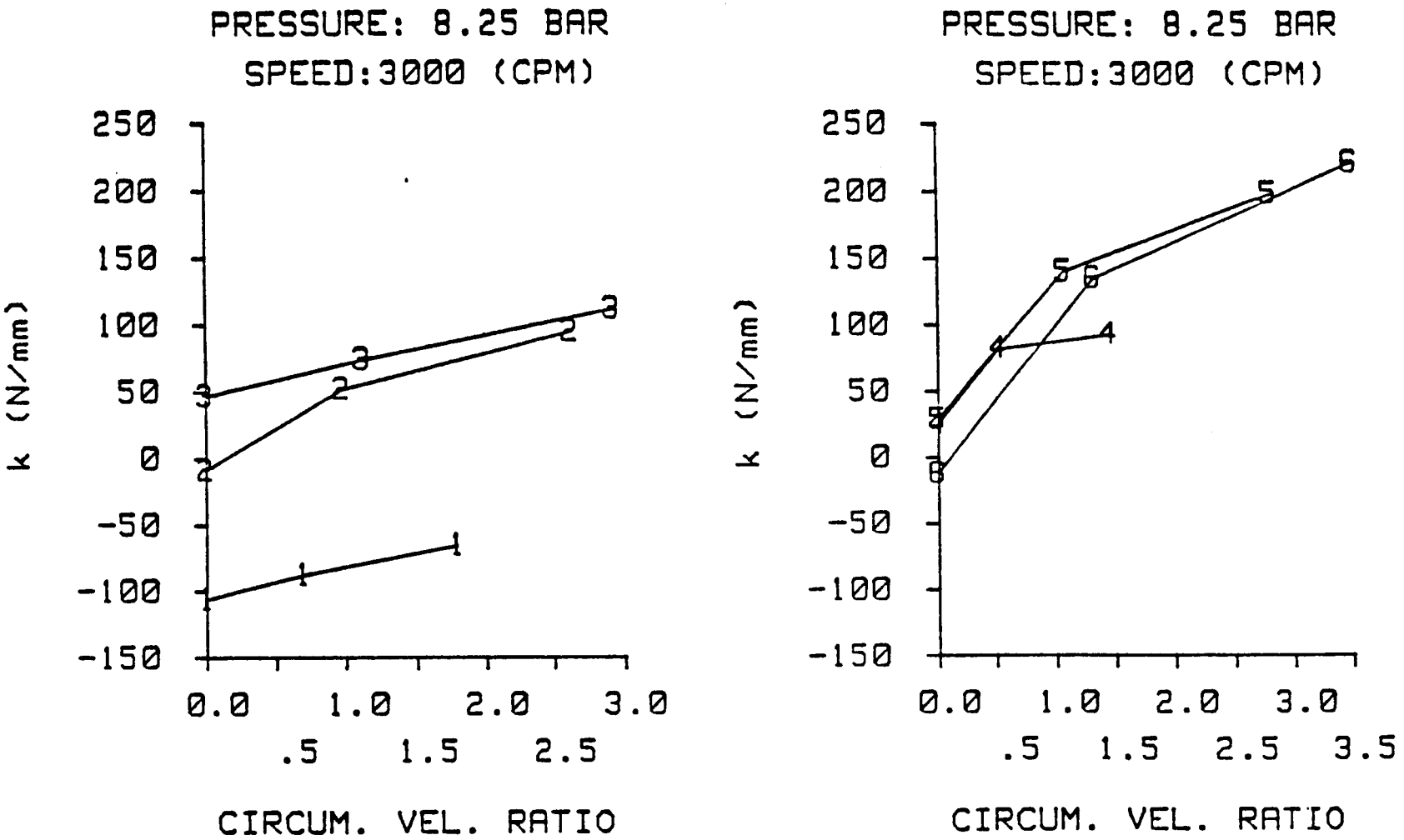

Figure 46. Cross-coupled stiffness versus inlet circumferential velocity ratio for inlet pressure of 8.25 bar and rotor speed of 3000 cpm. Three clearances are plotted (see Table 1). Honeycomb stator (left), smooth stator (right).

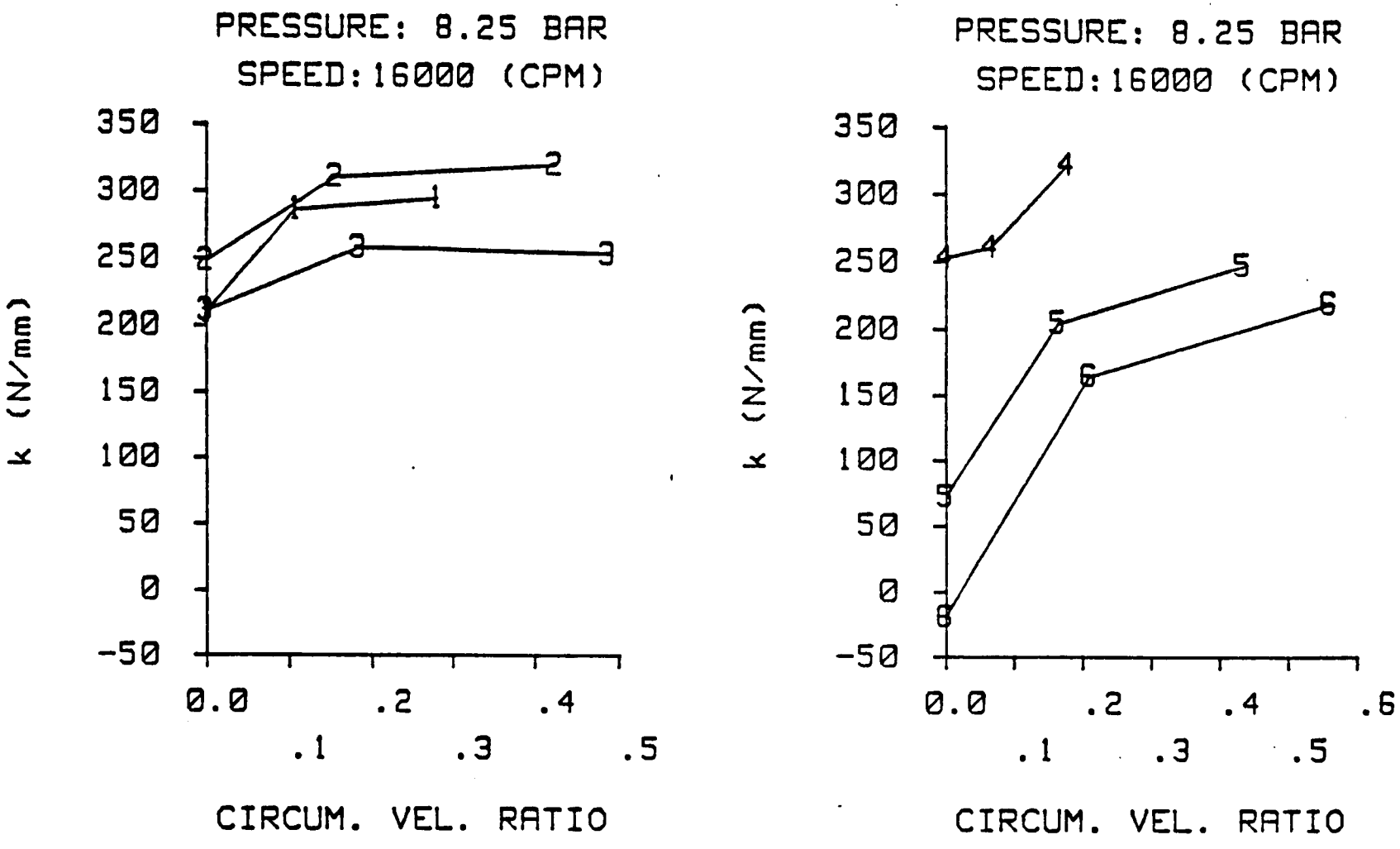

Figure 47. Cross-coupled stiffness versus inlet circumferential velocity ratio for inlet pressure of 8.25 bar and rotor speed of 16000 cpm. Three clearances are plotted (see Table 1). Honeycomb stator (left), smooth on right (see Table 1).

Figures 44–47 show how increasing seal clearance affects cross-coupled stiffness. In each figure, cross-coupled stiffness is plotted versus circumferential velocity ratio for three seals. Figure 44 shows the effect of seal clearance on cross-coupled stiffness for a pressure of 3.08 bar and a rotor speed of 3000 cpm. For the honeycomb stator seal, cross-coupled stiffness becomes more positive as seal clearance increases. Increasing seal clearance results in a small increase in the cross-coupled stiffness of the smooth stator seal. Figure 45 is for the same pressure as figure 44, but for a rotor speed of 16,000 cpm. At this rotor speed, clearance does not seem to affect the cross-coupled stiffness of the honeycomb stator seal. However, for the smooth stator seal, the smallest clearance has a cross-coupled stiffness that is much higher than the other two clearances. This effect was seen previously, in figures 39–41, where the smallest clearance smooth stator seal has much more rotor speed dependence than the other two smooth seals. Figures 46 and 47 correspond to figures 44 and 45 respectively, where the pressure has been increased to 8.25 bar. The trends observed at the lower pressure are repeated at the higher pressure.

DIRECT DAMPING

Direct damping is plotted versus rotor speed for various pressures in figure 48. Direct damping has essentially the same magnitude for either stator surface. However, damping for the honeycomb stator seal first increases and then decreases with increasing rotor speed, while damping in the smooth stator seal does not depend on rotor speed. Figure 49 is a plot of direct damping versus inlet circumferential velocity ratio for various pressures. Direct damping is insensitive to circumferential velocity ratio for either stator surface. Figure 50 shows direct

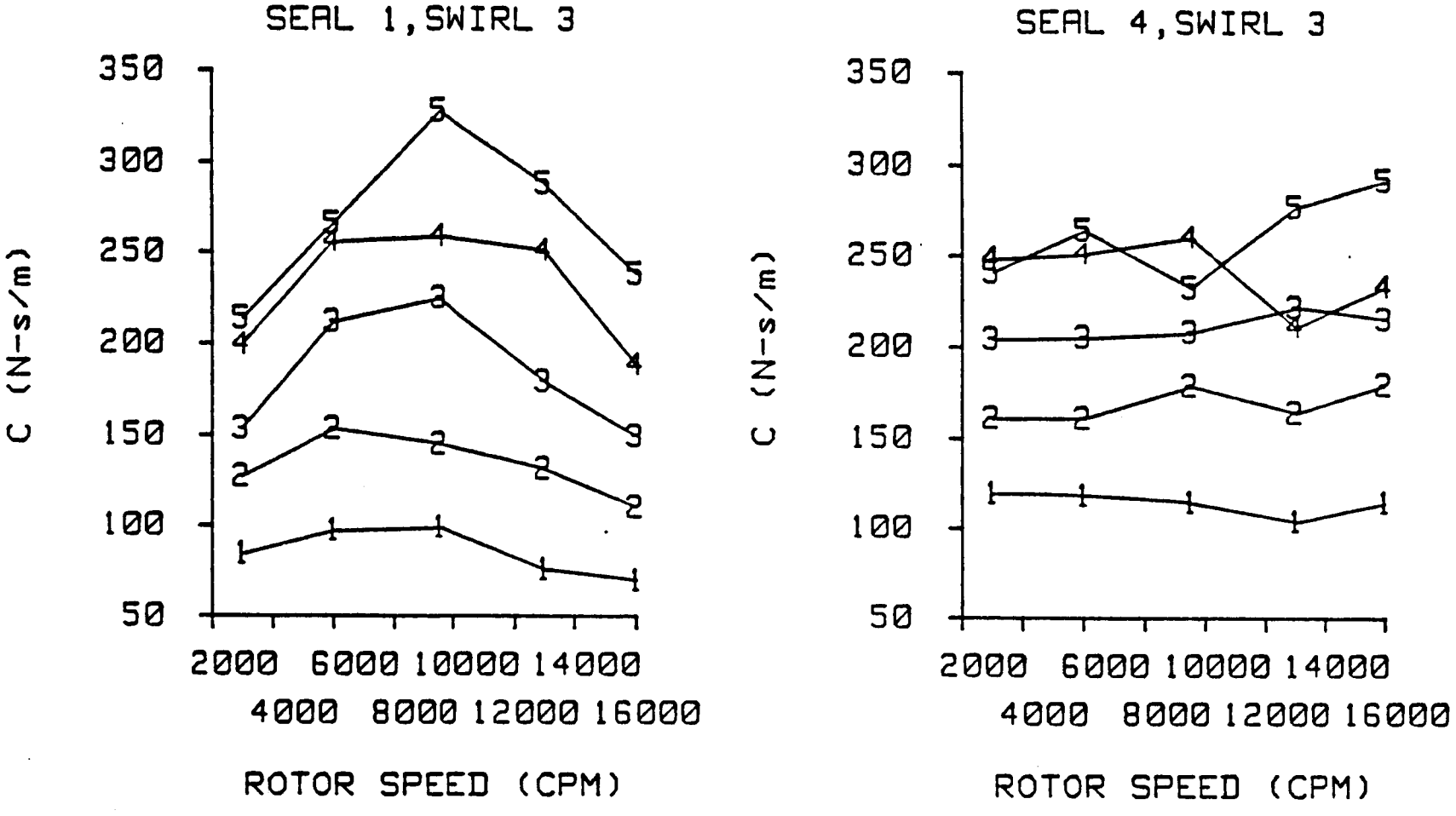

Figure 48. Direct damping versus rotor speed for seals 1 & 4 and inlet circumferential velocity 3. Inlet pressures 1–5 are plotted (see Table 2). Honeycomb stator (left), smooth stator (right).

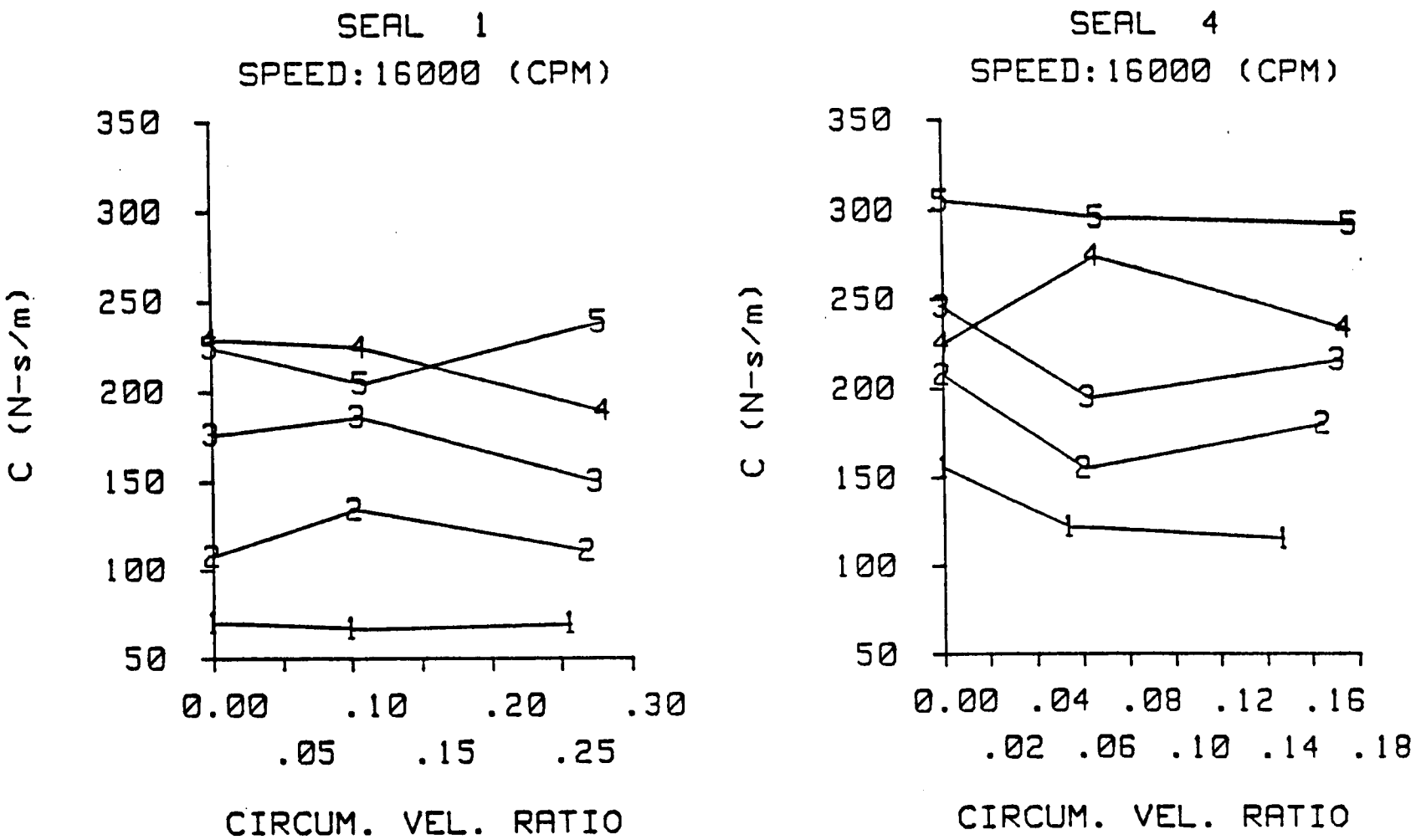

Figure 49. Direct damping versus inlet circumferential velocity ratio for seals 1 & 4 and rotor speed of 16000 cpm. Inlet pressures 1–5 are plotted (see Table 2). Honeycomb stator (left), smooth stator (right).

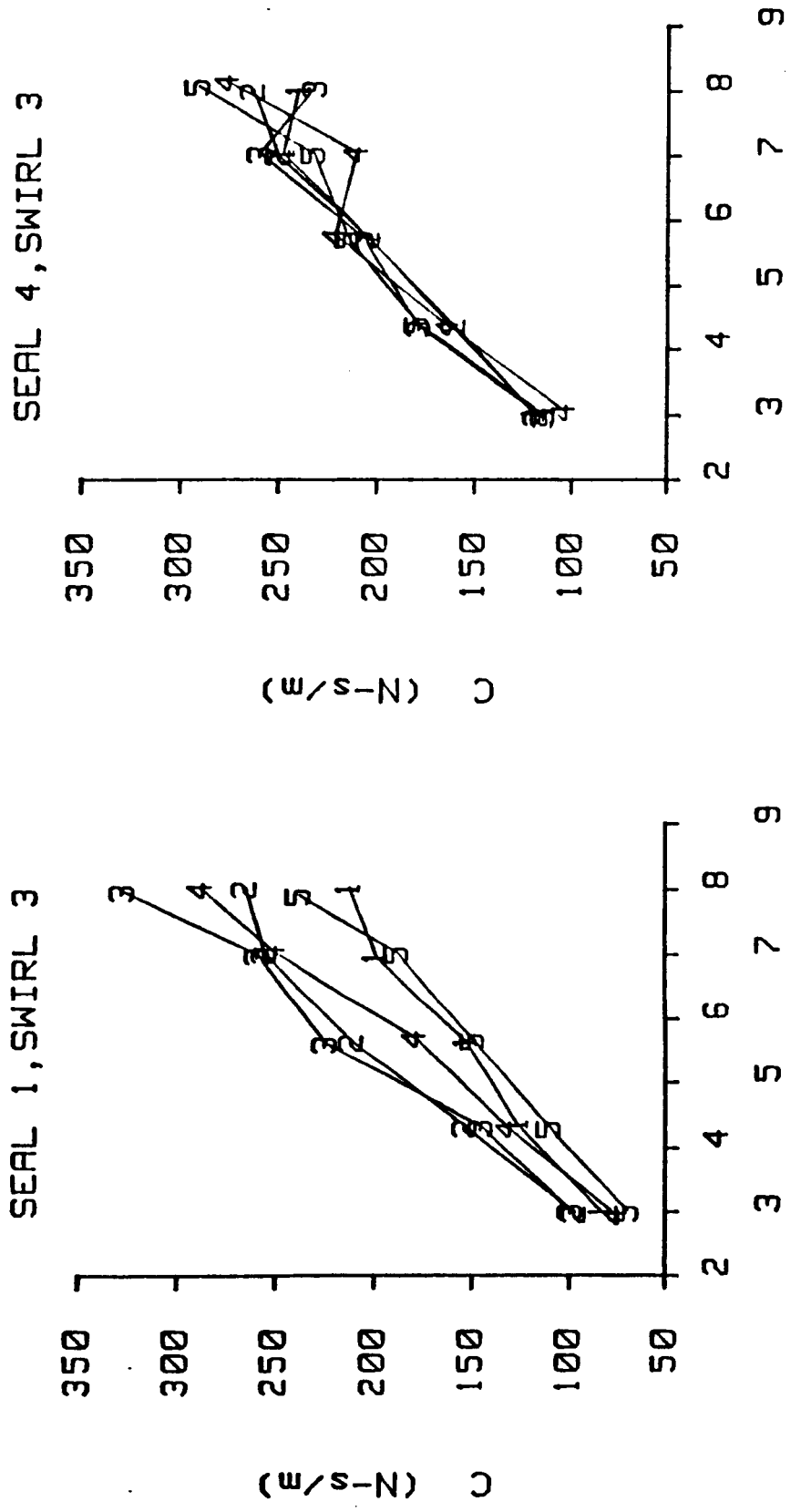

Figure 50. Direct damping versus inlet pressure ratio for seals 1 & 4 and inlet circumferential velocity 3. Rotor speeds 1–5 are plotted (see Table 2). Honeycomb stator (left), smooth stator (right).

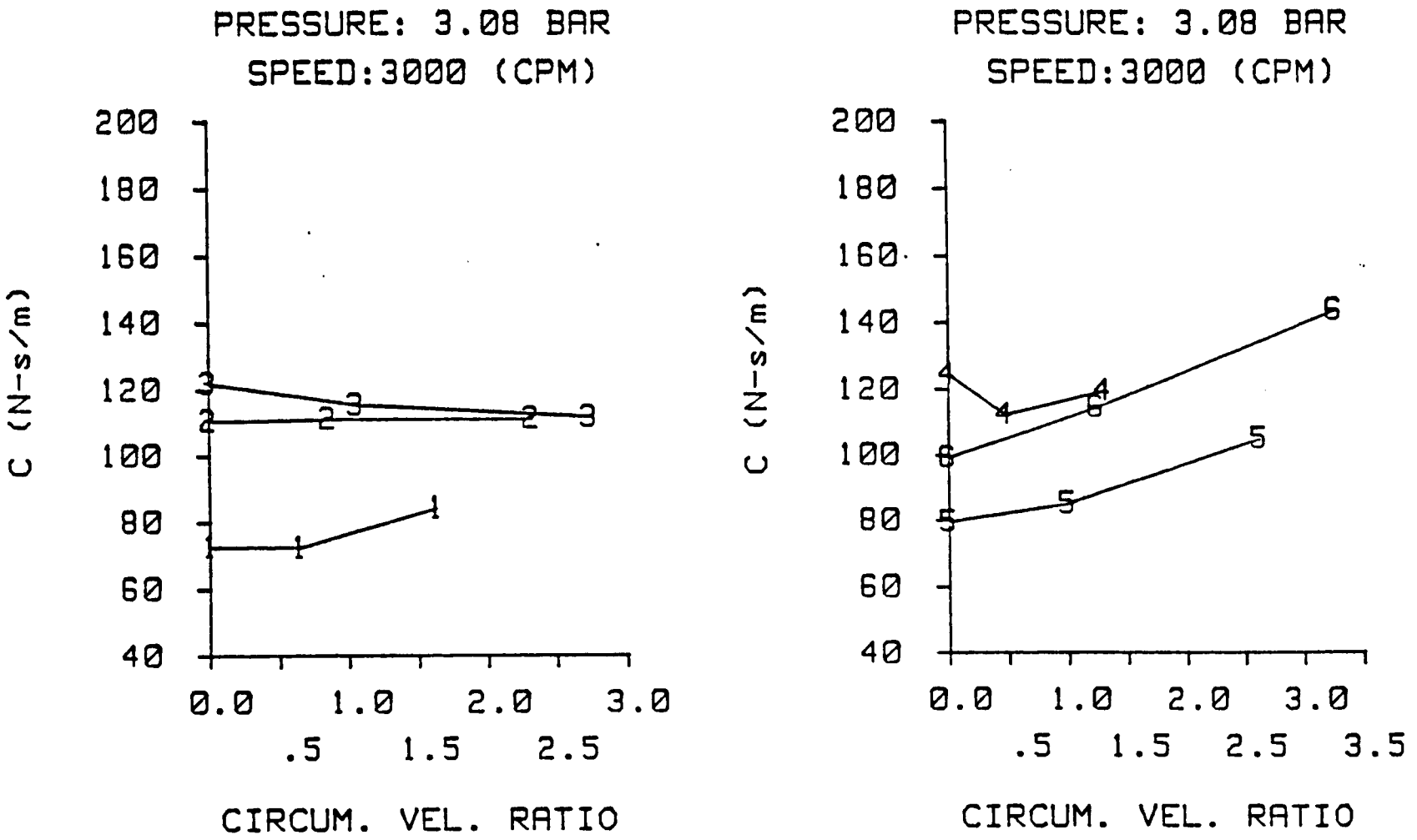

Figure 51. Direct damping versus inlet circumferential velocity ratio for inlet pressure of 3.08 bar and rotor speed of 3000 cpm. Three clearances are plotted (see Table 1). Honeycomb stator (left), smooth stator (right).

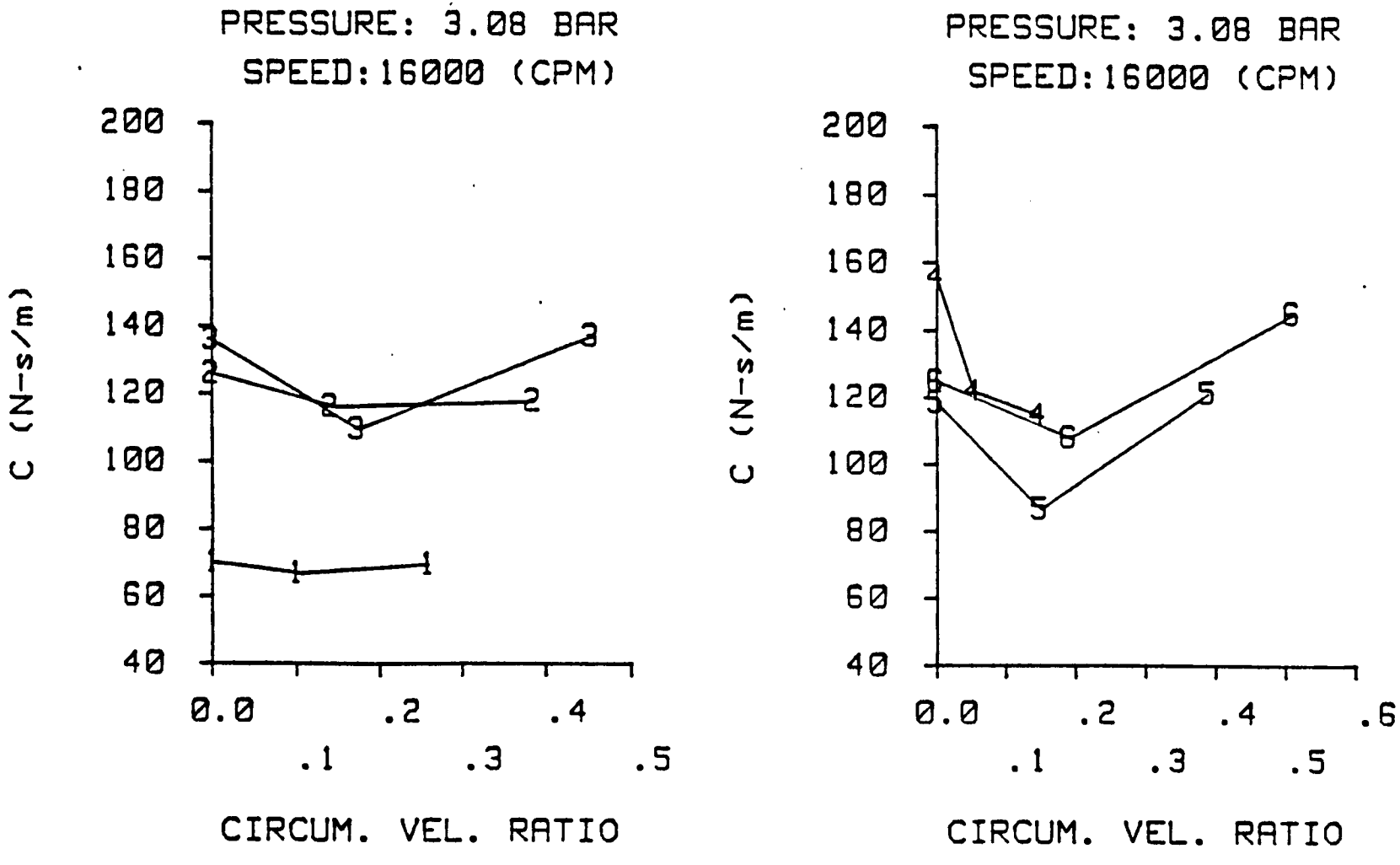

Figure 52. Direct damping versus inlet circumferential velocity ratio for inlet pressure of 3.08 bar and rotor speed of 16000 cpm. Three clearances are plotted (see Table 1). Honeycomb stator (left), smooth stator (right).

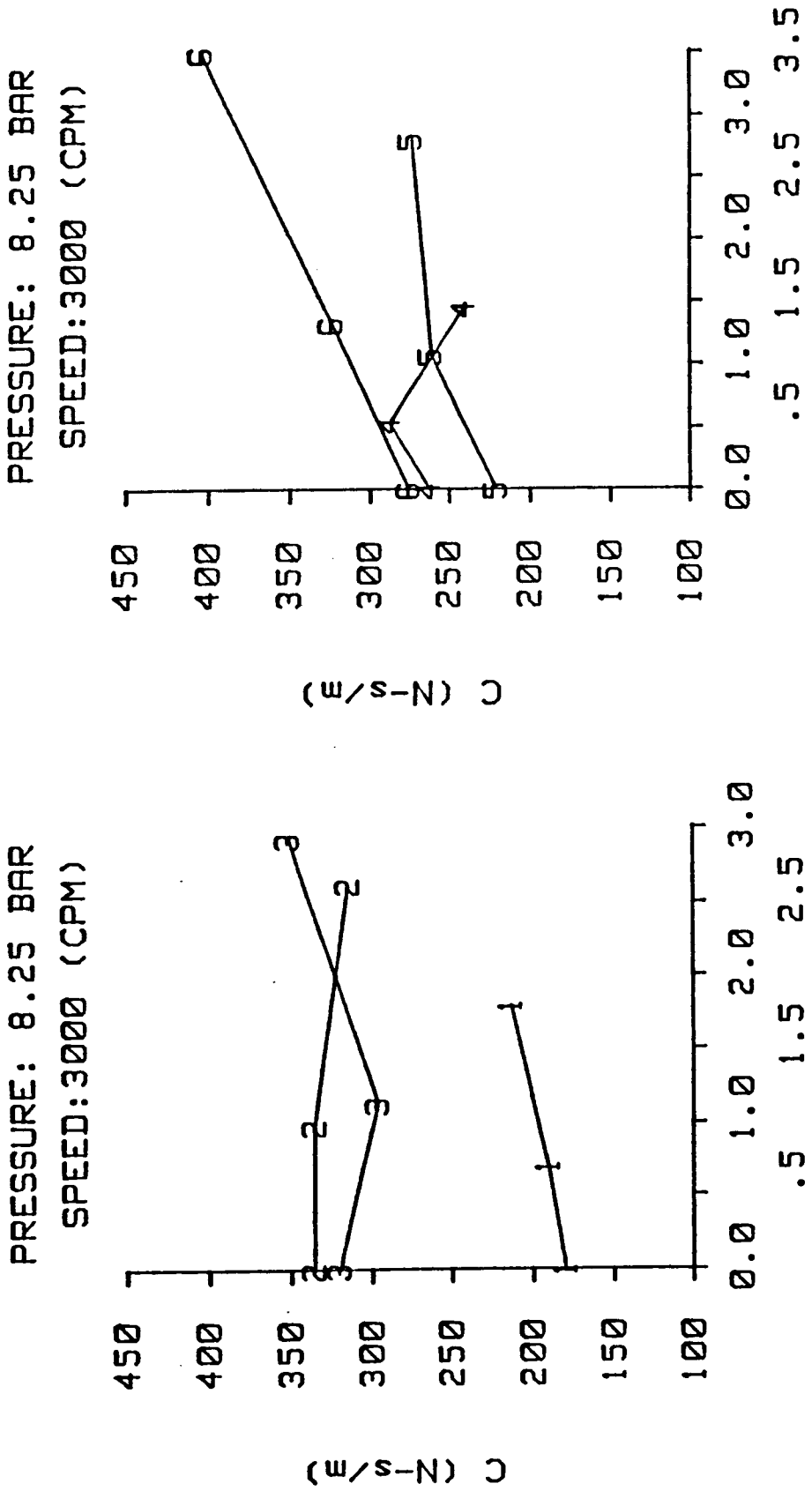

Figure 53. Direct damping versus inlet circumferential velocity ratio for inlet pressure of 8.25 bar and rotor speed of 3000 cpm. Three clearances are plotted (see Table 1). Honeycomb stator (left), smooth stator (right).

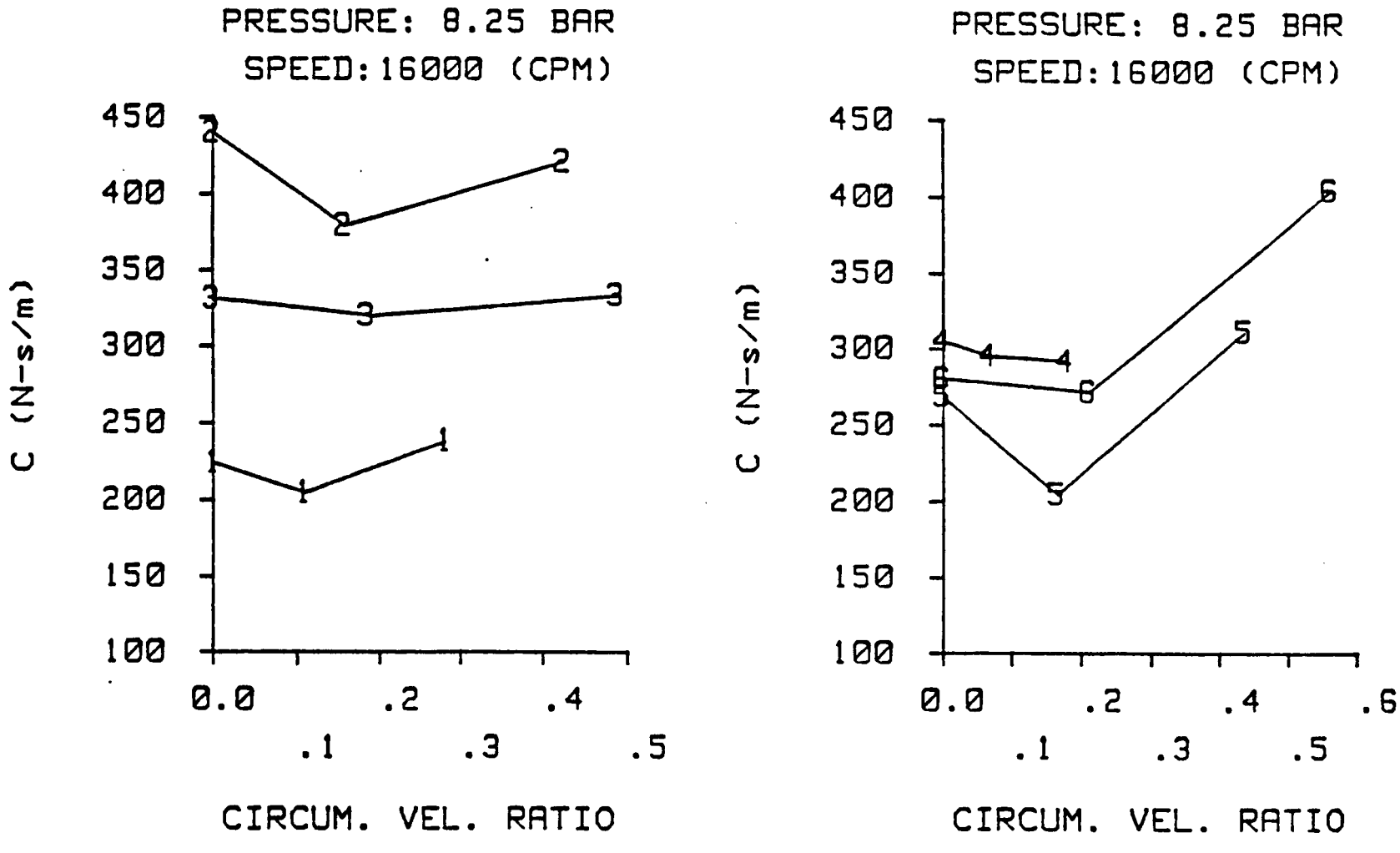

Figure 54. Direct damping versus inlet circumferential velocity ratio for inlet pressure of 8.25 bar and rotor speed of 16000 cpm. Three clearances are plotted (see Table 1). Honeycomb stator (left), smooth stator (right).

damping versus pressure ratio for various rotor speeds. As with the other rotordynamic coefficients, direct damping increases directly with pressure. Similar trends were obtained for seals 2,3,5, and 6. The data for these seals are given in the Appendix.

The effect of seal clearance on direct damping is shown in figures 51–54. Figure 51 shows the effect of seal clearance on direct damping at a pressure of 3.08 bar and a rotor speed of 3000 cpm. Damping increases somewhat from seal 1 (the smallest clearance seal) to seal 2. However, damping in seal 2 and seal 3 is roughly the same. In the smooth stator seal, there is no clear effect of clearance on damping. Figure 52 shows the same information as figure 51 except that the rotor speed has been increased to 16,000 cpm. The trends are the same as for figure 51. Thus, rotor speed does not play a part in the relationship between direct damping and clearance. Figures 53 and 54 show the same information as figures 51 and 52 except that the pressure has been increased to 8.25 bar. The influence of clearance on direct damping is the same as it was at the lower pressure.

WHIRL FREQUENCY RATIO

The effect of rotor speed on whirl frequency ratio is shown in figures 55 and 56. Inlet circumferential velocity is at its highest velocity with rotation for both plots.

Figure 55 is a plot of whirl frequency ratio versus rotor speed for a pressure of 3.08 bar. Whirl frequency ratio decreases with rotor speed for the two larger clearance seals for both stator surfaces. In the smallest clearance honeycomb stator seal, whirl frequency ratio increases with rotor speed. In the smallest

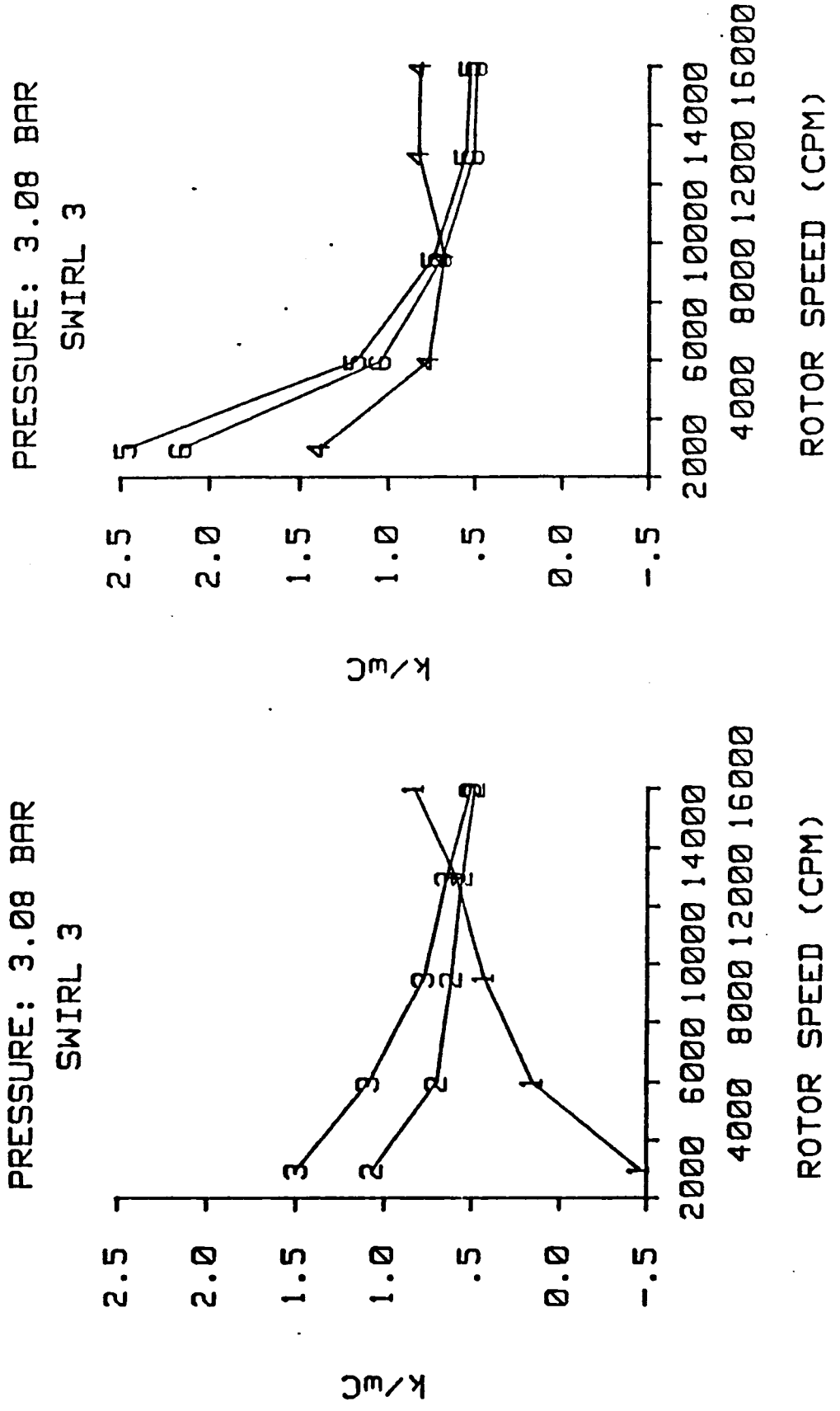

Figure 55. Whirl frequency ratio versus rotor speed for inlet pressure of 3.08 bar and inlet circumferential velocity 3. Three clearances are plotted (see Table 1). Honeycomb stator (left), smooth stator (right).

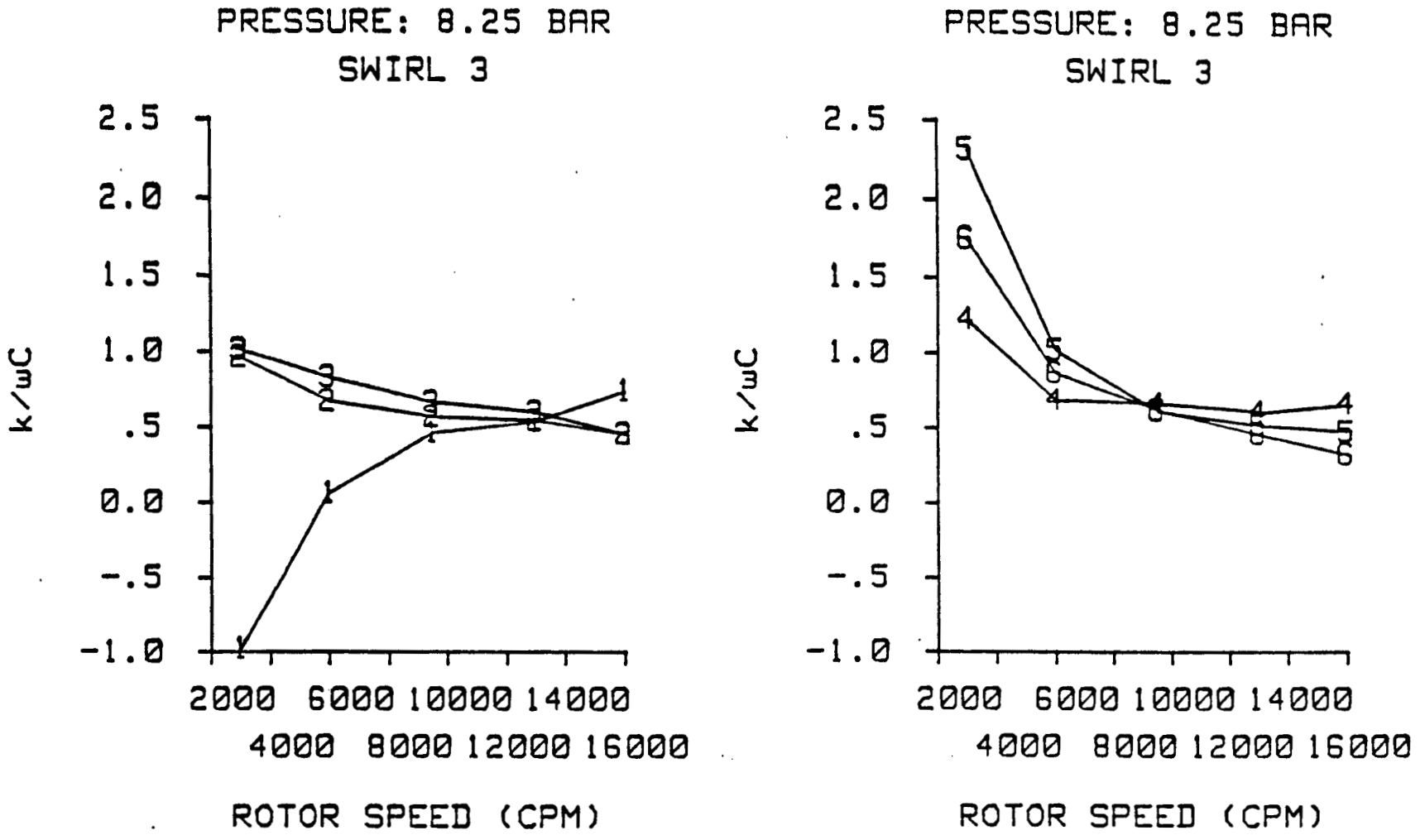

Figure 56. Whirl frequency ratio versus rotor speed for inlet pressure of 8.25 bar and inlet circumferential velocity 3. Three clearances are plotted (see Table 1). Honeycomb stator (left), smooth stator (right).

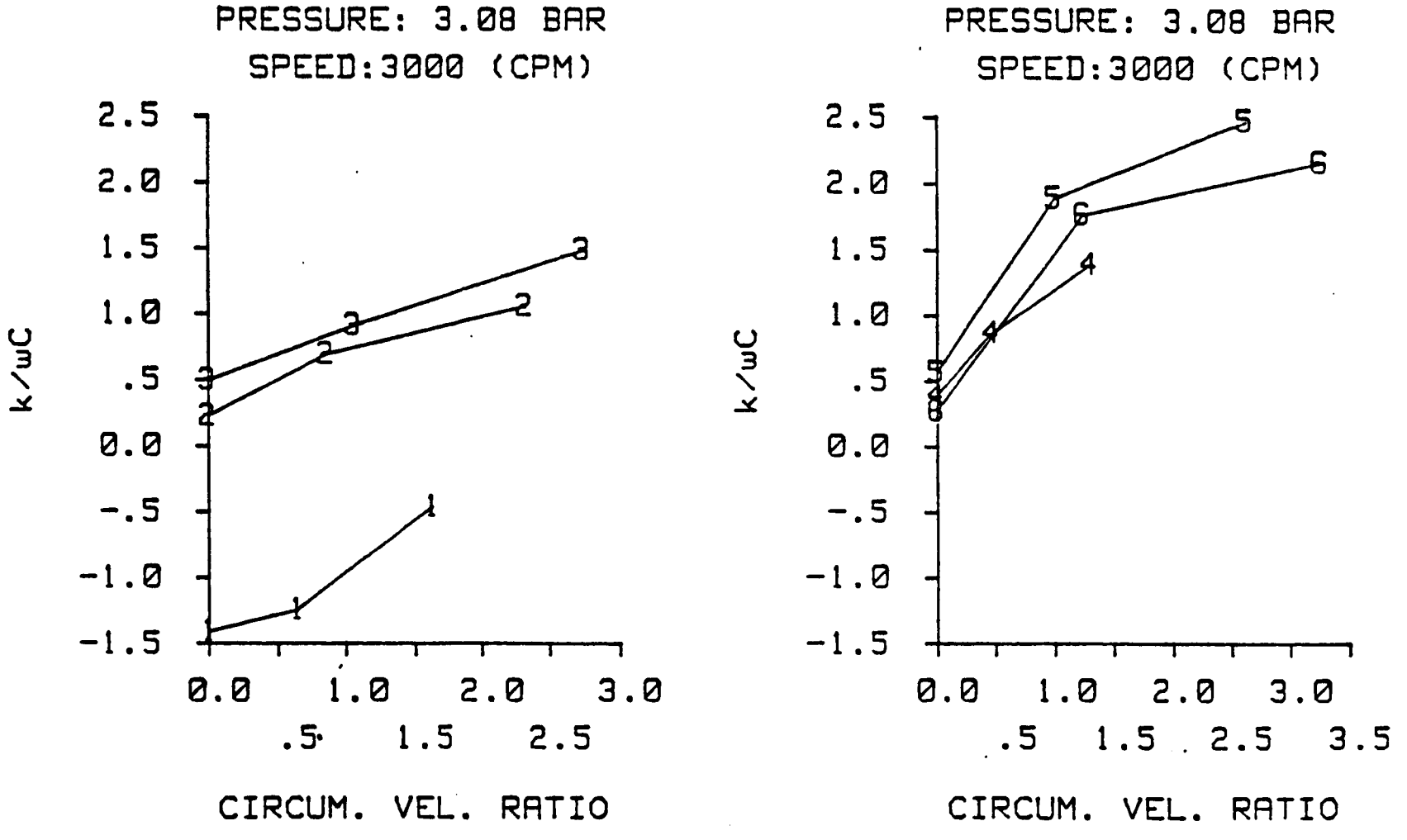

Figure 57. Whirl frequency ratio versus inlet circumferential velocity ratio for inlet pressure of 3.08 bar and rotor speed of 3000 cpm. Three clearances are plotted (see Table 1). Honeycomb stator (left), smooth stator (right).

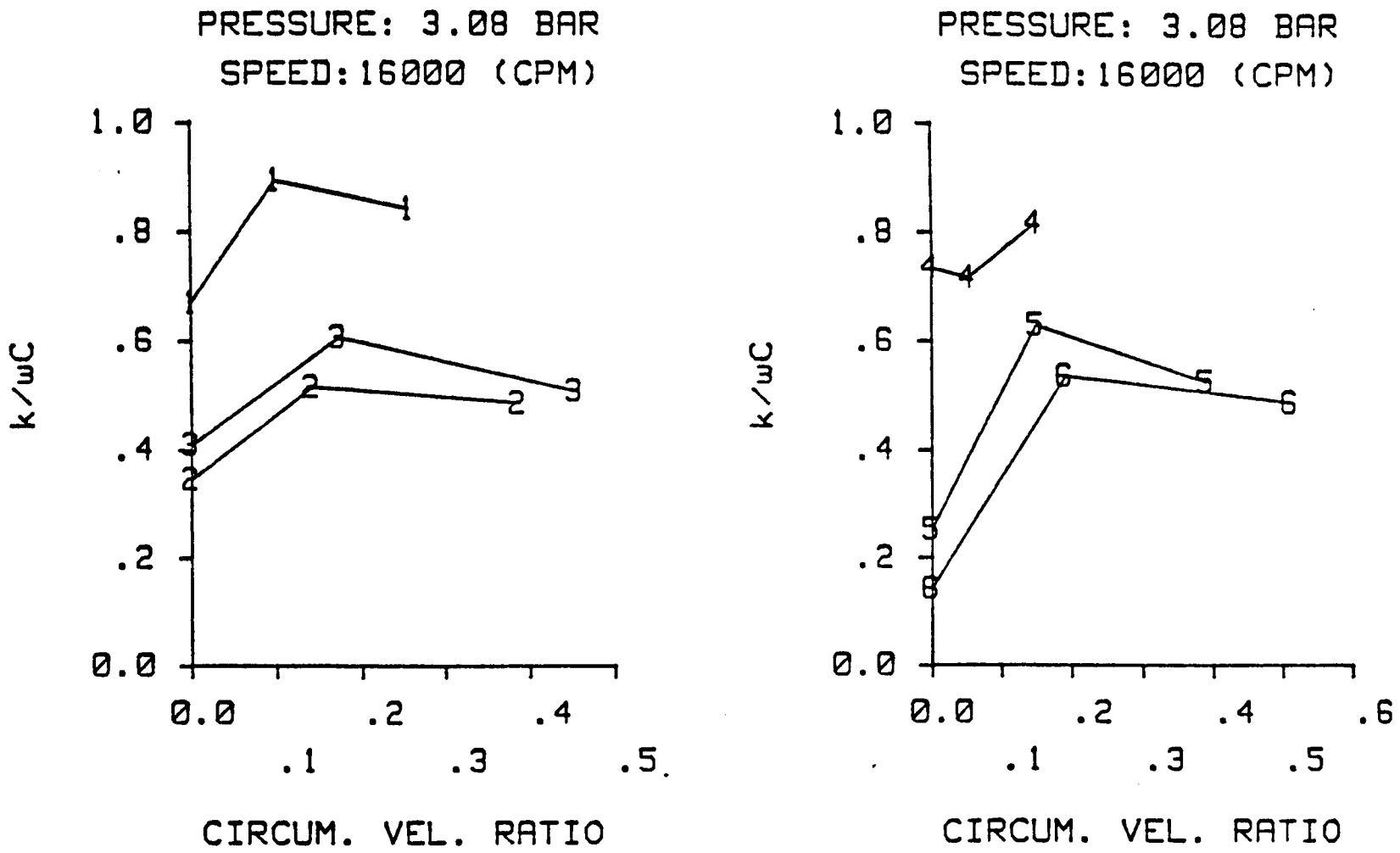

Figure 58. Whirl frequency ratio versus inlet circumferential velocity ratio for inlet pressure of 3.08 bar and rotor speed of 16000 cpm. Three clearances are plotted (see Table 1). Honeycomb stator (left), smooth stator (right).

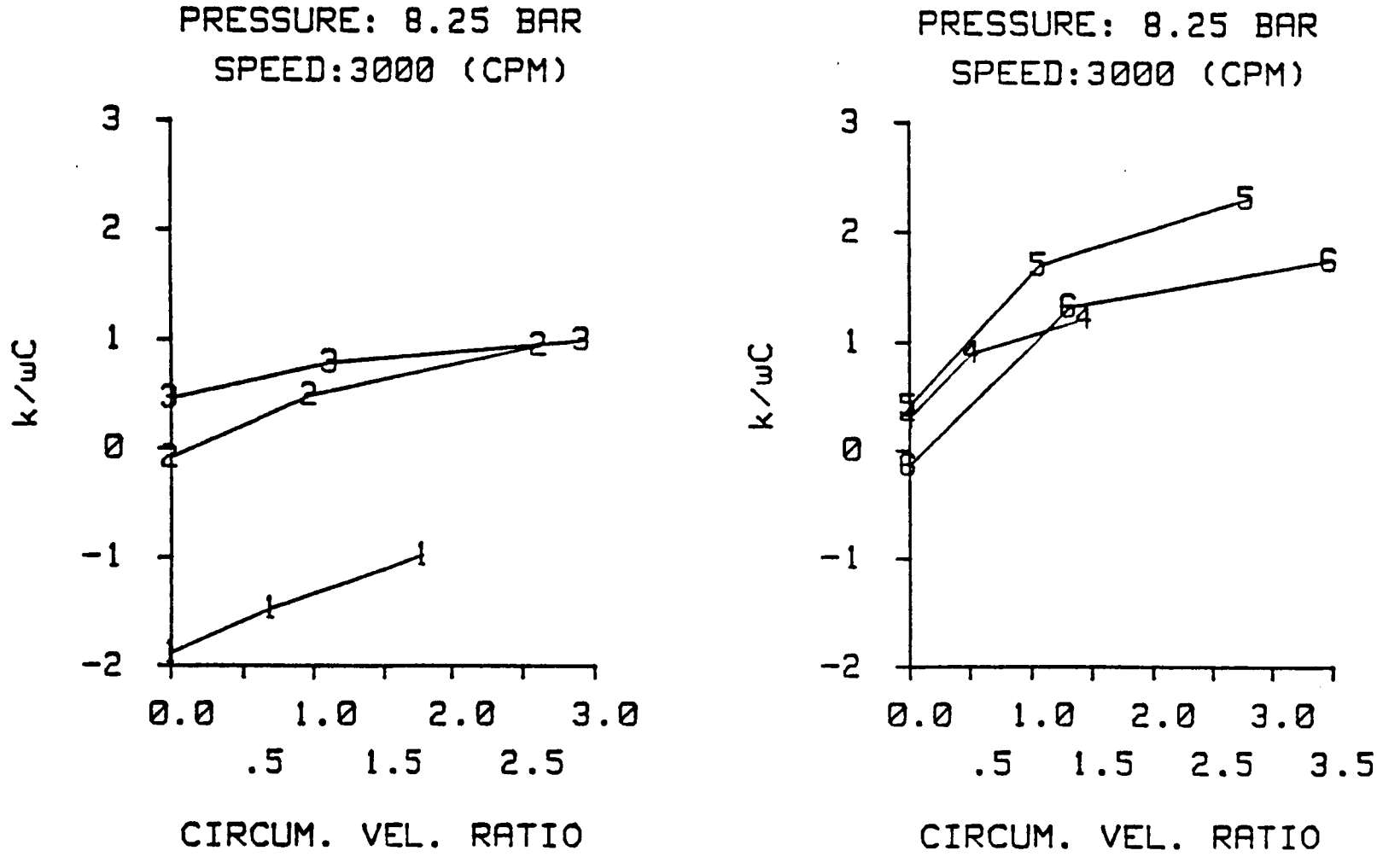

Figure 59. Whirl frequency ratio versus inlet circumferential velocity ratio for inlet pressure of 8.25 bar and rotor speed of 3000 cpm. Three clearances are plotted (see Table 1). Honeycomb stator (left), smooth stator (right).

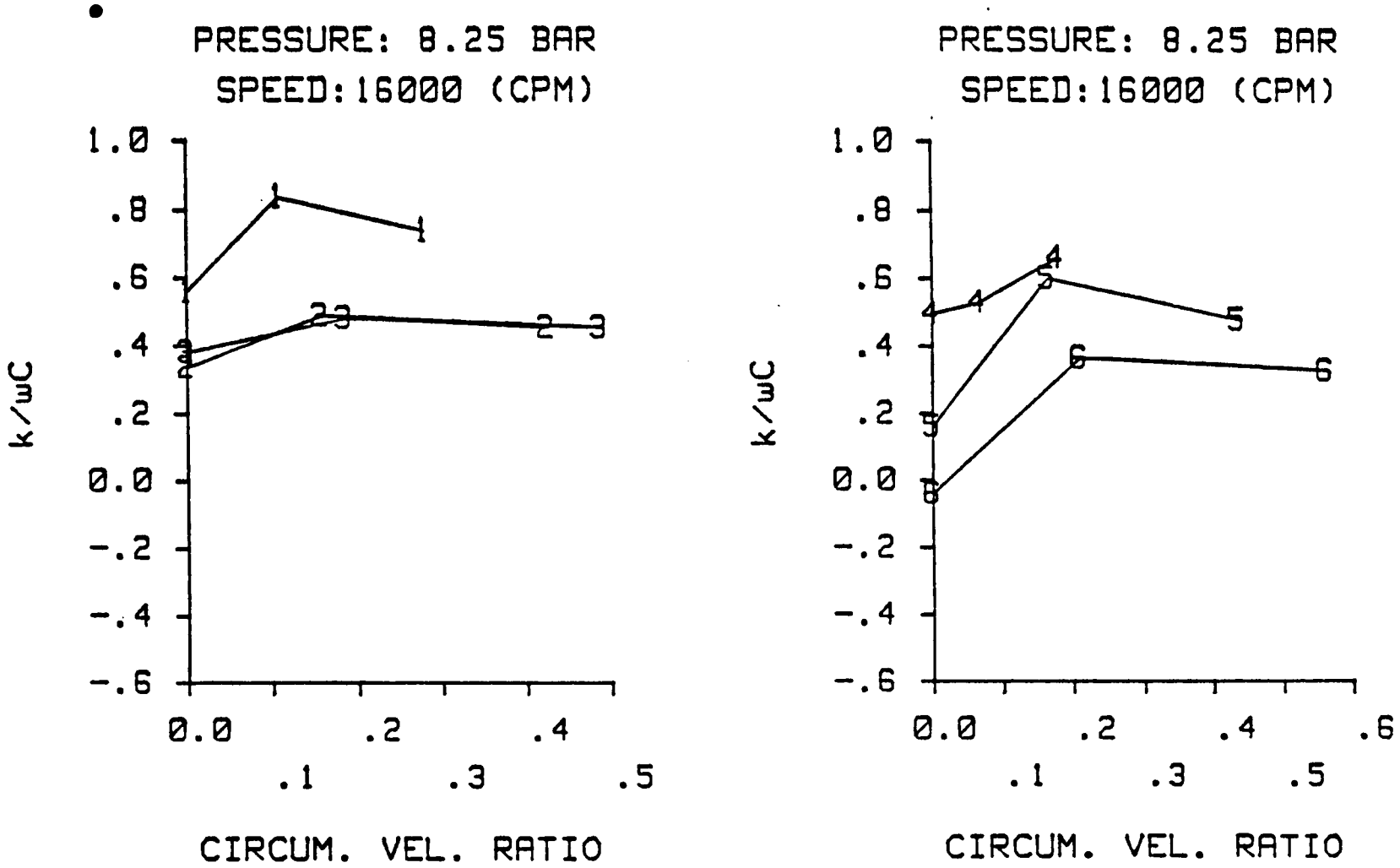

Figure 60. Whirl frequency ratio versus inlet circumferential velocity ratio for inlet pressure of 8.25 bar and rotor speed of 16000 cpm. Three clearances are plotted (see Table 1). Honeycomb stator (left), smooth stator (right).

clearance smooth stator seal, whirl frequency ratio initially decreases with rotor speed, but begins increasing at higher rotor speeds. Figure 56 is a plot of whirl frequency ratio versus rotor speed for a pressure of 8.25 bar. The trends observed in figure 55 are repeated here.

Figures 57–60 are plots of whirl frequency ratio versus circumferential velocity ratio for three clearances. Pressure and rotor speed are held constant on each plot. These plots show the effect of clearance on whirl frequency ratio. Figure 57 is for a pressure of 3.08 bar and a rotor speed of 3000 cpm. Whirl frequency ratio for the smallest clearance honeycomb stator seal is much lower than for the two larger clearances. There is not a clear trend for whirl frequency ratio versus clearance in the smooth stator seal. Figure 58 is similar to figure 57, except the rotor speed is 16,000 cpm. This time, the highest whirl frequency ratio is for the smallest clearance seal for both stator surfaces. Figures 59 and 60 show the same trends as figures 57 and 58 for a pressure of 8.25 bar.

These results indicate that the honeycomb stator seals are more stable at low rotor speeds. At the highest rotor speeds tested, the smallest clearance smooth seal is more stable than the smallest clearance honeycomb stator seal, and the stator surface does not affect stability at the larger clearances.

C-2

CHAPTER VI

COMPARISON OF RESULTS TO THEORETICAL MODEL

In this chapter, experimental results for the labyrinth-rotor/honeycomb-stator and the labyrinth-rotor/smooth-stator configurations are compared to the predictions of Scharrer's [13] theoretical model. The model input is described below. In the figures that follow, the honeycomb stator results are presented on the left and the smooth stator results are presented on the right.

MODEL INPUT

The required input for the model and the values used are shown in table 4. The values marked with an asterisk are approximate; the true values used are those recorded for each particular test. Kinematic viscosity was calculated from recorded values using Sutherland's formula from Schlichting [23]. Seal clearance was corrected for rotor speed using the values from table 3.

DIRECT STIFFNESS

Experimental values of direct stiffness are compared to the predictions of Scharrer's model in figures 61–66. Figure 61 is a plot of direct stiffness versus rotor speed. The model predicts an increase in the magnitude of direct stiffness with rotor speed that is not present in the experimental data. Also, the model predicts that direct stiffness is positive at low rotor speeds, whereas the experimental data show that it is negative. Figure 62 is a plot of direct stiffness versus circumferential velocity ratio. The model predicts that direct stiffness is

Table 4. Input parameters for theoretical model.

	Honeycomb Stator	Smooth Stator
Reservoir Pressure (bar)	Table 2*	Table 2*
Sump Pressure (bar)	1.0*	1.0*
Reservoir Temp. (K)	300.0*	300.0*
Clearance (mm)	Table 1,3*	Table 1,3*
Rotor Radius (mm)	75.77	75.77
Tooth Pitch (mm)	3.175	3.175
Tooth Height (mm)	3.175	3.175
Tooth Tip Width (mm)	0.150	0.150
Friction Coefficients		
Rotor – mr	-0.2417	-0.2417
– nr	0.0942	0.0942
Stator – ms	-0.1083	-0.2417
– ns	0.2820	0.0942
Specific Heat Ratio	1.40	1.40
Kinematic Viscosity (m^2/s)	2.3E-6*	2.3E-6*
Inlet Swirl Ratio	Table 2*	Table 2*
Rotor Speed (cpm)	Table 2*	Table 2*
Compressibility	1.0	1.0
Gas Constant (J/kg-K)	287.1	287.1
Number of Teeth	16	16

* Value is approximate (see text).

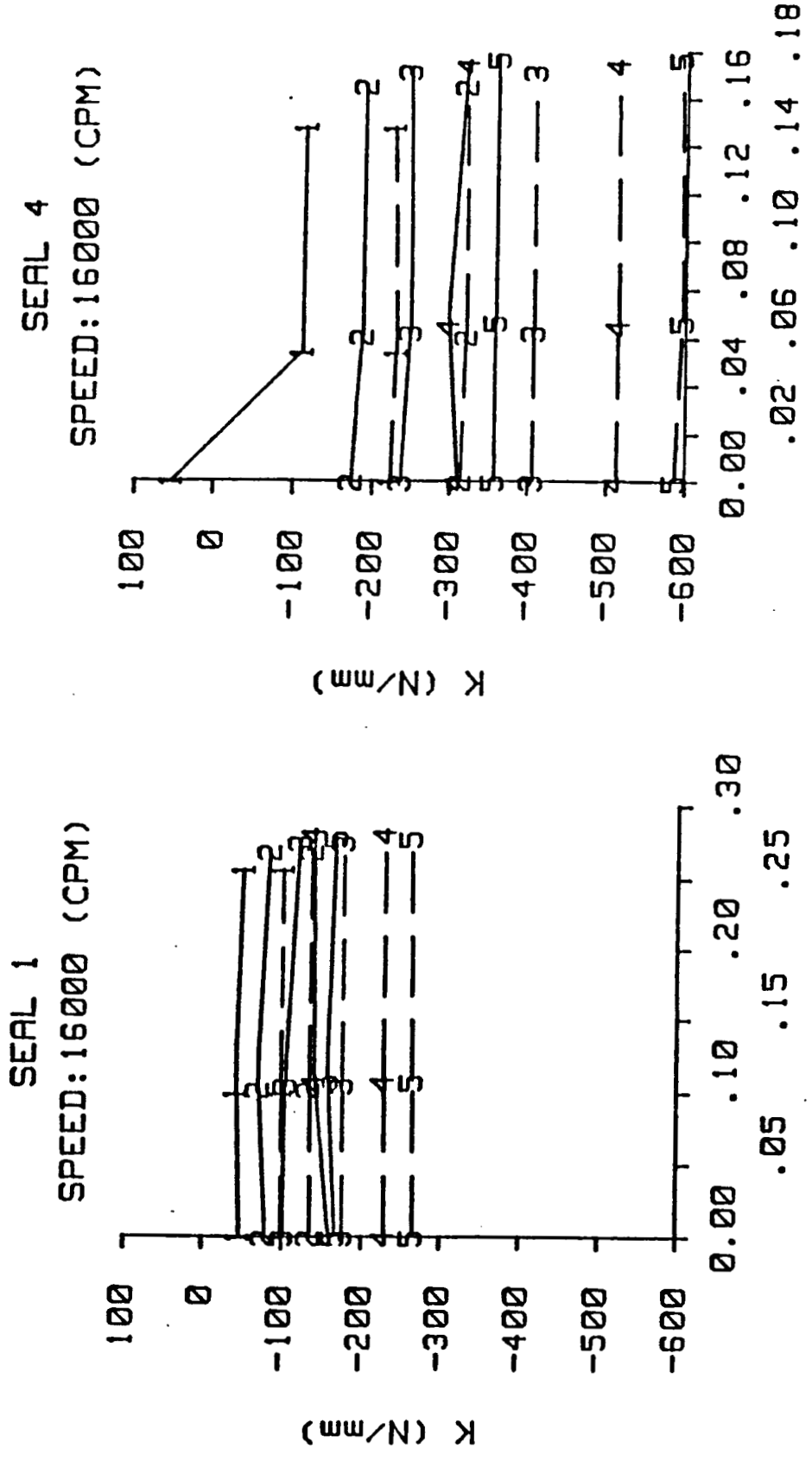

Figure 62. A comparison of experimental and theoretical direct stiffness versus inlet circumferential velocity ratio for seals 1 & 4 and rotor speed of 16000 cpm. Inlet pressures 1-5 are plotted (see Table 2). Honeycomb stator (left), smooth stator (right).

PRECEDING PAGE BLANK NOT FILMED

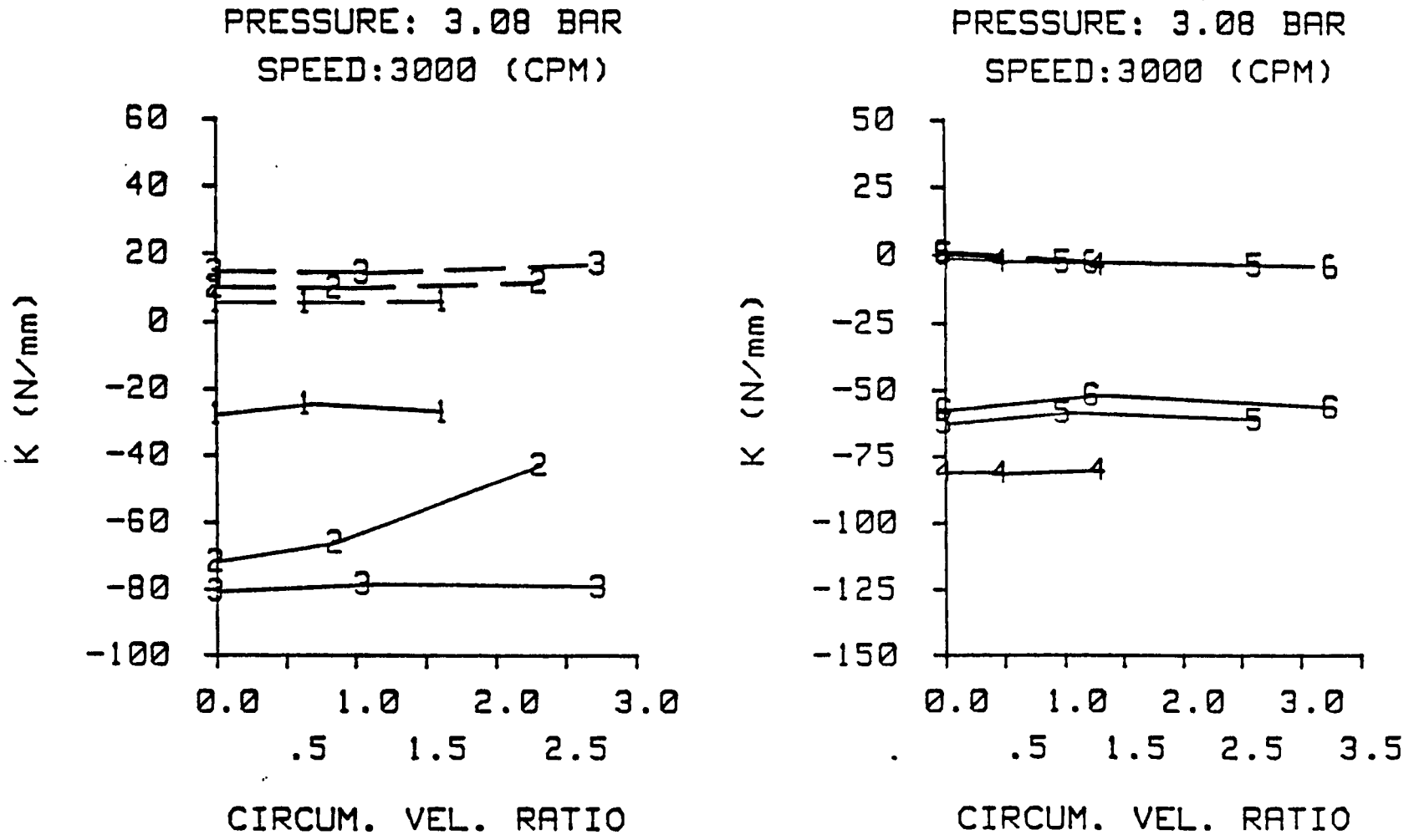

Figure 63. A comparison of experimental and theoretical direct stiffness versus inlet circumferential velocity ratio for inlet pressure of 3.08 bar and rotor speed of 3000 cpm. Three clearances are plotted (see Table 1). Honeycomb stator (left), smooth stator (right).

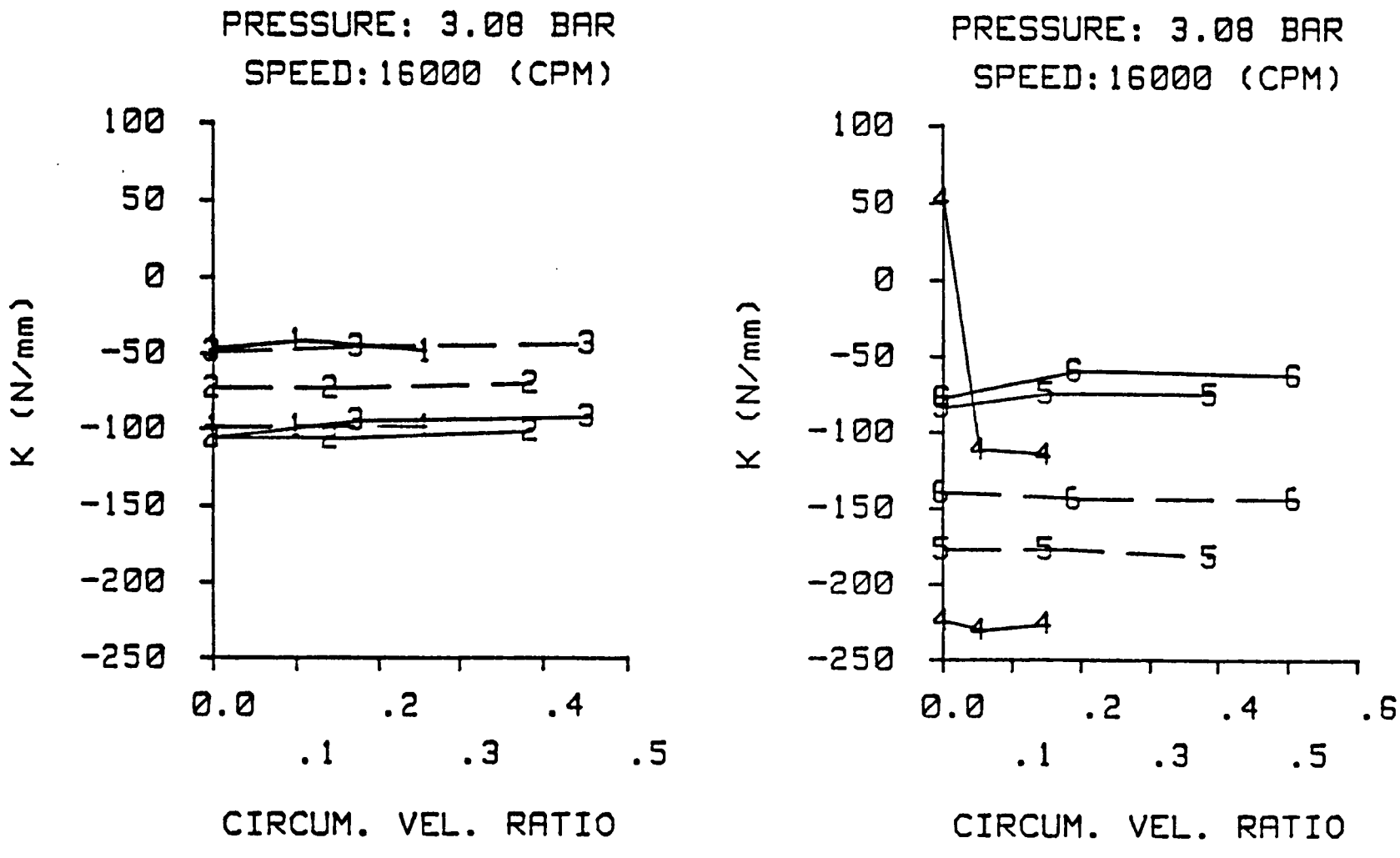

Figure 64. A comparison of experimental and theoretical direct stiffness versus inlet circumferential velocity ratio for inlet pressure of 3.08 bar and rotor speed of 16000 cpm. Three clearances are plotted (see Table 1). Honeycomb stator (left), smooth stator (right).

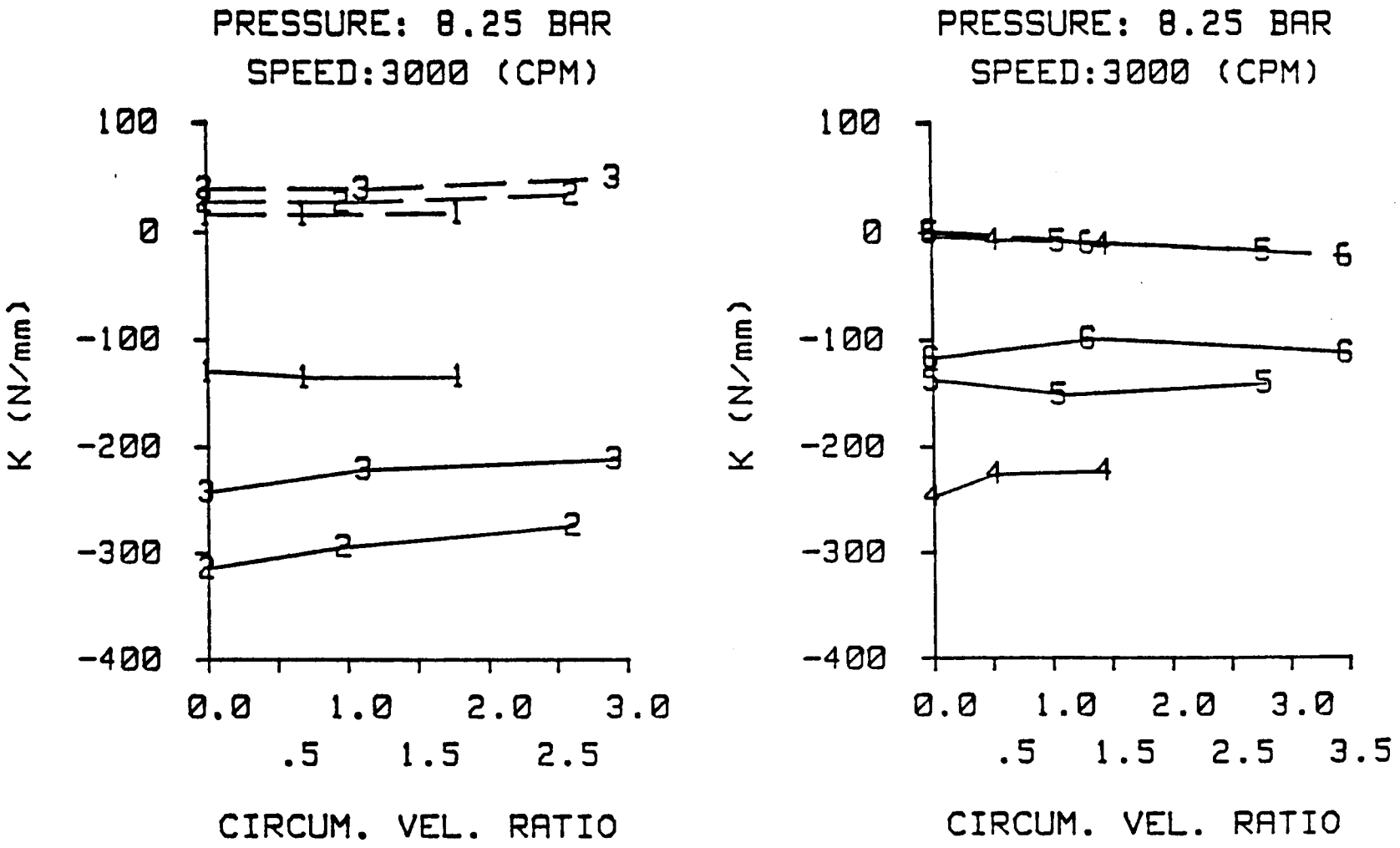

Figure 65. A comparison of experimental and theoretical direct stiffness versus inlet circumferential velocity ratio for inlet pressure of 8.25 bar and rotor speed of 3000 cpm. Three clearances are plotted (see Table 1). Honeycomb stator (left), smooth stator (right).

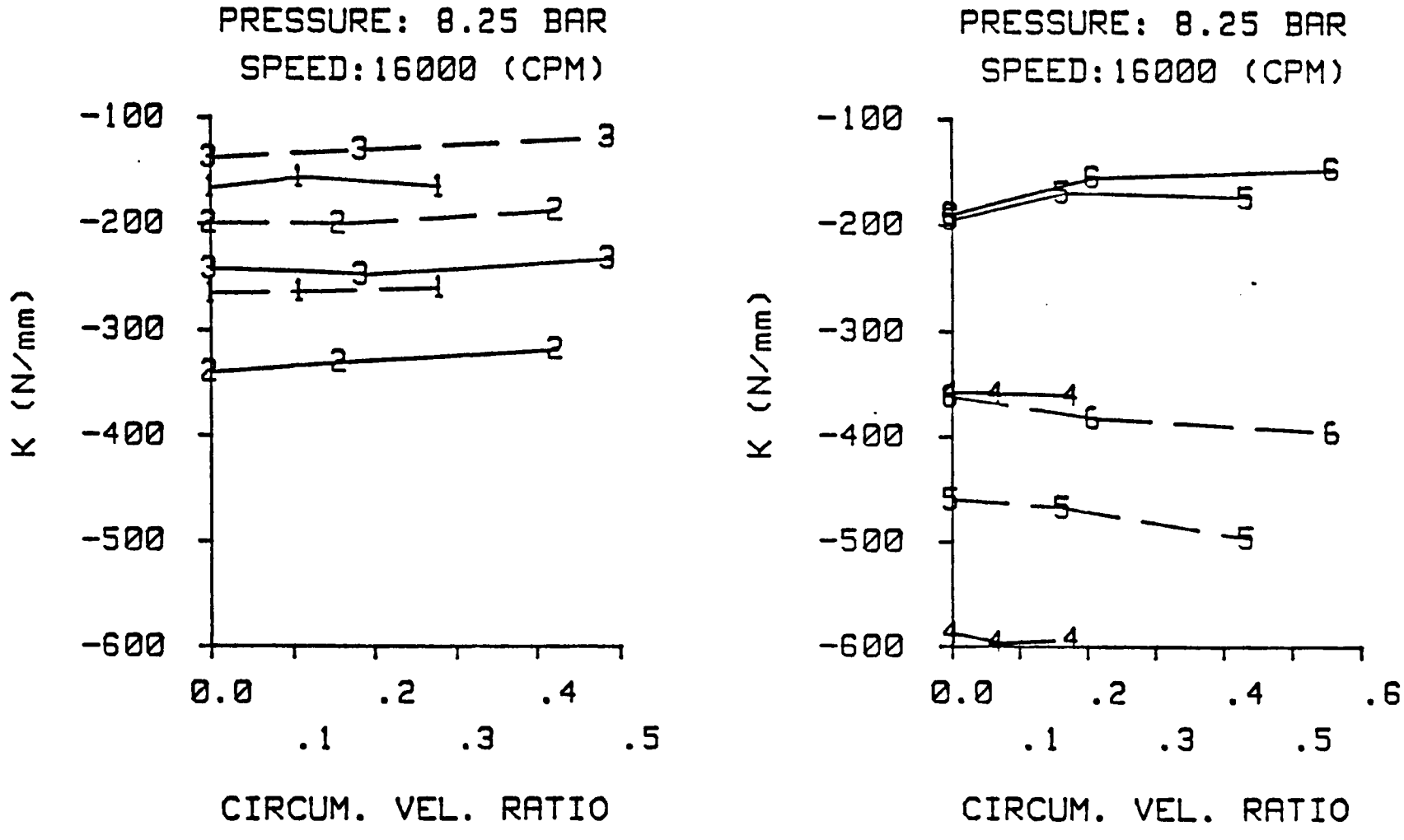

Figure 66. A comparison of experimental and theoretical direct stiffness versus inlet circumferential velocity ratio for inlet pressure of 8.25 bar and rotor speed of 16000 cpm. Three clearances are plotted (see Table 1). Honeycomb stator (left), smooth stator (right).

not affected by changes in the circumferential velocity ratio. This agrees with the experimental data.

Figures 63–66 show the effect of clearance on direct stiffness. The model predicts that direct stiffness becomes more positive as clearance increases. The experimental data for the honeycomb stator seal show that the stiffness initially becomes more negative as clearance increases and as the clearance gets large the stiffness begins to become more positive. The trend predicted by the model is correct for the smooth stator seal.

CROSS-COUPLED STIFFNESS

Experimental values for cross-coupled stiffness are compared to Scharrer's model in figures 67–73. Figure 67 is a plot of cross-coupled stiffness versus rotor speed for various pressures for the smallest clearance seal. The theory predicts the rise in cross-coupled stiffness with rotor speed for the honeycomb stator seal. For the smooth stator seal, the theory predicts an initial decrease in cross-coupled stiffness with rotor speed, but an increase beyond 9500 cpm. The test data indicates that cross-coupled stiffness rises with increasing rotor speed regardless of the rotor speed. Figure 68 is a plot of cross-coupled stiffness versus rotor speed for seals 3 and 6. The theory predicts that cross-coupled stiffness rises with rotor speed for the honeycomb stator seal. This result agrees with the test data. For the smooth stator seal, the theory predicts a speed dependence that is not present in the test data. In general, the model slightly underpredicts the speed dependence of the honeycomb stator seals and overpredicts the speed dependence of the smooth stator seals. However, the model consistently predicts the magnitude of cross-coupled stiffness within a factor of 2.

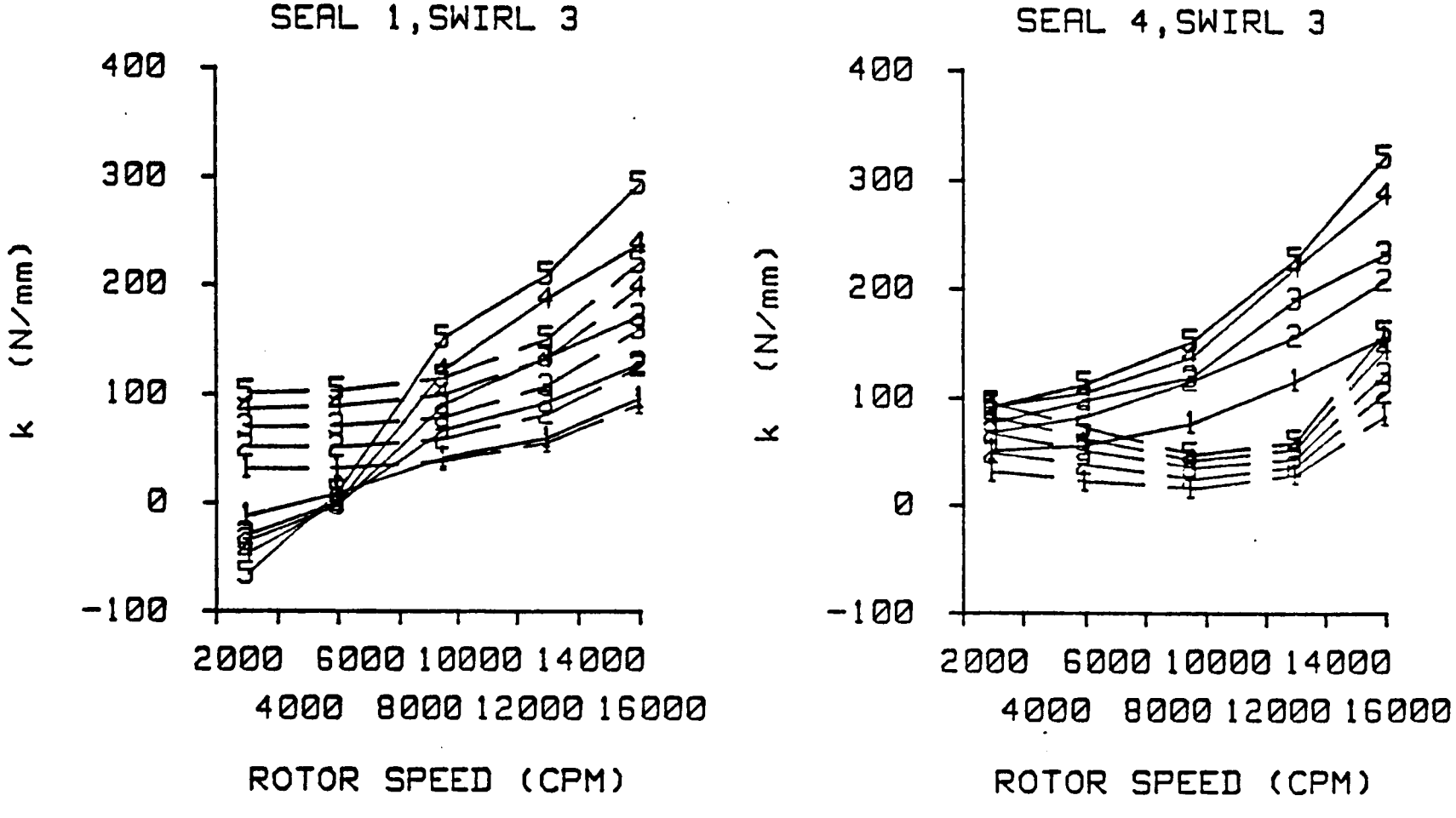

Figure 67. A comparison of experimental and theoretical cross-coupled stiffness versus rotor speed for seals 1 & 4 and inlet circumferential velocity 3. Inlet pressures 1–5 are plotted (see Table 2). Honeycomb stator (left), smooth stator (right).

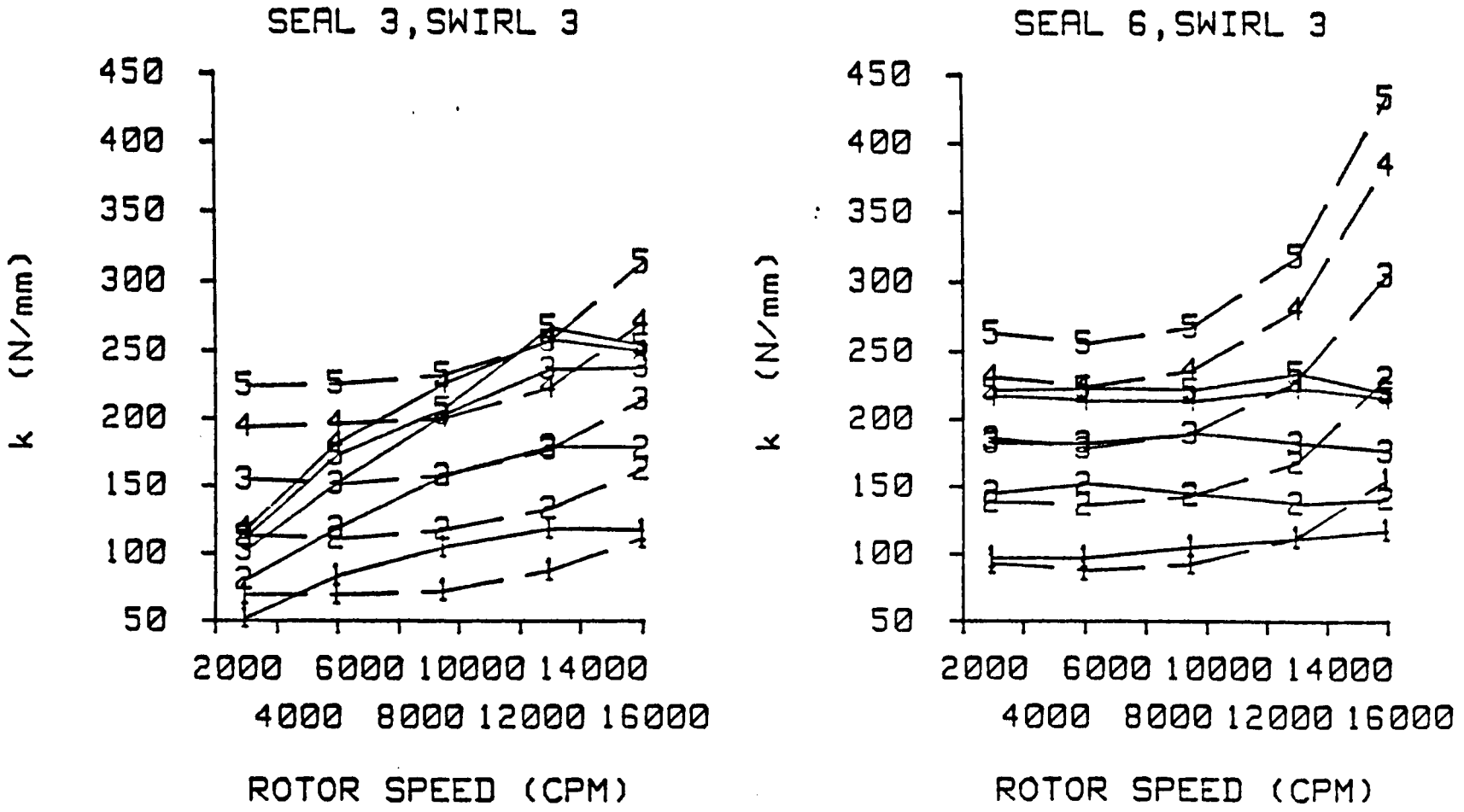

Figure 68. A comparison of experimental and theoretical cross-coupled stiffness versus rotor speed for seals 3 & 6 and inlet circumferential velocity 3. Inlet pressures 1–5 are plotted (see Table 2). Honeycomb stator (left), smooth stator (right).

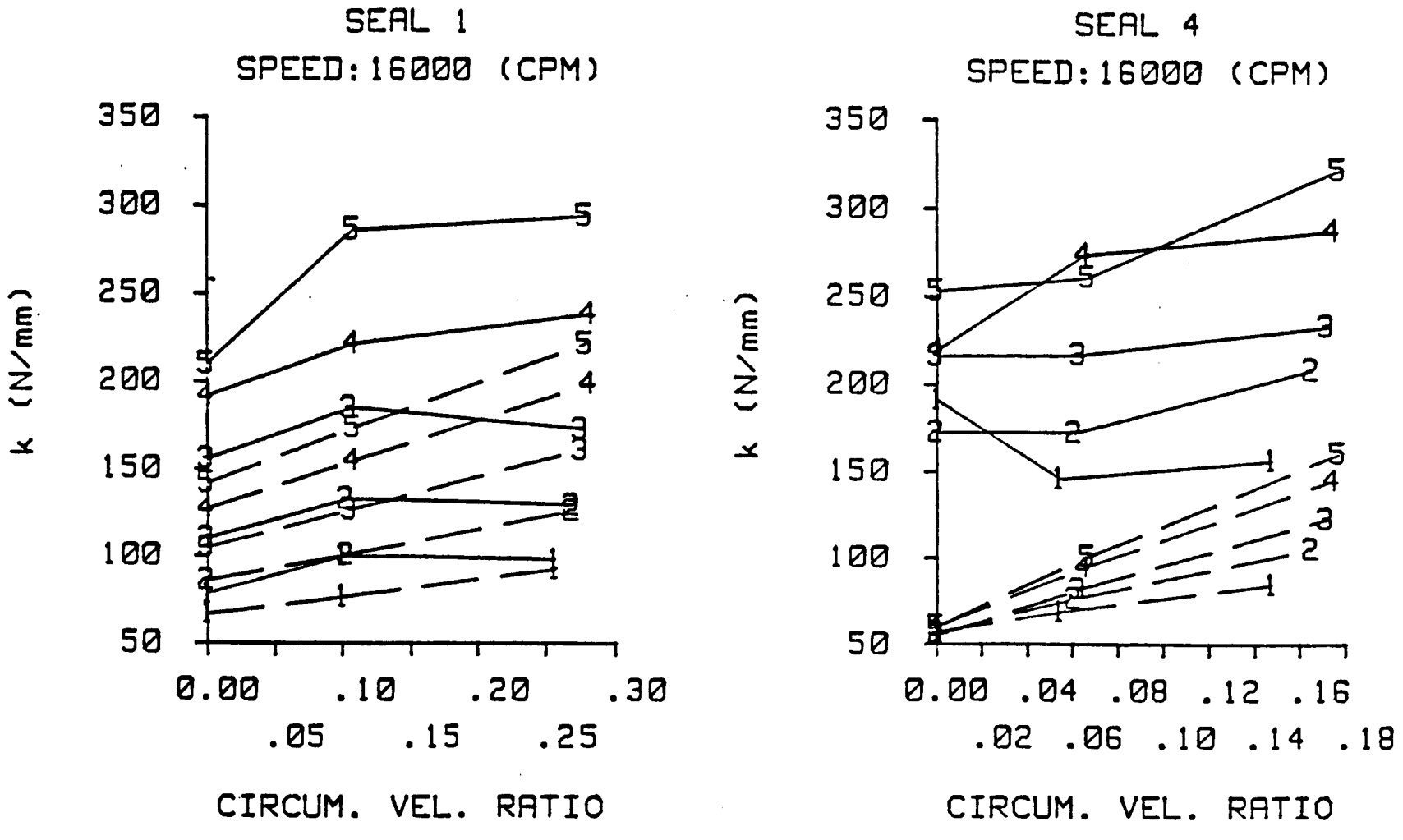

Figure 69. A comparison of experimental and theoretical cross-coupled stiffness versus inlet circumferential ratio for seal 1 and rotor speed of 16000 cpm. Inlet pressures 1–5 are plotted (see Table 2). Honeycomb stator (left), smooth stator (right).

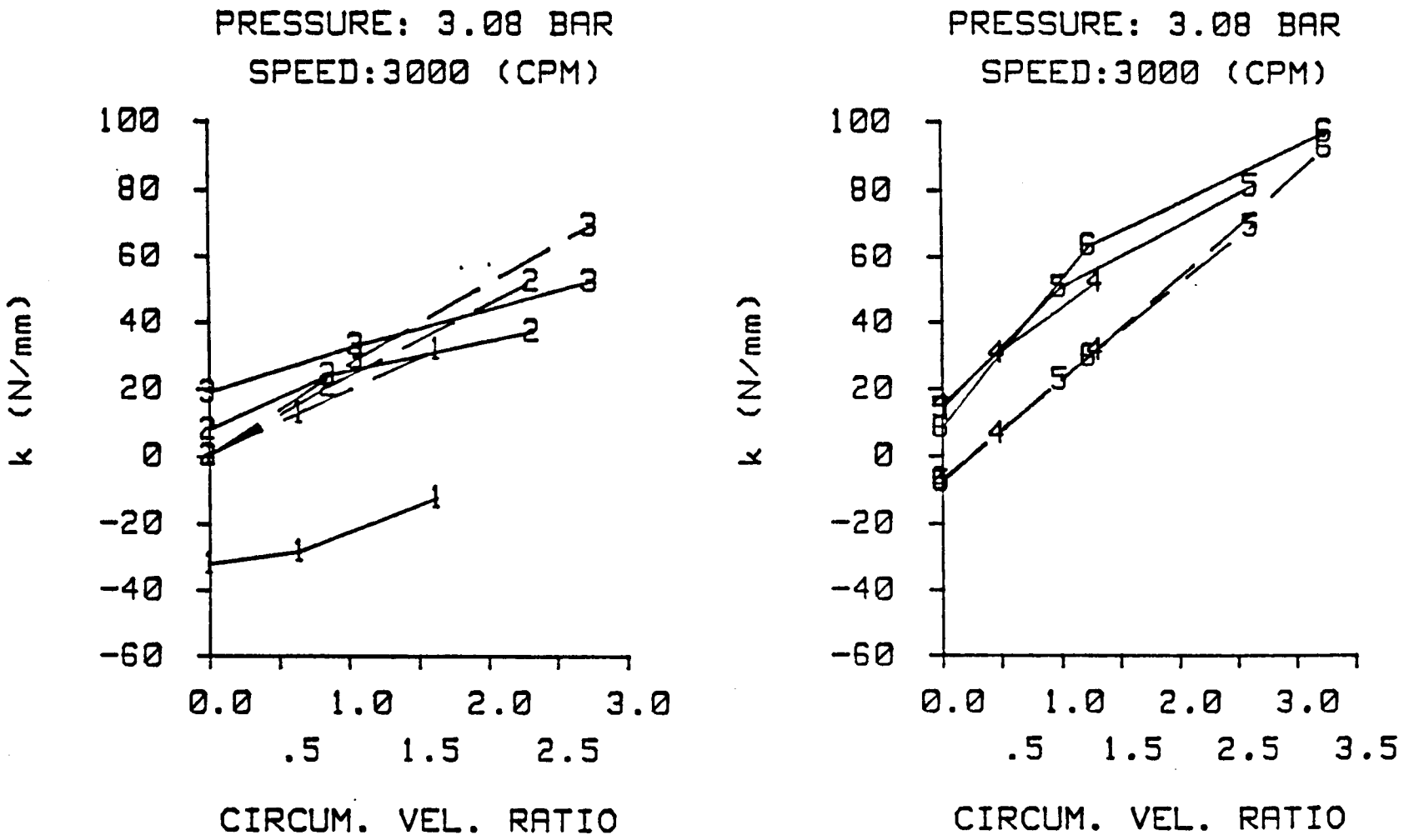

Figure 70. A comparison of experimental and theoretical cross-coupled stiffness versus inlet circumferential velocity ratio for inlet pressure of 3.08 bar and rotor speed of 3000 cpm. Three clearances are plotted (see Table 1). Honeycomb stator (left), smooth stator (right).

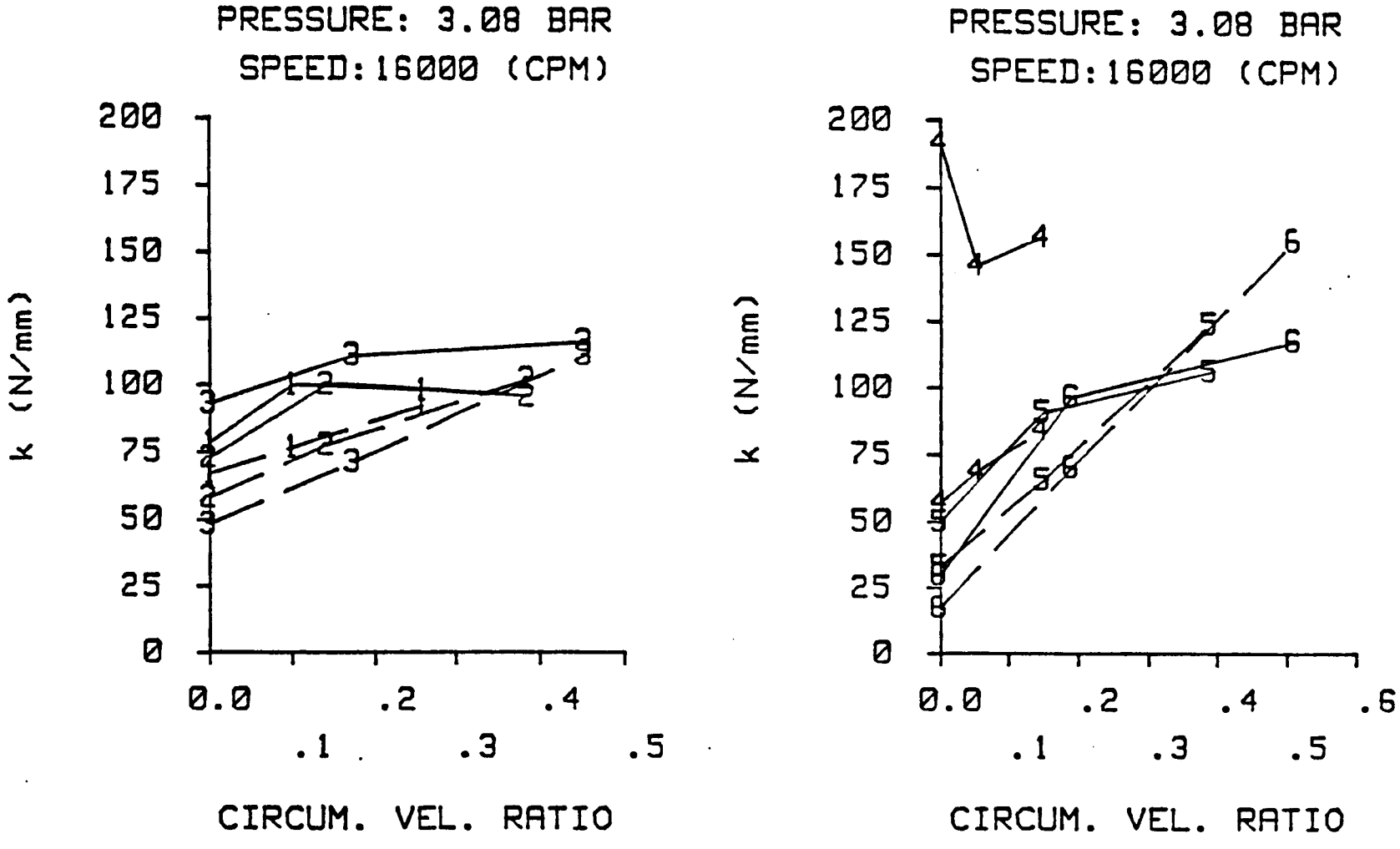

Figure 71. A comparison of experimental and theoretical cross-coupled stiffness versus inlet circumferential velocity ratio for inlet pressure of 3.08 bar and rotor speed of 16000 cpm. Three clearances are plotted (see Table 1). Honeycomb stator (left), smooth stator (right).

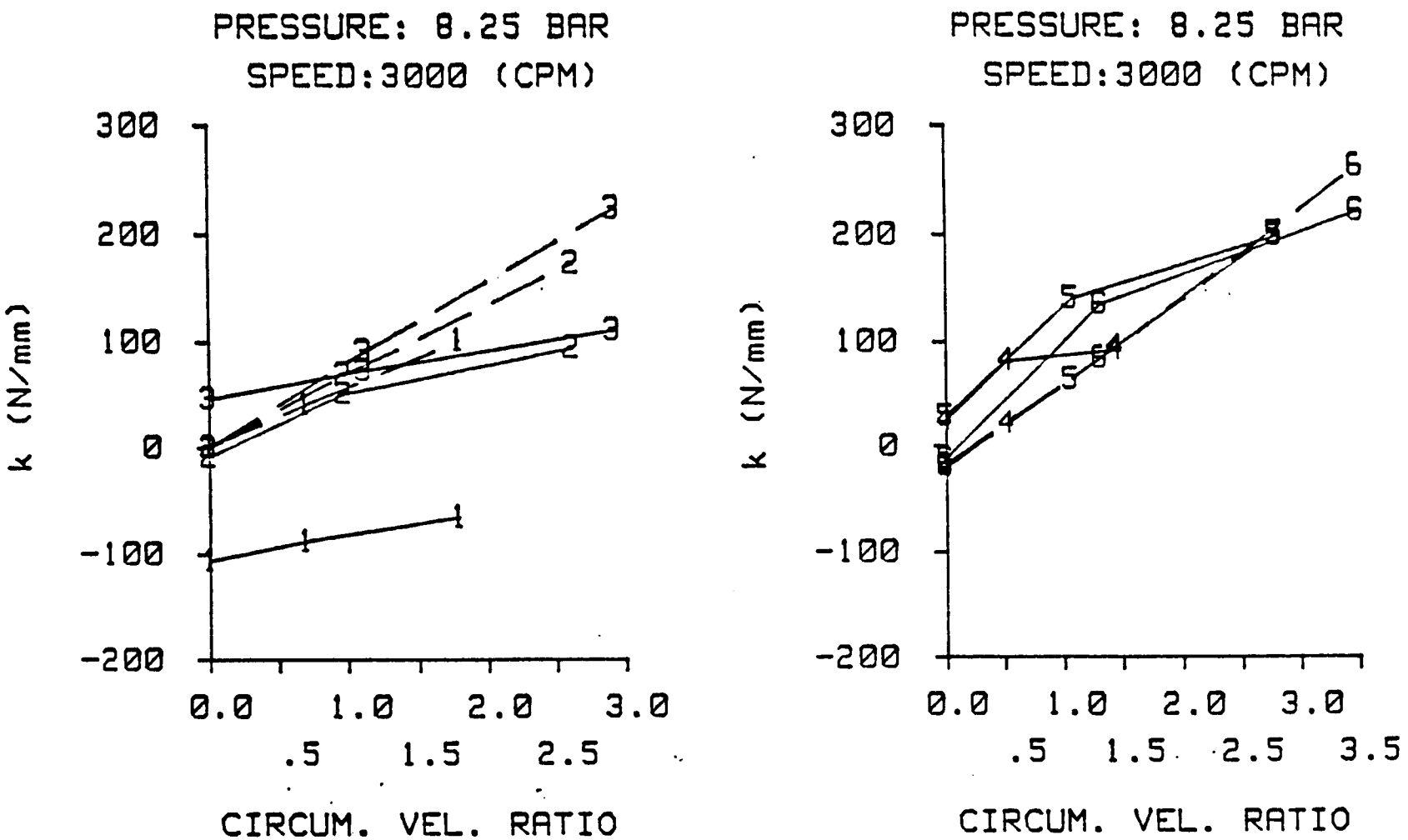

Figure 72. A comparison of experimental and theoretical cross-coupled stiffness versus inlet circumferential velocity ratio for inlet pressure of 8.25 bar and rotor speed of 3000 cpm. Three clearances are plotted (see Table 1). Honeycomb stator (left), smooth stator (right).

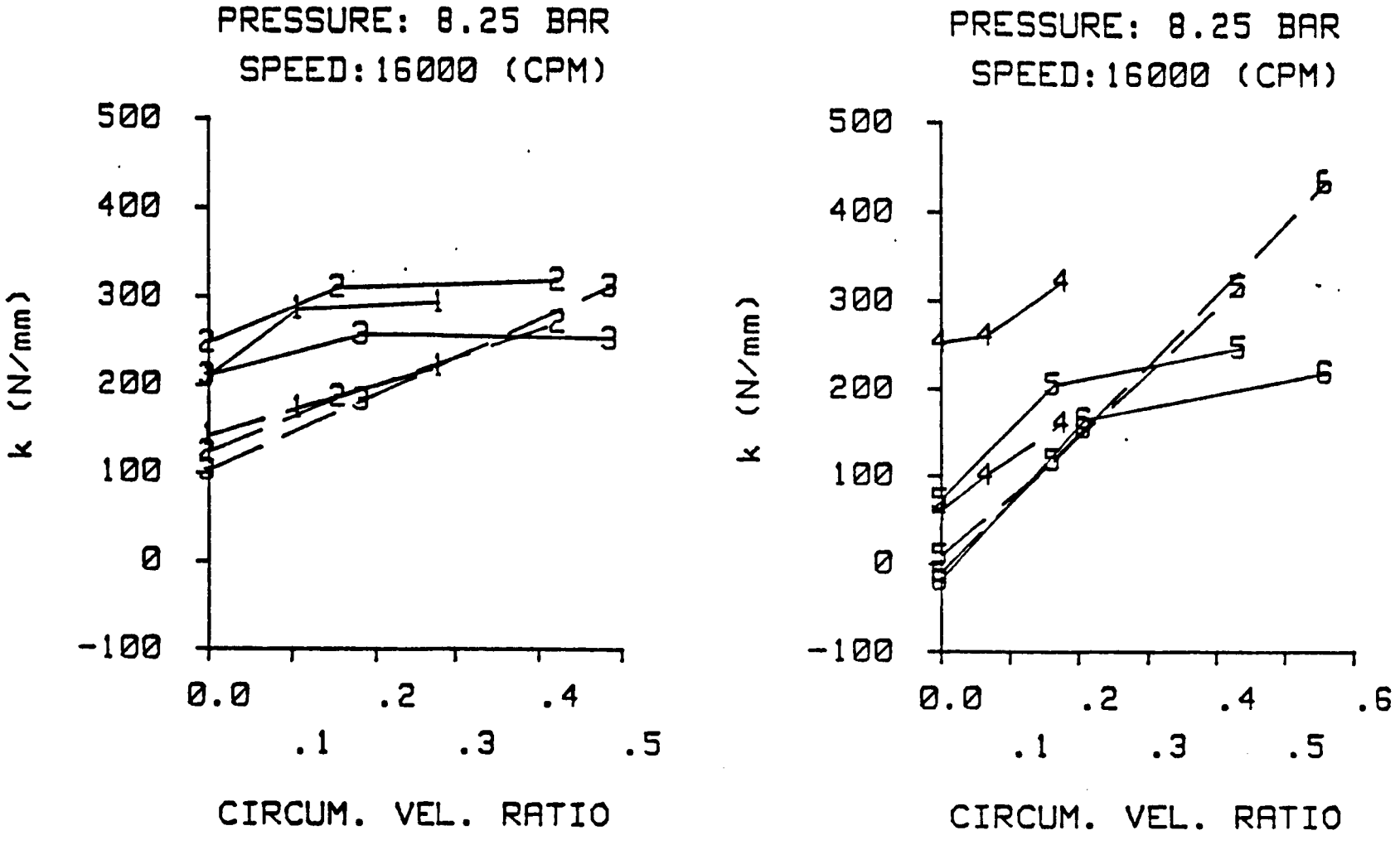

Figure 73. A comparison of experimental and theoretical cross-coupled stiffness versus inlet circumferential velocity ratio for inlet pressure of 8.25 bar and rotor speed of 16000 cpm. Three clearances are plotted (see Table 1). Honeycomb stator (left), smooth stator (right).

Figure 69 is a plot of cross-coupled stiffness versus circumferential velocity ratio for the smallest clearance seals. The theory predicts a linear increase in cross-coupled stiffness with increasing tangential velocity for both seals. The test data indicate a somewhat less than linear trend.

Figures 70–73 show the effect of clearance on cross-coupled stiffness. The model predicts that there is a weak increase in cross-coupled stiffness with clearance at low rotor speeds and a weak decrease in cross-coupled stiffness with clearance at high rotor speeds. This trend is generally supported by the data except for the smallest clearance. Also, the model prediction of cross-coupled stiffness magnitude is much better for the two larger clearance seals.

DIRECT DAMPING

Figures 74–79 provide comparisons of theoretical direct damping to experimental data for both stator surfaces. Direct damping is plotted versus rotor speed in figure 74. The theoretical model predicts a rise in direct damping with rotor speed for both stator surfaces. This does not agree with the test data in either case. The model also predicts that damping is always higher for the honeycomb stator seal compared to the smooth stator seal, whereas this is not consistently observed in the test data. Direct damping is plotted versus circumferential velocity ratio in figure 75. The theoretical model correctly predicts that direct damping is insensitive to changes in inlet tangential velocity.

Figures 76–79 show the effect of clearance on direct damping. The model predicts a small increase in damping with clearance. For the honeycomb stator seal, the experimental data show this trend between the two larger clearances; however, there is much less damping at the smallest clearance. For the smooth

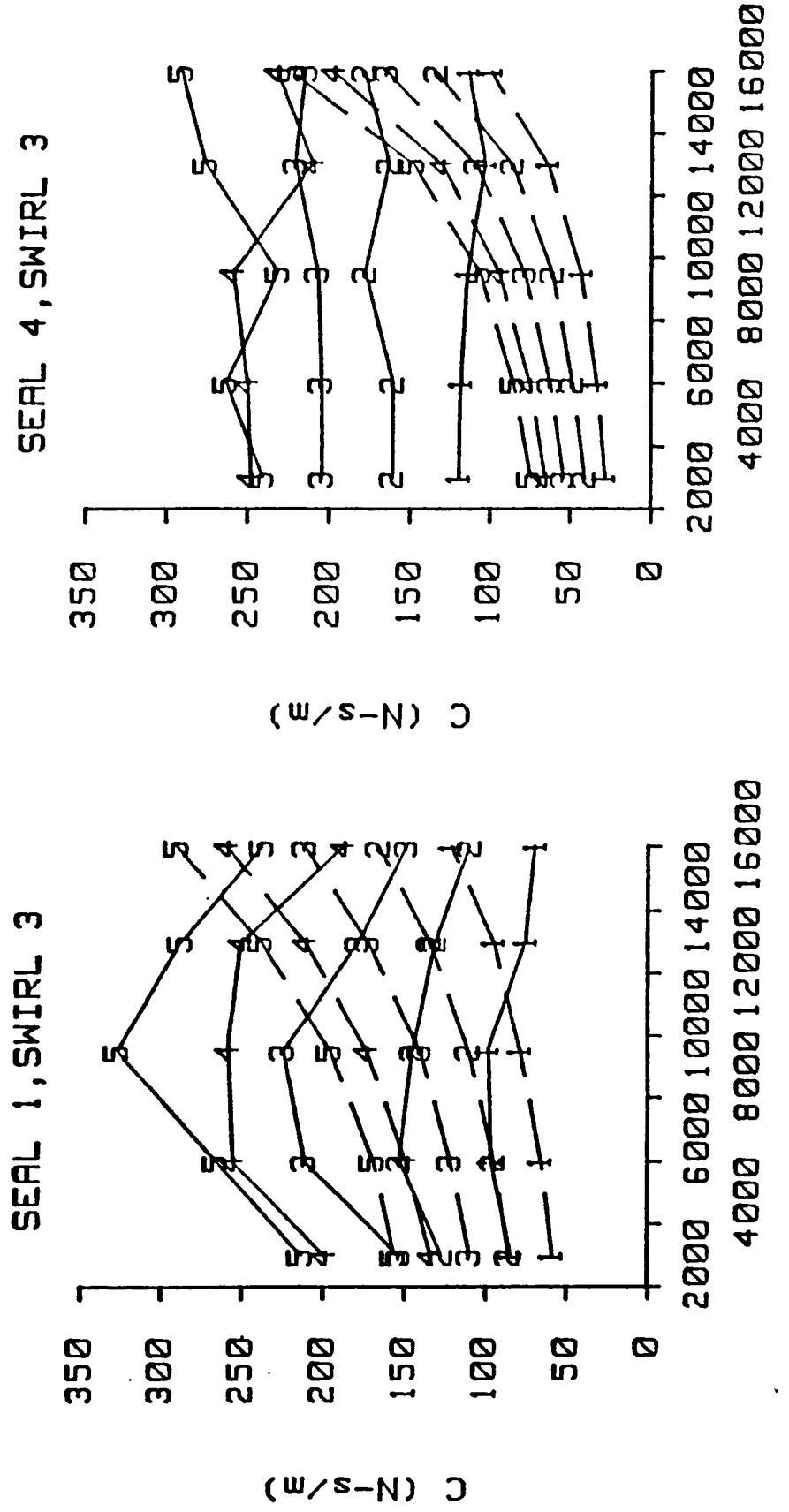

Figure 74. A comparison of experimental and theoretical direct damping versus rotor speed for seals 1 & 4 and inlet circumferential velocity 3. Inlet pressures 1-5 are plotted (see Table 2). Honeycomb stator (left), smooth stator (right).

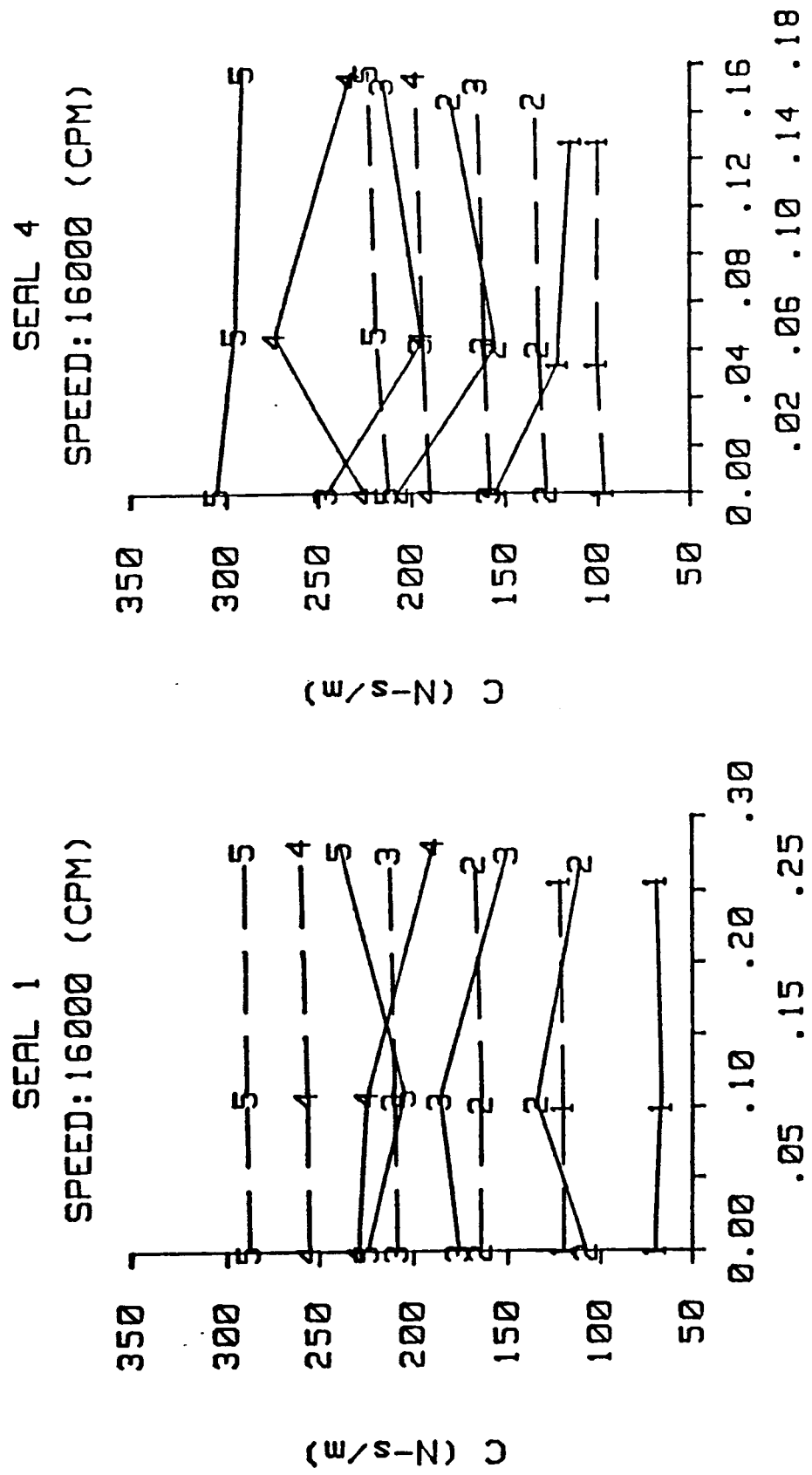

Figure 75. A comparison of experimental and theoretical direct damping versus inlet circumferential velocity ratio for seals 1 & 4 and rotor speed of 16000 cpm. Inlet pressures 1–5 are plotted (see Table 2). Honeycomb stator (left), smooth stator (right).

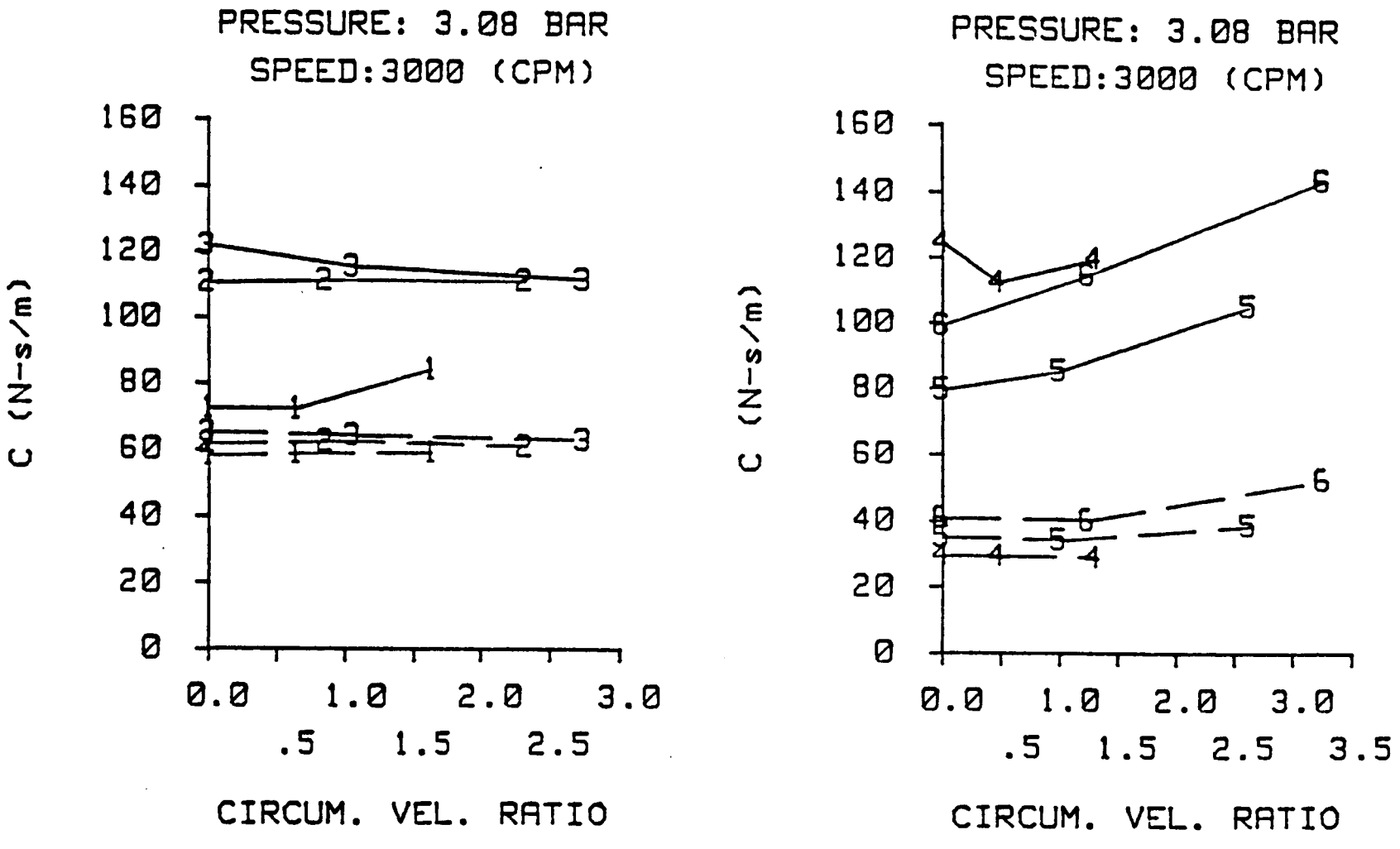

Figure 76. A comparison of experimental and theoretical direct damping versus inlet circumferential velocity ratio for inlet pressure of 3.08 bar and rotor speed of 3000 cpm. Three clearances are plotted (see Table 1). Honeycomb stator (left), smooth stator (right).

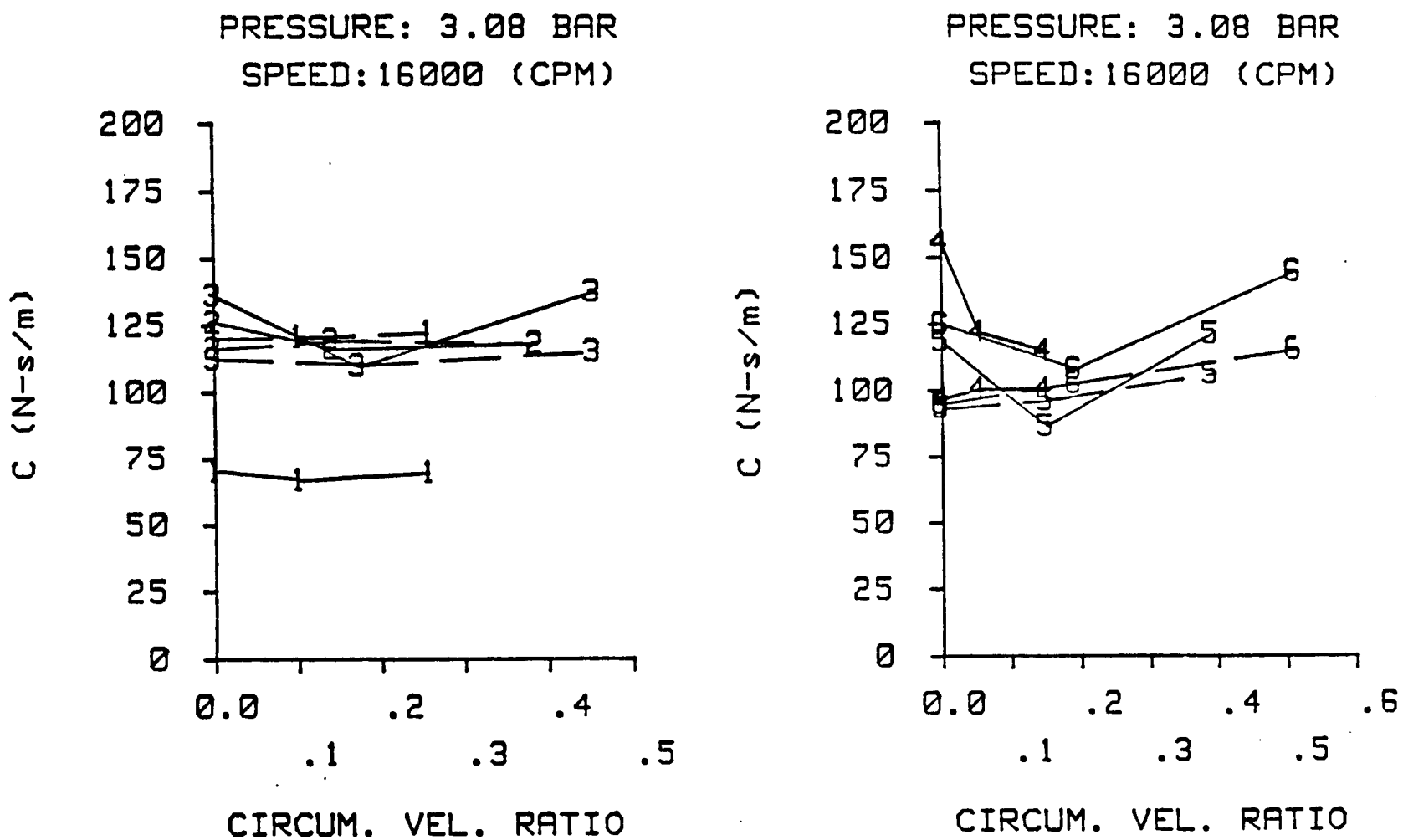

Figure 77. **A comparison of experimental and theoretical direct damping versus inlet circumferential velocity ratio for inlet pressure of 3.08 bar and rotor speed of 16000 cpm. Three clearances are plotted (see Table 1). Honeycomb stator (left), smooth stator (right).**

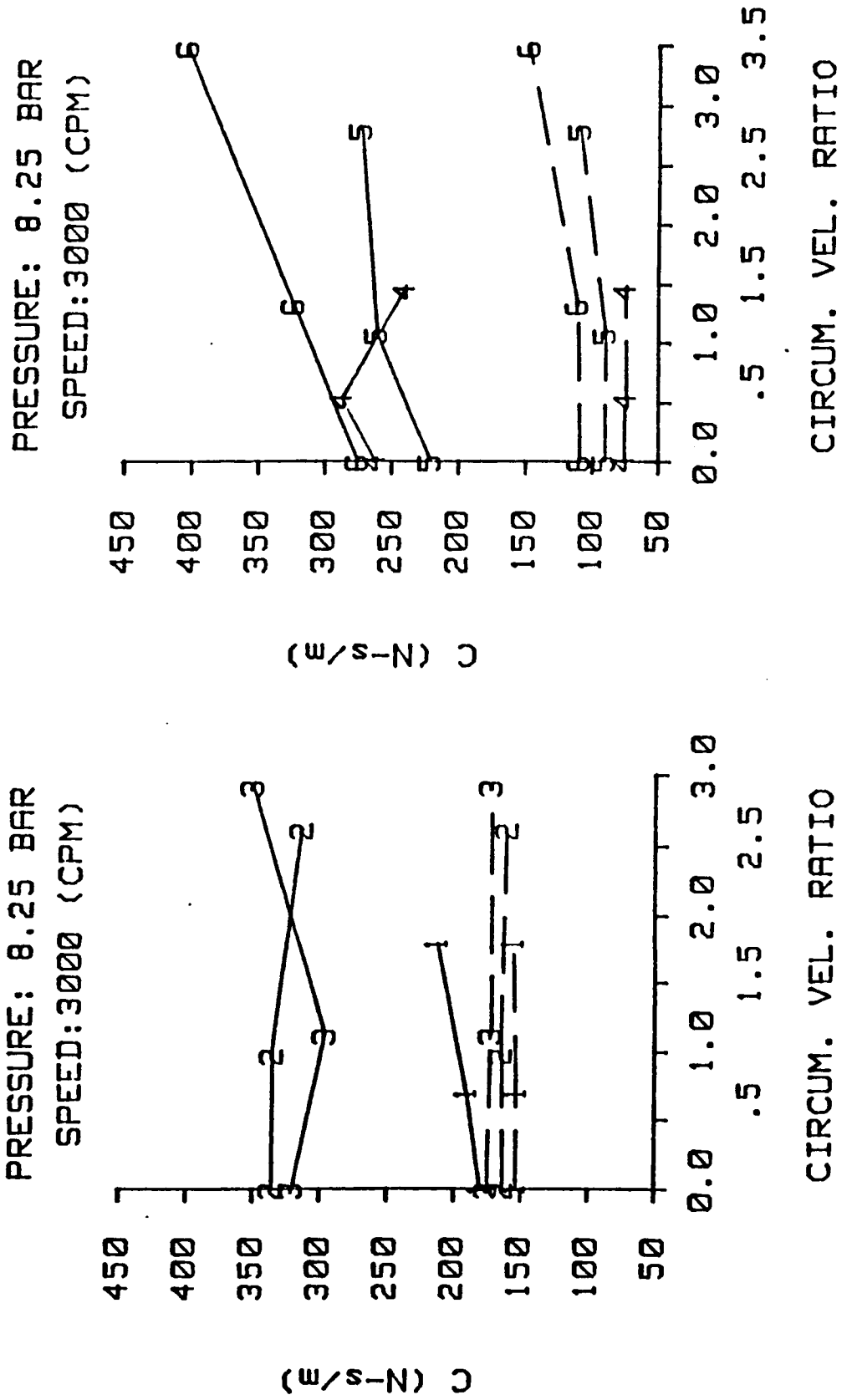

Figure 78. A comparison of experimental and theoretical direct damping versus inlet circumferential velocity ratio for inlet pressure of 8.25 bar and rotor speed of 3000 cpm. Three clearances are plotted (see Table 1). Honeycomb stator (left), smooth stator (right).

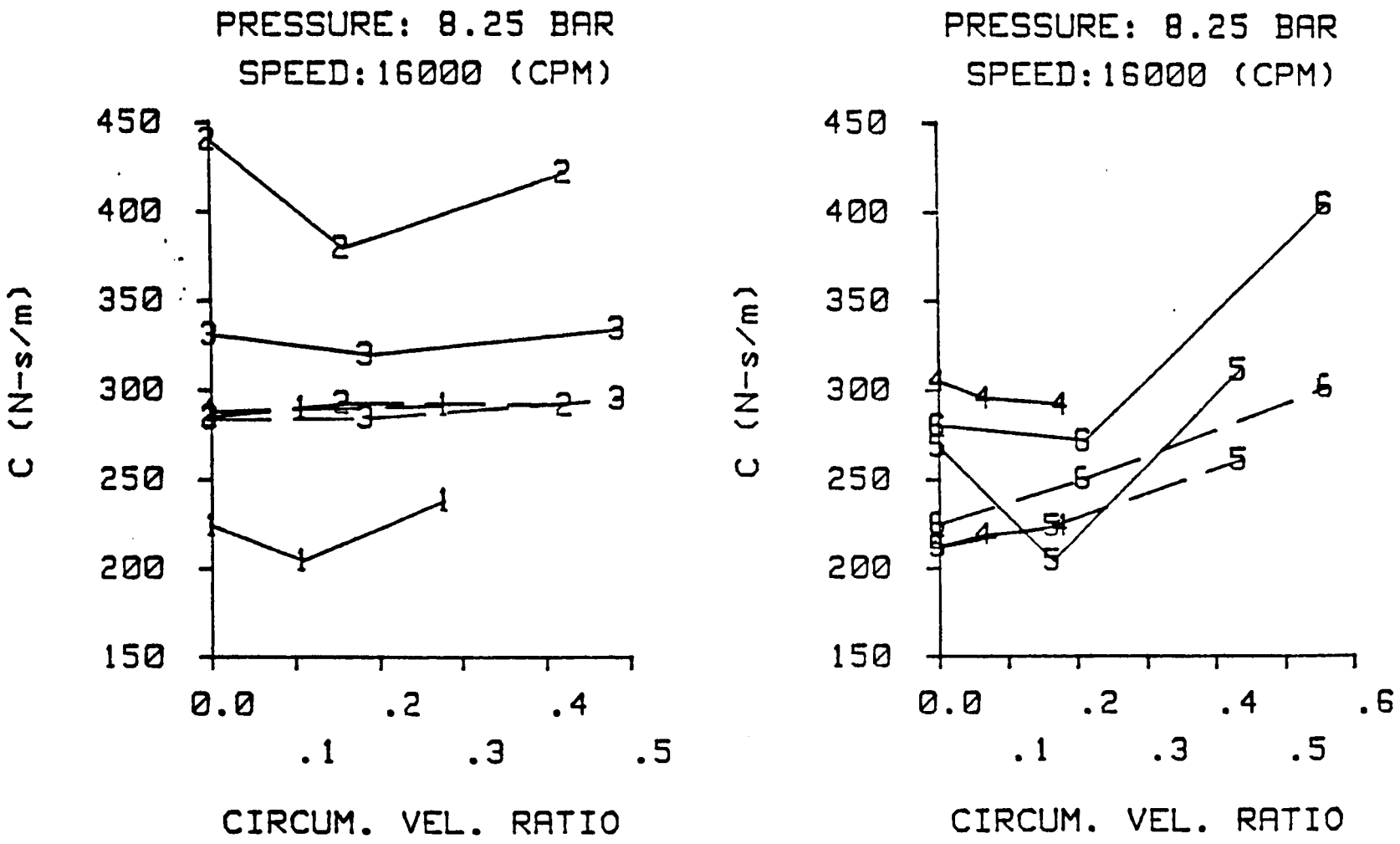

Figure 79. A comparison of experimental and theoretical direct damping versus inlet circumferential velocity ratio for inlet pressure of 8.25 bar and rotor speed of 16000 cpm. Three clearances are plotted (see Table 1). Honeycomb stator (left), smooth stator (right).

stator seal, the experimental data again agree with the predicted trend at the larger clearances; but, damping at the smallest clearance is larger than at the larger clearances. Additionally, the model predicts direct damping well at high rotor speeds for the larger clearances. The model prediction is about 50% low for the larger clearances at low rotor speeds.

CHAPTER VII

CONCLUSIONS

The test data support the following conclusions for the labyrinth-rotor/honeycomb-stator seals:

1) Direct stiffness is negative. Direct stiffness becomes more negative with clearance when clearance is small, but begins to become more positive as clearance gets large.

2) Cross-coupled stiffness is generally positive. Cross-coupled stiffness increases with rotor speed and with inlet tangential velocity. At the lower rotor speeds, cross-coupled stiffness is much lower for the smallest clearance seal than for the other two seals. At the higher rotor speeds, cross-coupled stiffness is approximately the same value regardless of clearance.

3) Direct damping is positive. Direct damping is much lower in the smallest clearance seal than in the two larger clearance seals.

By comparison of the results for the honeycomb stator seals to the results for the smooth stator seals, the following conclusions may be drawn:

1) The honeycomb stator seals leak more than the smooth stator seals when the clearance is low. The honeycomb stator seals leak less when the clearance is high. This result is consistent with the results of Stocker et al. [22].

2) The honeycomb stator seal is more stable at low rotor speeds. For high rotor speeds and small clearance, the smooth stator seal is more stable. For high rotor speeds and larger clearance, the two seals are equally stable.

By comparison of the experimental results to theoretical predictions, the following conclusions may be draw:

1) The model predicts that direct stiffness depends on rotor speed, whereas the experimental data shows that it does not. The model predicts that direct stiffness magnitude of the smooth stator seal is always higher than for the honeycomb stator seal. This conclusion is not supported by the data either. The model also predicts incorrectly that direct stiffness is positive at low rotor speeds.

2) The model underpredicts the rotor speed dependence of cross-coupled stiffness in the honeycomb stator seal. The model overpredicts the rotor speed dependence of cross-coupled stiffness in the smooth stator seal, particularly at the larger clearances.

3) The model consistently predicts the value of cross-coupled stiffness of the honeycomb stator seal correctly within 25% of the measured values. The model correctly predicts that the dependence of cross-coupled stiffness on clearance is very weak.

4) The model incorrectly predicts that direct damping increases with speed, and does not predict the decrease in damping at small clearance. For the two larger clearance seals the model produces good results for rotor speeds above

12,000 cpm. Below 12,000 cpm, the model underpredicts direct damping by 50%.

In general, Scharrer's model gives useful results for cross-coupled stiffness in the honeycomb-stator/labyrinth-rotor seal for the range of variables tested. Scharrer's model can give good results for direct damping in the honeycomb-stator/labyrinth-rotor seal by applying a correction factor to increase the damping at low rotor speeds. Overall, the model produces better results for the larger clearances.

Values of the rotordynamic coefficients for the two larger clearance seals tend to be much closer together than to the smaller clearance seal. This is true for both the honeycomb-stator/labyrinth-rotor seal and for the previously untested smallest clearance smooth-stator/labyrinth-rotor seal. Since there are many practical applications where labyrinth seals are used with clearances below the tested range, further testing with smaller clearances are required.

REFERENCES

1 Benckert, H., and Wachter, J., 1978, "Querkrafte aus Spaltdichtungen-Eine mogliche Ursache fur die Laufunruhe von Turbomaschinen," *Atomkernenergie,"*32, Lfg. 4, pp. 239-246.

2 Benckert, H., and Wachter, J., 1980, "Flow Induced Spring Coefficients of Labyrinth Seals for Applications in Rotordynamics,," NASA CP 2133, Proceedings from a workshop on Rotordynamic Instability Problems in High-Performance Turbomachinery–1980, held at Texas A&M University, College Station, TX, pp. 189-212.

3 Benckert, H., 1980, "Stromungsbedinte Federkennwerte in Labyrinthdichtungen," Doctoral dissertation at University of Stuttgart.

4 Wright, D., 1983, "Labyrinth Seal Forces on a Whirling Rotor," *Rotor Dynamical Instability,* ASME, New York, pp. 19-31.

5 Childs, D. and Scharrer, J., 1986, "Experimental Rotordynamic Coefficient Results for Teeth-On-Rotor and Teeth-On-Stator Labyrinth Gas Seals," ASME Paper No. 86-GT-12, Also accepted for *ASME Journal of Engineering for Gas Turbines and Power.*

6 Alford, J., 1965, "Protecting Turbomachinery from Self-Excited Rotor Whirl," Trans. *ASME, Journal of Engineering for Power,*pp. 333-344.

7 Kostyuk, A., 1972, "A Theoretical Analysis of the Aerodynamic Force in the Labyrinth Glands of Turbomachines," *Teploenergetica,*19(11)0, pp. 39-44.

8 Iwatsubo, T., 1980, "Evaluation of Instability Forces of Labyrinth Seals in Turbines or Compressors," NASA CP 2133, Proceedings from a workshop on Rotordynamic Instability Problems in High-Performance Turbomachinery–1980, held at Texas A&M University, College Station, TX, pp. 139-167.

9 Gans, B., 1983, "Prediction of the Aero-Elastic Force in a Labyrinth Type Seal and its Impact on Turbomachinery Stability," M.S. Thesis, M.I.T.

10 Childs, D. and Scharrer, J., 1986, "An Iwatsubo Based Solution for Labyrinth Seals: A Comparison to Experimental Results," *ASME Journal of Engineering for Gas Turbines and Power,* April, Vol. 108, pp. 325-331.

11 Fujikawa, T., Kameoka, T., and Abe, T., 1984, "A Theoretical Approach to Labyrinth Seal Forces," NASA CP 2338, Proceedings from a workshop on Rotordynamic Instability Problems in High-Performance Turbomachinery–1984, held at Texas A&M University, College Station, TX, pp. 173-186.

12 Wyssmann, H., Jenny, R., and Pham, T., 1984, "Prediction of Stiffness and Damping Coefficients for Centrifugal Compressor Labyrinth Seals," ASME

84-GT-86. Presented at the 29th International Gas Turbine Conference and Exhibit, Amsterdam, The Netherlands.

13 Scharrer, J.K., 1987, "A Comparison of Experimental and Theoretical Results for Labyrinth Gas Seals," Doctoral Dissertation, Texas A&M University, College Station, TX.

14 Elrod, D., and Childs, D., 1988, "Experimental Rotordynamic Coefficient Results for Honeycomb Seals", Texas A&M Turbomachinery Laboratory Report TRC-Seal-1-88.

15 Iwatsubo, T., Matooka, N., and Kawai, R., 1982, "Flow Induced Force and Flow Patterns of Labyrinth Seals," NASA CP 2250, Proceedings from a workshop on Rotordynamic Instability Problems in High-Performance Turbomachinery–1982, held at Texas A&M University, College Station, TX, pp. 205-222.

16 Yamada, Y., 1961, *Trans. Japan Soc. Mechanical Engineers*, Vol. 27, No. 180, p. 1267.

17 Elrod, D., February 5, 1988, Unpublished data (Private collection, Hawkins).

18 Iino, T., and Kaneko, H., 1980, "Hydraulic Forces Caused by Annular Pressure Seals in Centrifugal Pumps," NASA CP 2133, Proceedings from a workshop on Rotordynamic Instability Problems in High-Performance Turbomachinery–1980, held at Texas A&M University, College Station, TX, pp. 213-225.

19 Bowen, W.L., and Bhateje, R., 1979, "The Hollow Roller Bearing," ASME Paper No. 79-LUB-15, ASME-ASLE Lubrication Conference, Dayton, Ohio.

20 Cohen, H., Rogers, G., and Saravanamuttoo, H., 1972, *Gas Turbine Theory*, Longman Group Limited, London, England.

21 Holman, J., 1978,*Experimental Methods for Engineers*, McGraw-Hill, New York, pp. 45.

22 Stocker, H., Cox, D., and Holle, G., 1977, "Aerodynamic Performance of Conventional and Advanced Design Labyrinth Seals with Solid-Smooth, Abradable, and Honeycomb Lands," NASA CR-135307, pp. 63-72.

23 Schlichting, H., 1979, *Boundary Layer Theory*, McGraw-Hill, New York, p. 579.

APPENDIX

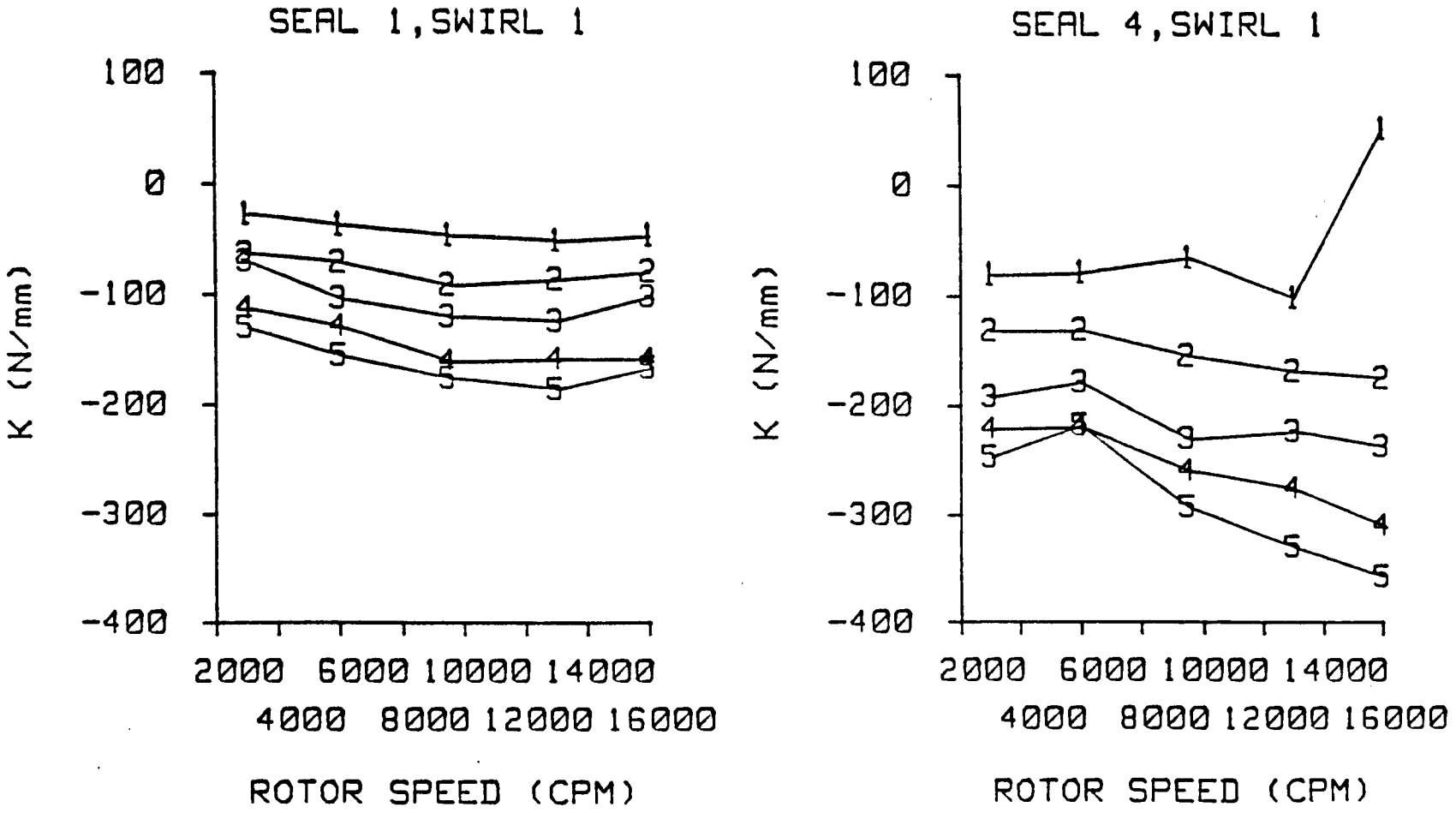

Figure A1. Direct stiffness versus rotor speed for seals 1 & 4 and inlet circumferential velocity 1. Inlet pressures 1–5 are plotted (see Table 2). Honeycomb stator (left), smooth stator (right).

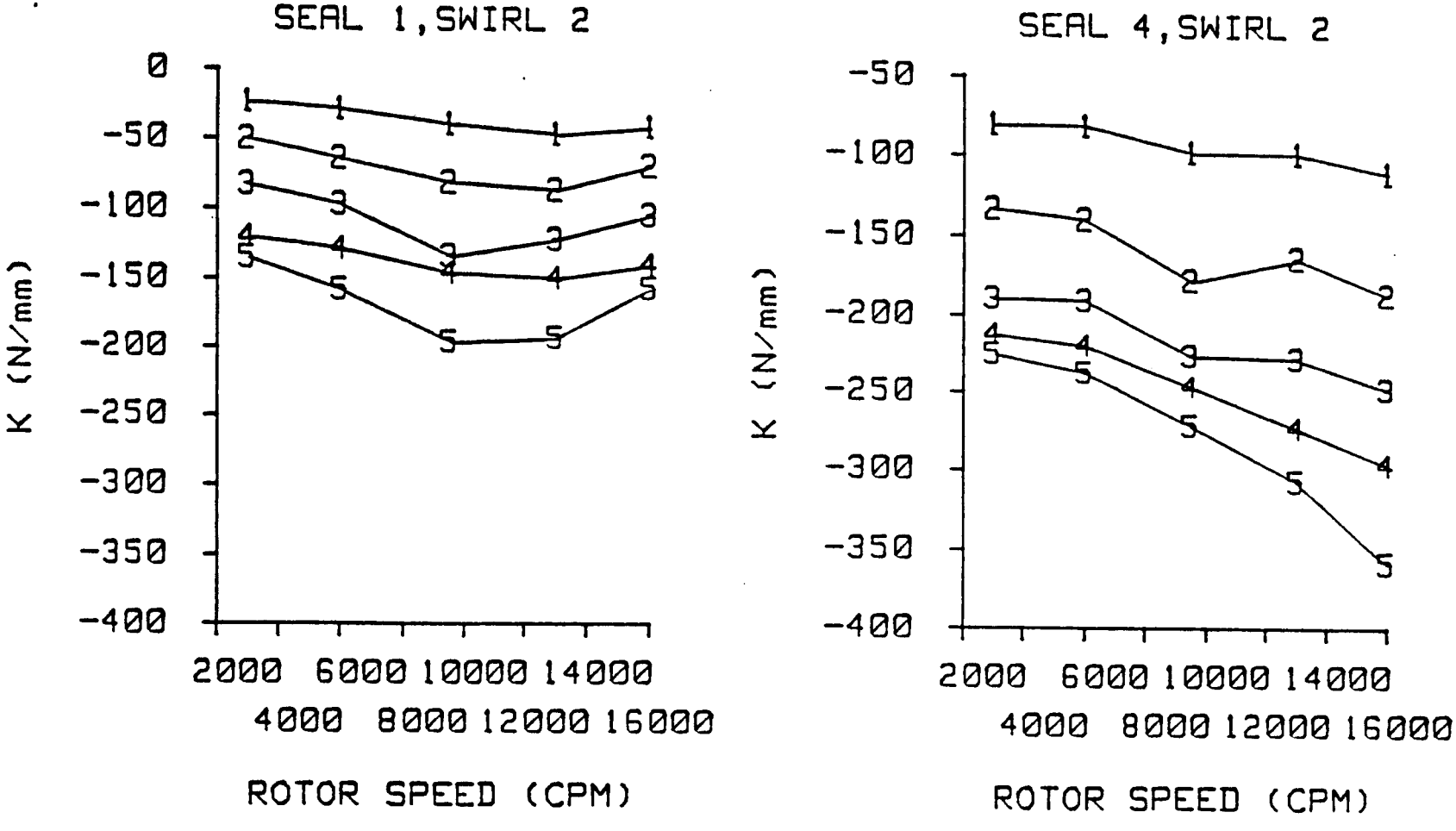

Figure A2. Direct stiffness versus rotor speed for seals 1 & 4 and inlet circumferential velocity 2. Inlet pressures 1–5 are plotted (see Table 2). Honeycomb stator (left), smooth stator (right).

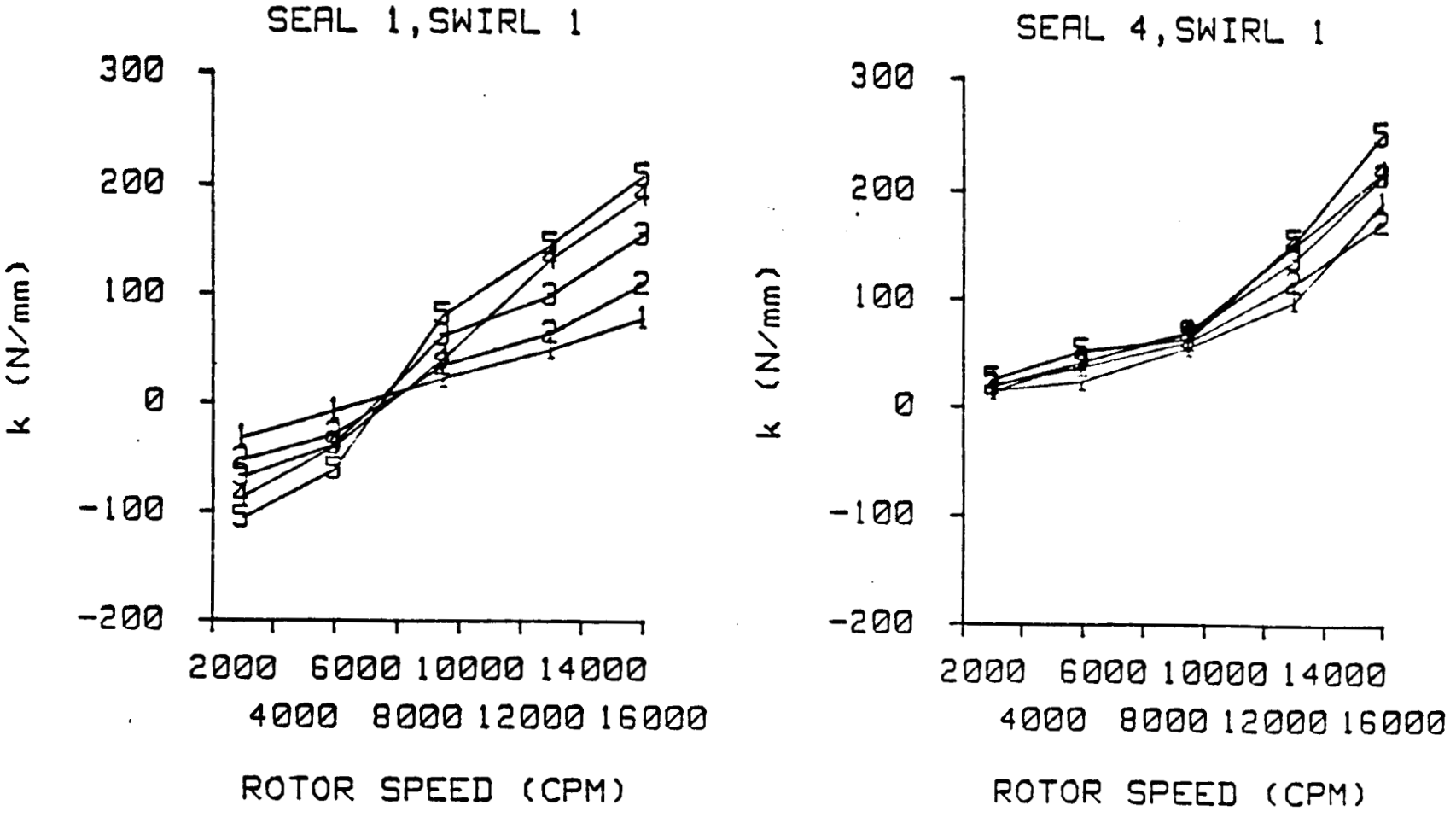

Figure A3. Cross-coupled stiffness versus rotor speed for seals 1 & 4 and inlet circumferential velocity 1. Inlet pressures 1–5 are plotted (see Table 2). Honeycomb stator (left), smooth stator (right).

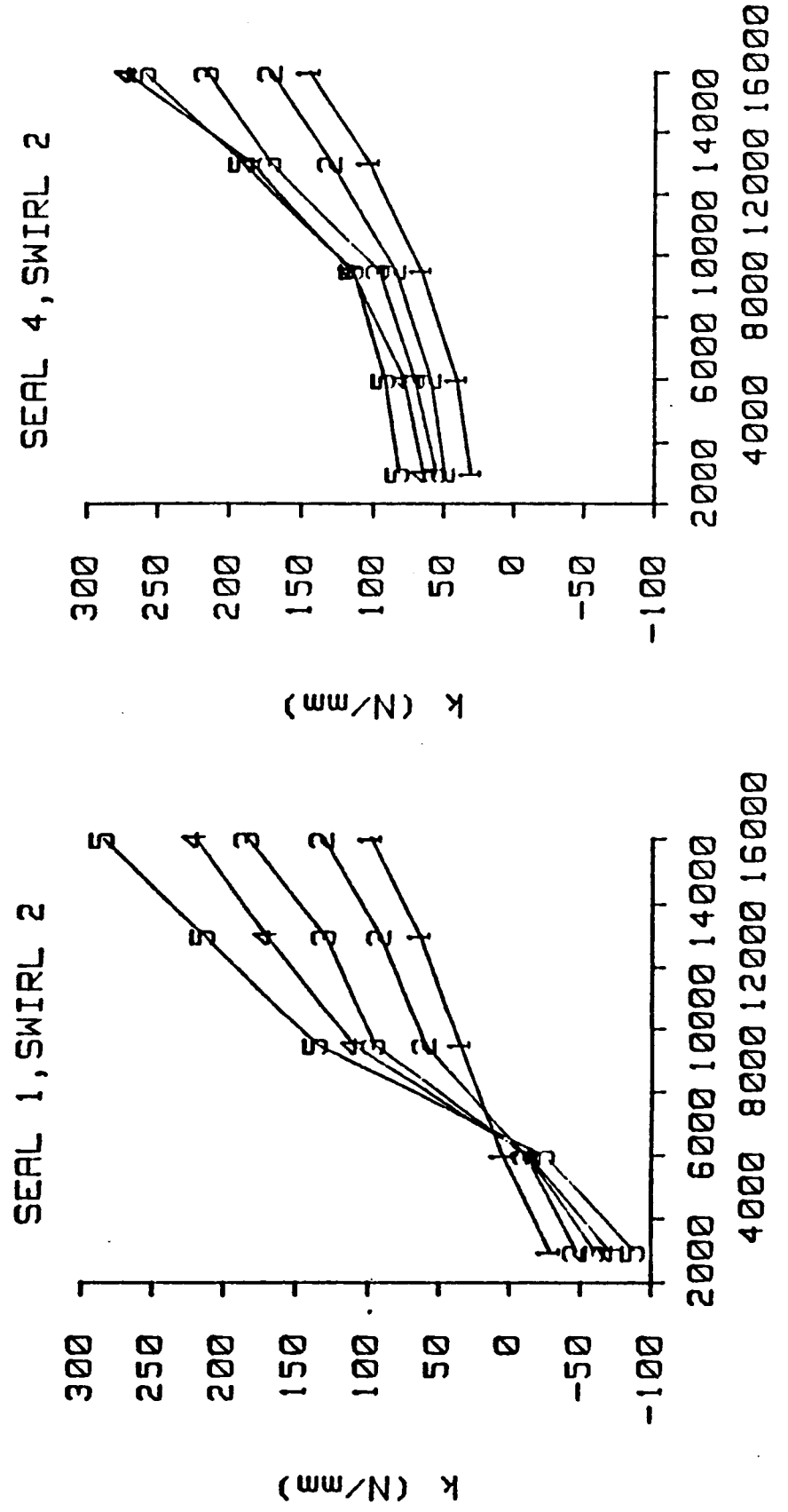

Figure A4. Cross-coupled stiffness versus rotor speed for seals 1 & 4 and inlet circumferential velocity 2. Inlet pressures 1–5 are plotted (see Table 2). Honeycomb stator (left), smooth stator (right).

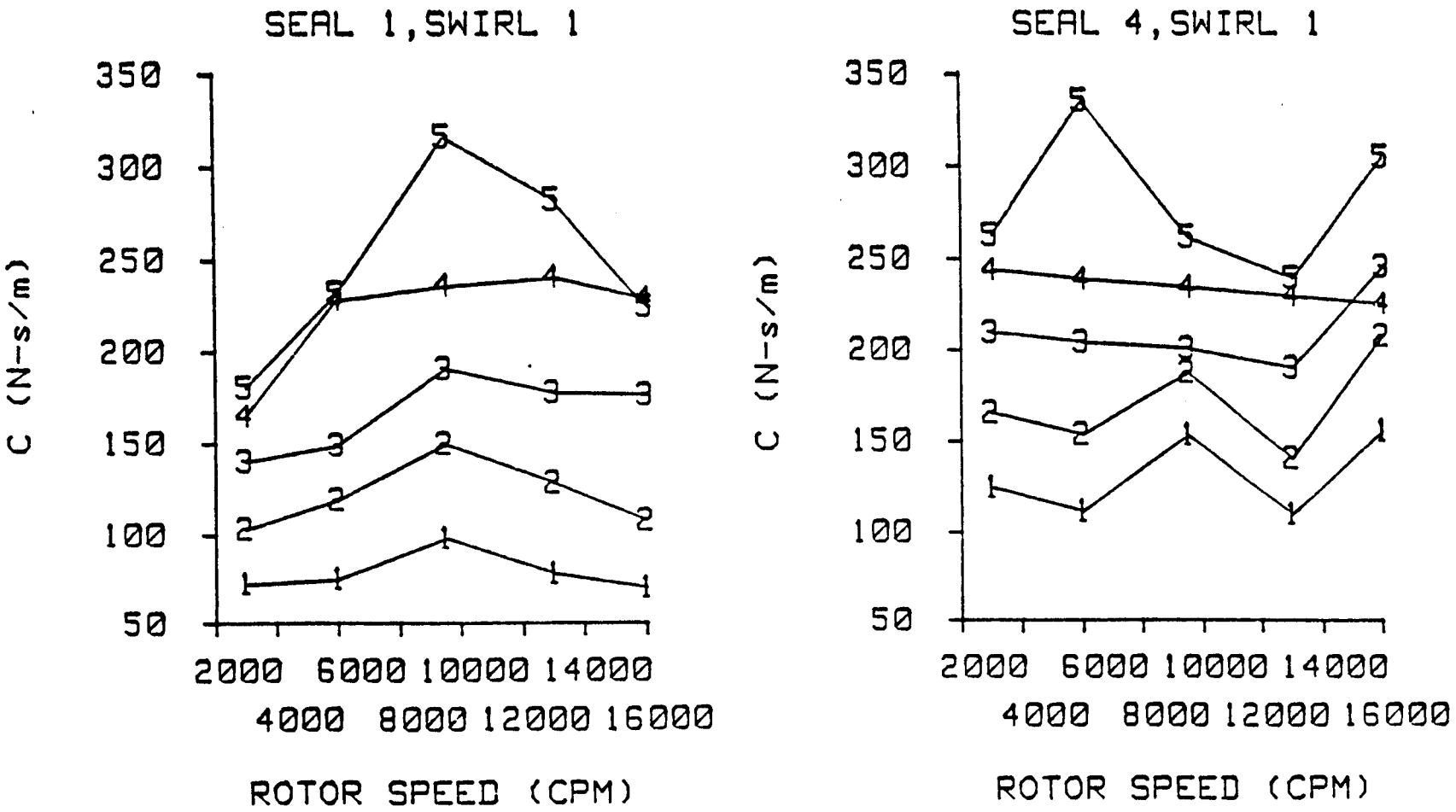

Figure A5. Direct damping versus rotor speed for seals 1 & 4 and inlet circumferential velocity 1. Inlet pressures 1–5 are plotted (see Table 2). Honeycomb stator (left), smooth stator (right).

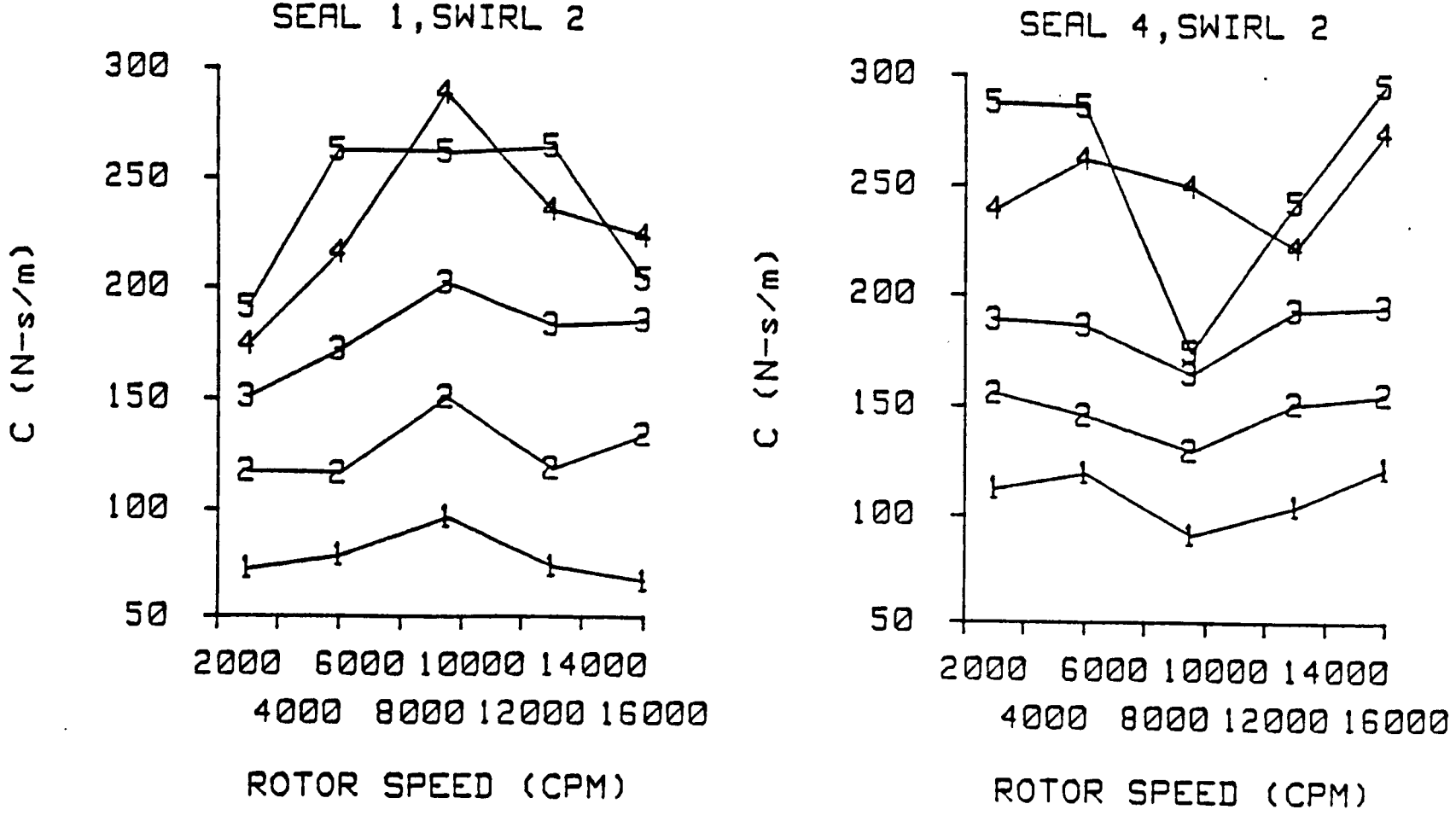

Figure A6. Direct damping versus rotor speed for seals 1 & 4 and inlet circumferential velocity 2. Inlet pressures 1–5 are plotted (see Table 2). Honeycomb stator (left), smooth stator (right).

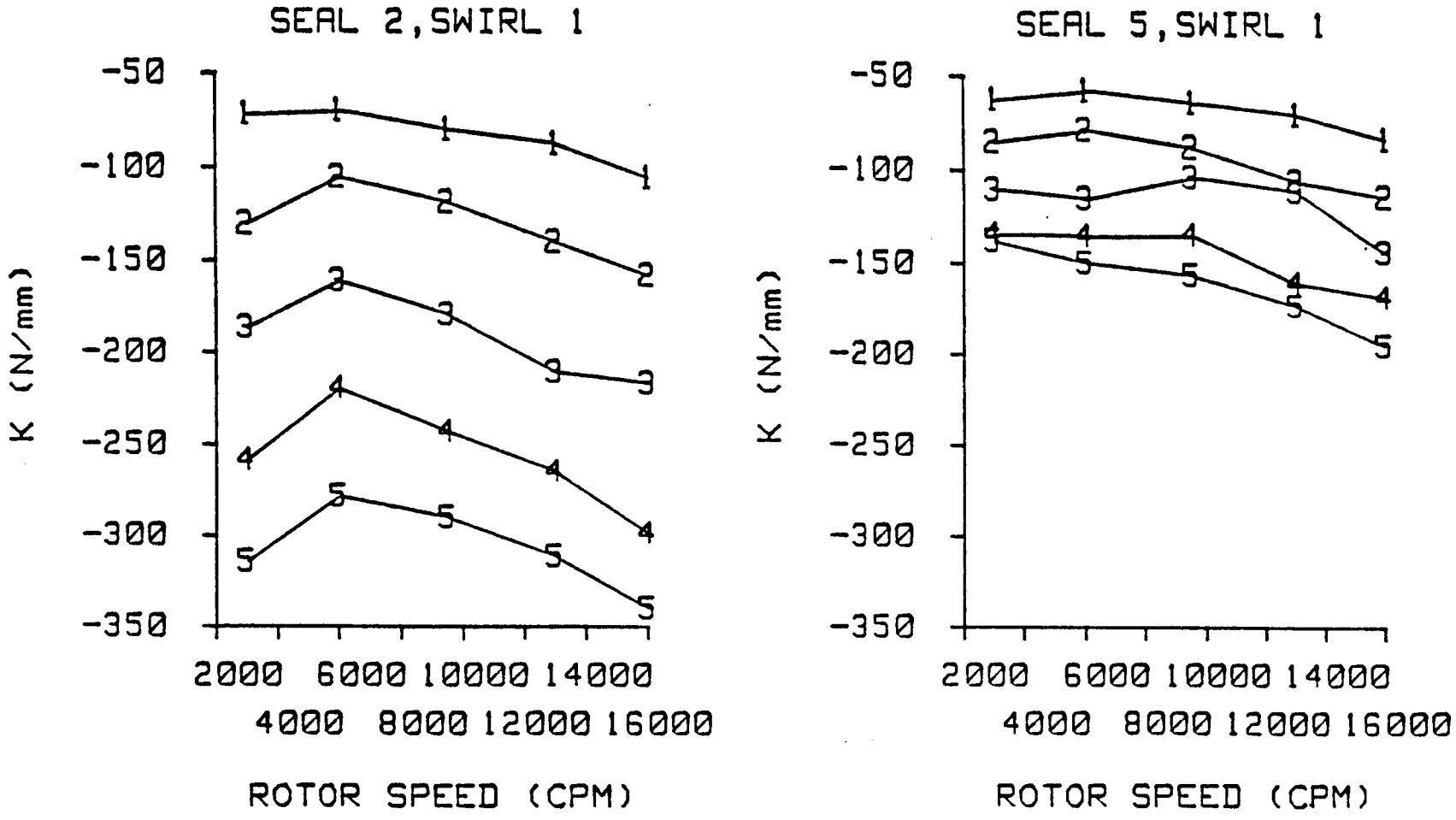

Figure A7. Direct stiffness versus rotor speed for seals 2 & 5 and inlet circumferential velocity 1. Inlet pressures 1–5 are plotted (see Table 2). Honeycomb stator (left), smooth stator (right).

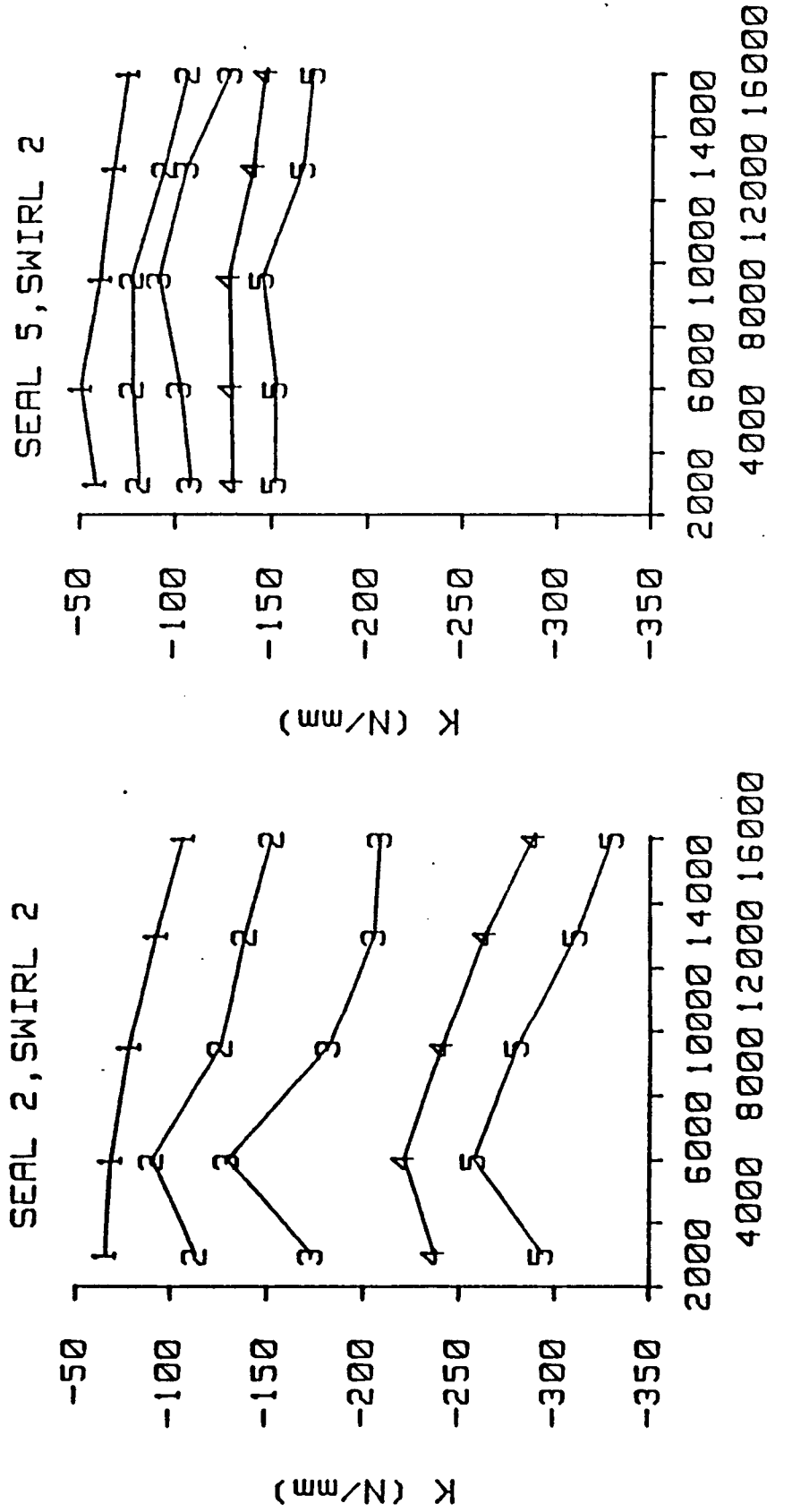

Figure A8. Direct stiffness versus rotor speed for seals 2 & 5 and inlet circumferential velocity 2. Inlet pressures 1–5 are plotted (see Table 2). Honeycomb stator (left), smooth stator (right).

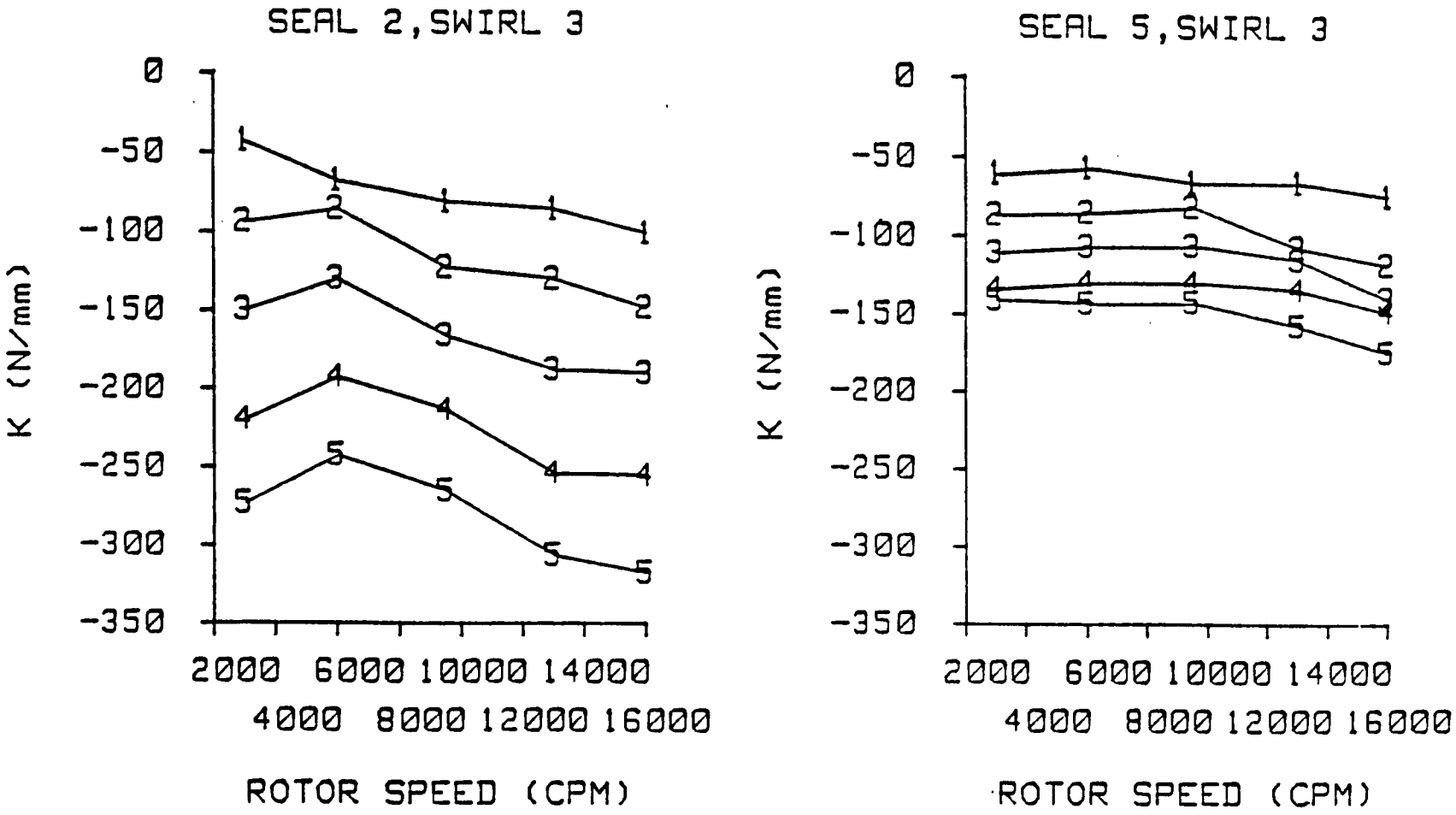

Figure A9. Direct stiffness versus rotor speed for seals 2 & 5 and inlet circumferential velocity 3. Inlet pressures 1–5 are plotted (see Table 2). Honeycomb stator (left), smooth stator (right).

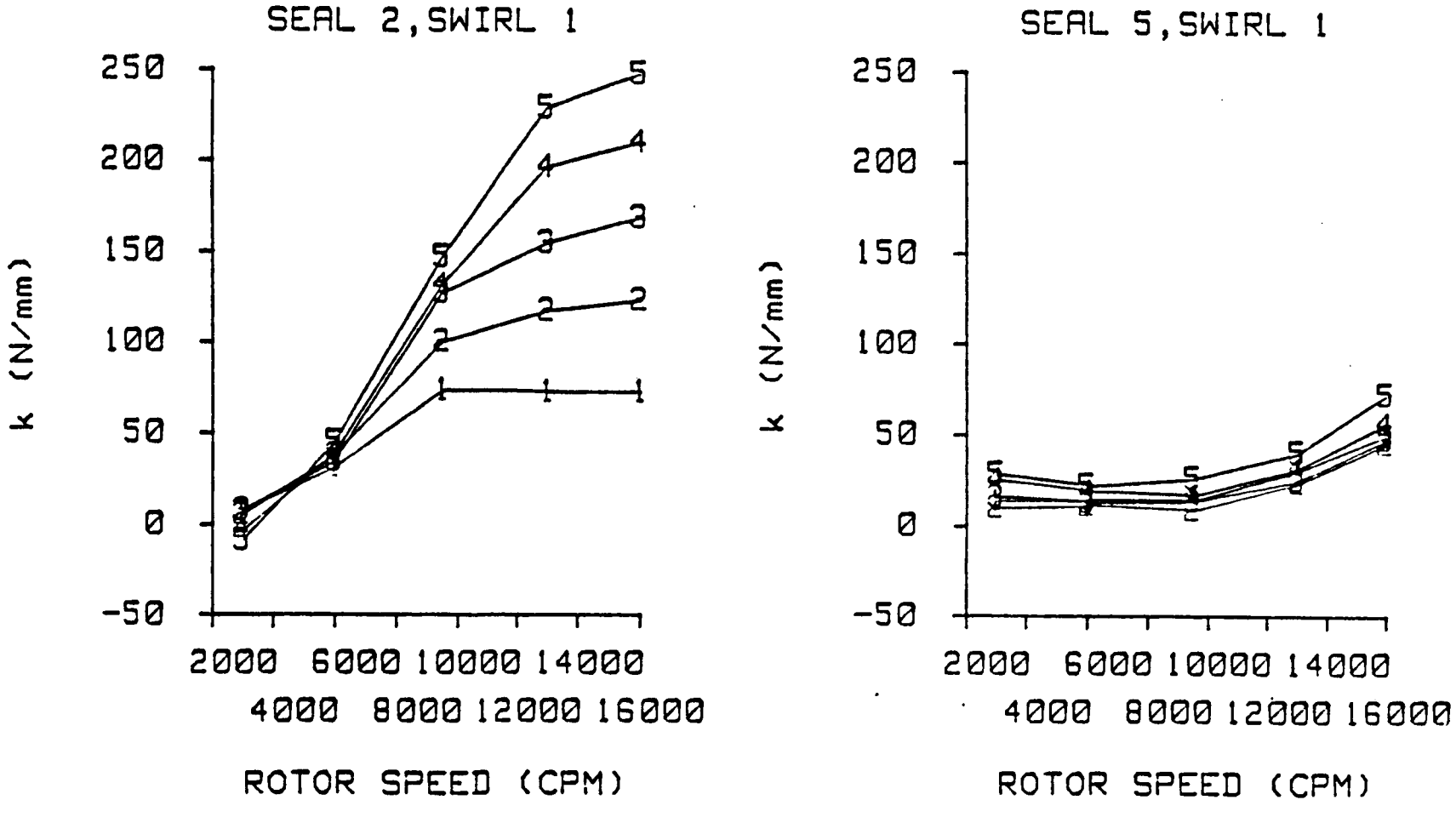

Figure A10. Cross-coupled stiffness versus rotor speed for seals 2 & 5 and inlet circumferential velocity 1. Inlet pressures 1–5 are plotted (see Table 2). Honeycomb stator (left), smooth stator (right).

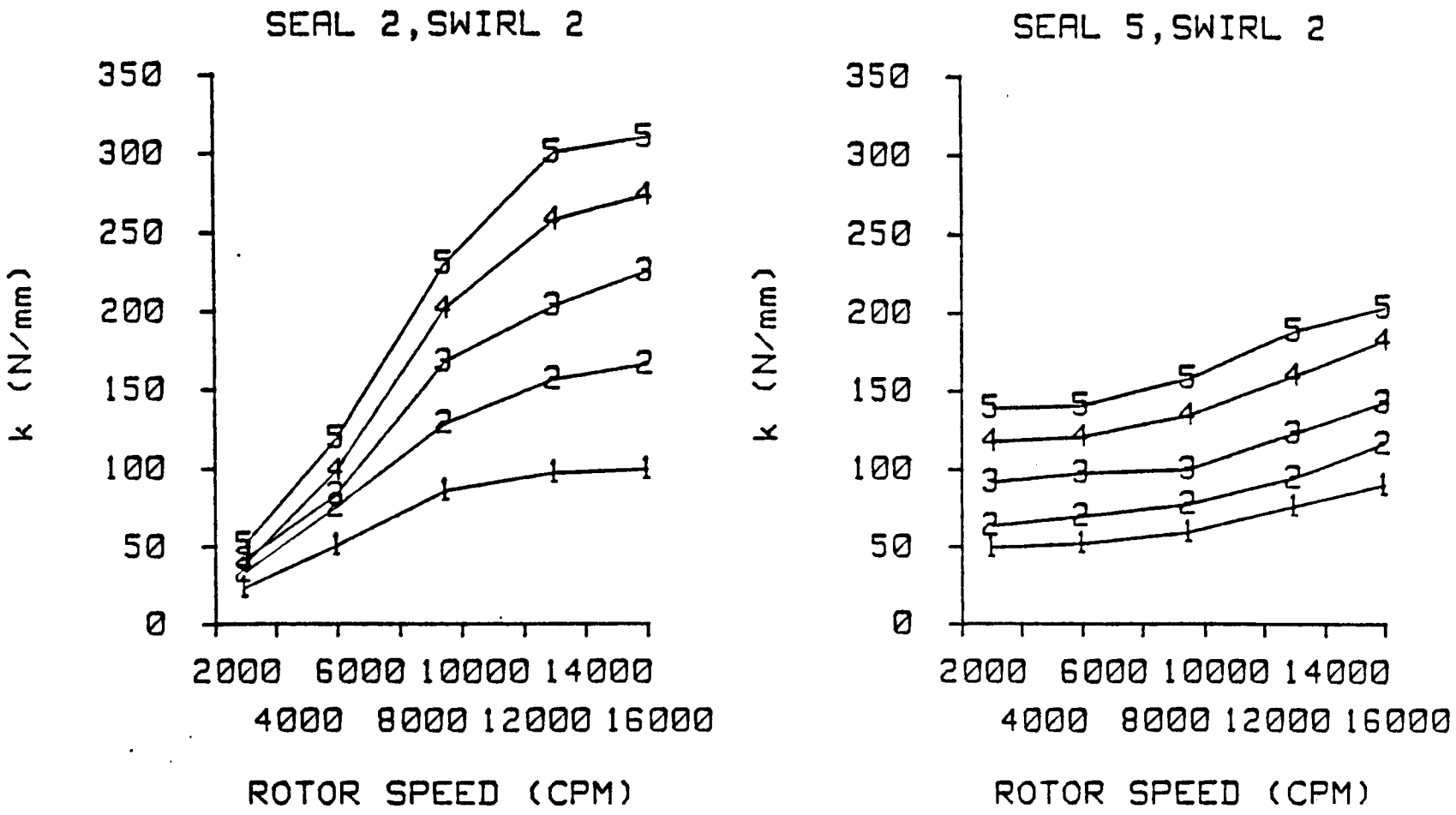

Figure A11. Cross-coupled stiffness versus rotor speed for seals 2 & 5 and inlet circumferential velocity 2. Inlet pressures 1–5 are plotted (see Table 2). Honeycomb stator (left), smooth stator (right).

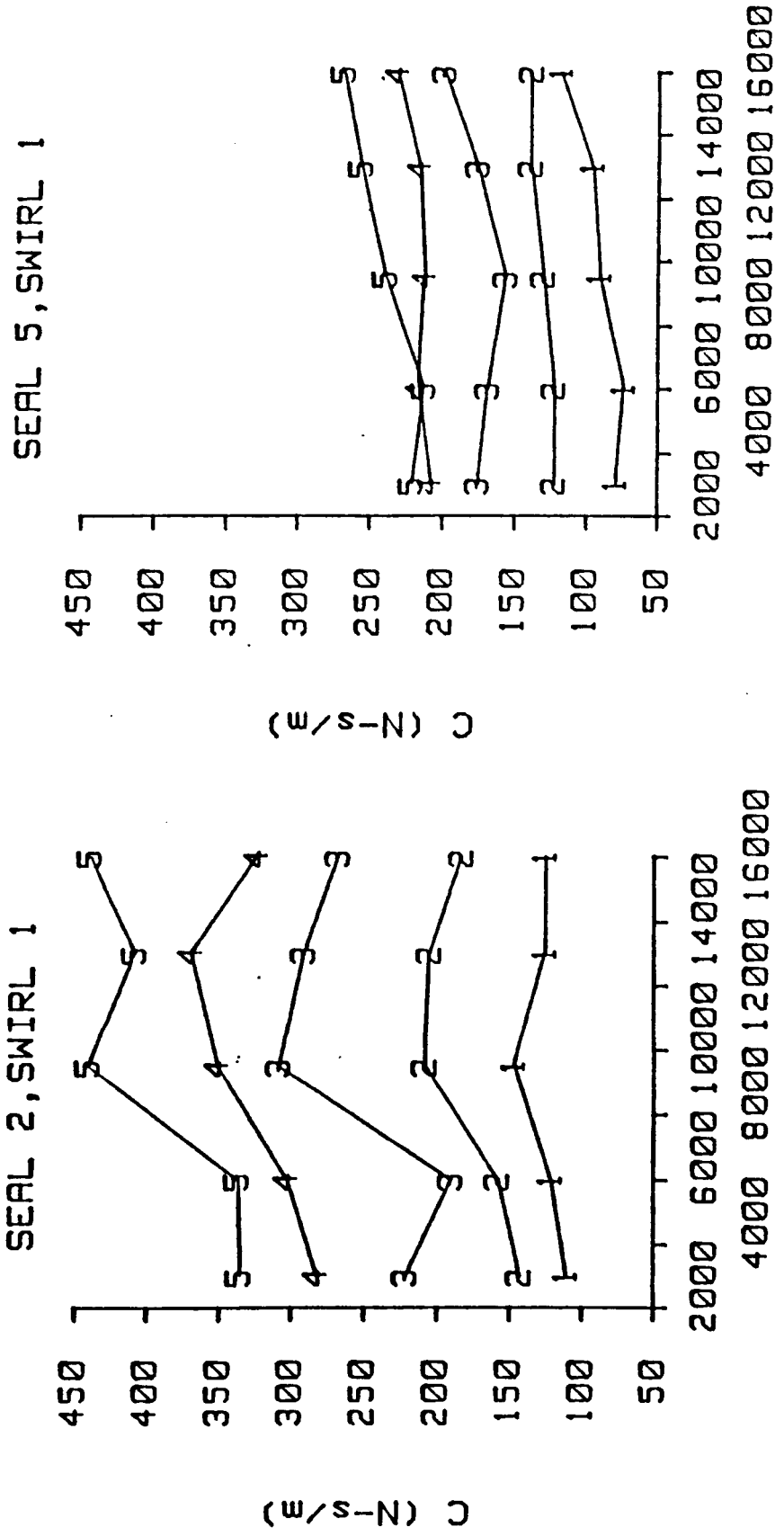

Figure A12. Direct damping versus rotor speed for seals 2 & 5 and inlet circumferential velocity 1. Inlet pressures 1–5 are plotted (see Table 2). Honeycomb stator (left), smooth stator (right).

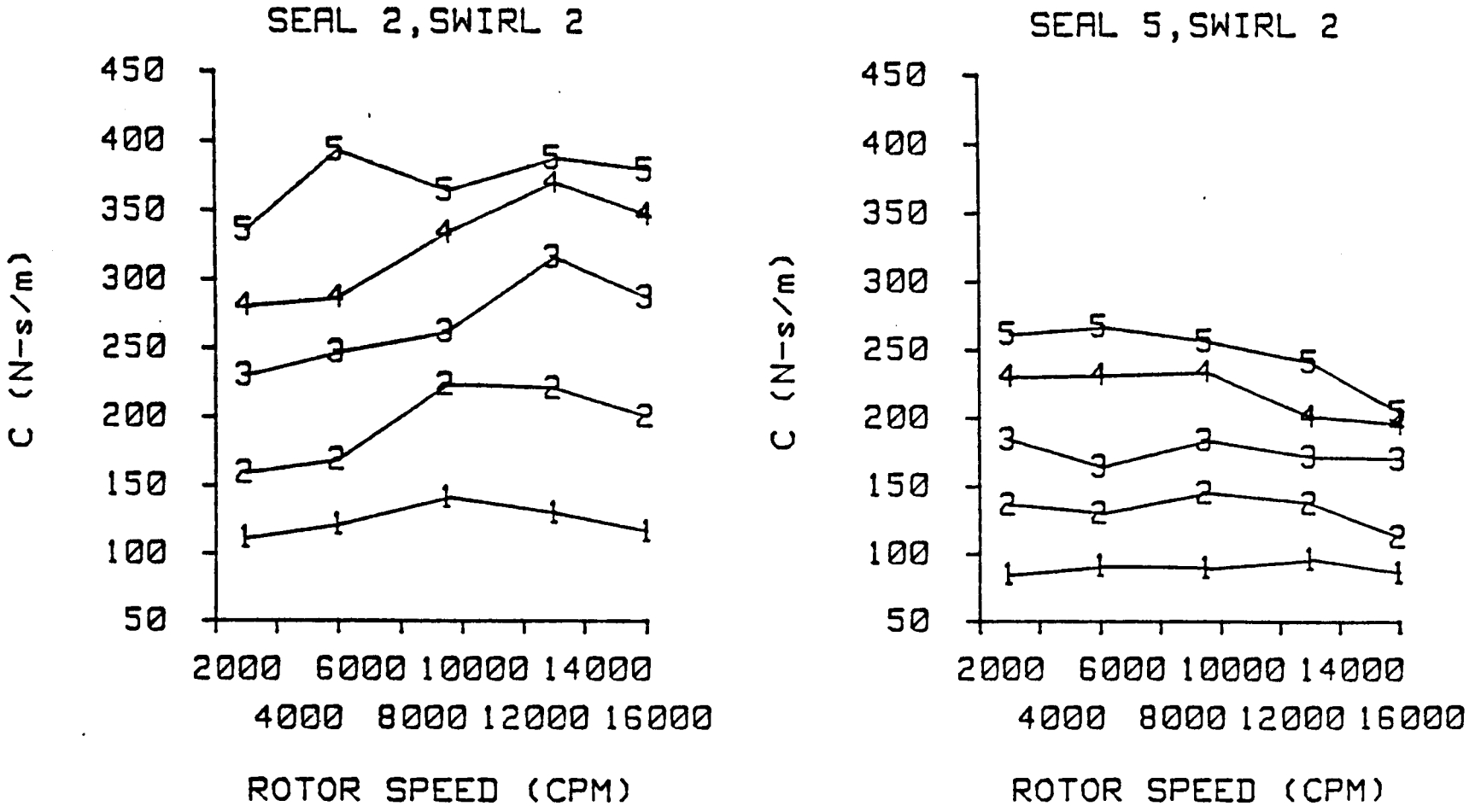

Figure A13. Direct damping versus rotor speed for seals 2 & 5 and inlet circumferential velocity 2. Inlet pressures 1–5 are plotted (see Table 2). Honeycomb stator (left), smooth stator (right).

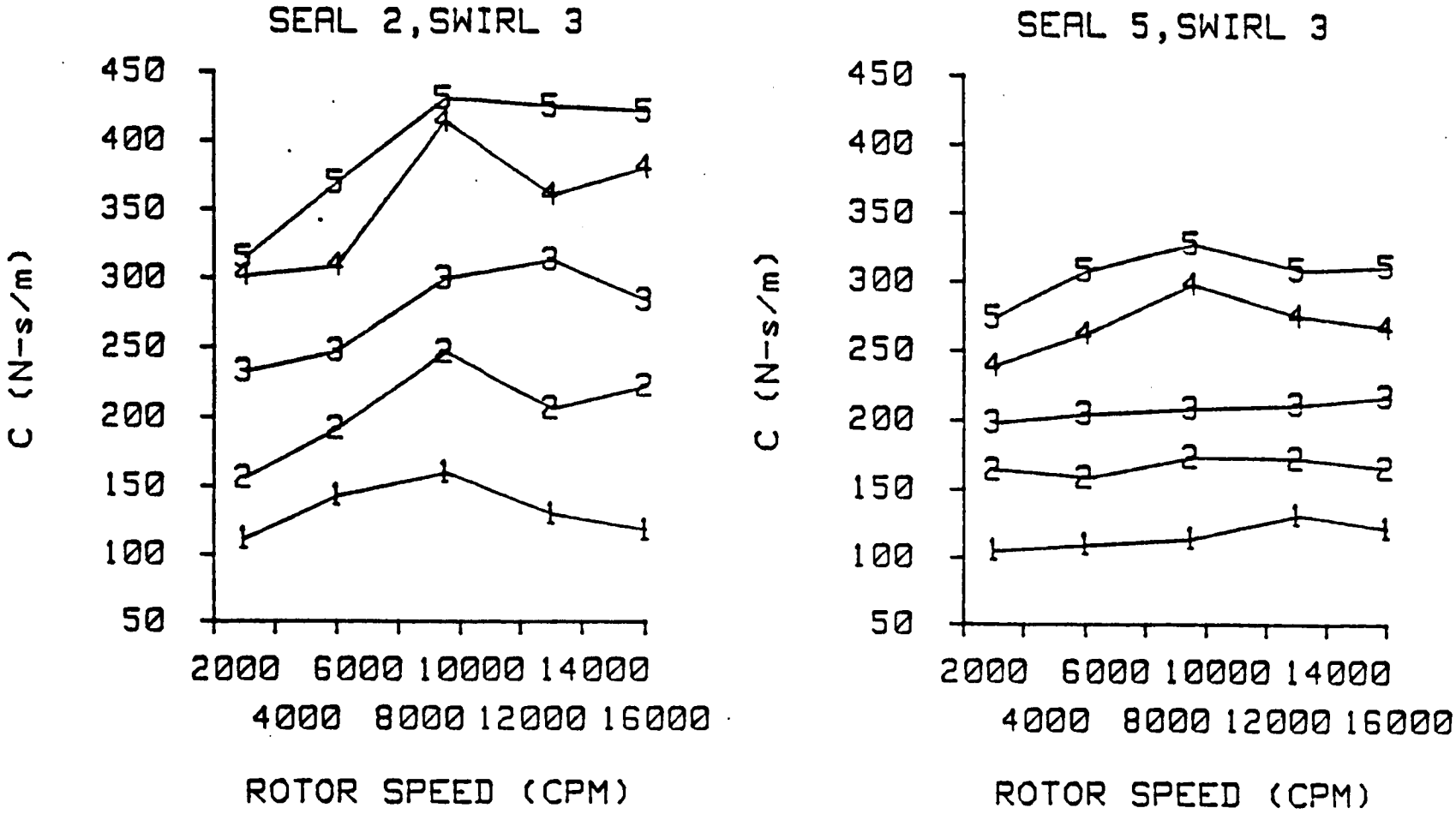

Figure A14. Direct damping versus rotor speed for seals 2 & 5 and inlet circumferential velocity 3. Inlet pressures 1–5 are plotted (see Table 2). Honeycomb stator (left), smooth stator (right).

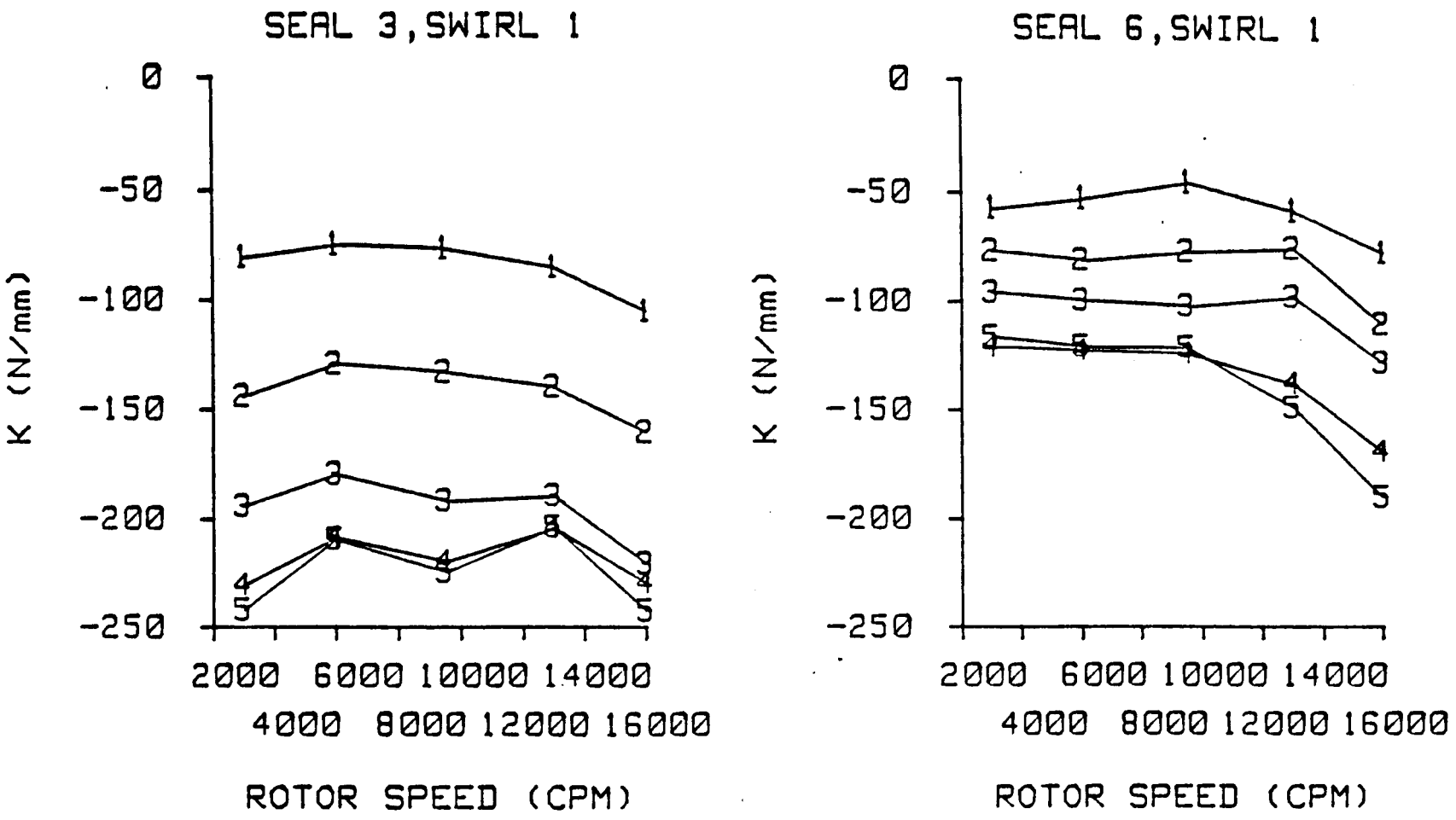

Figure A15. Direct stiffness versus rotor speed for seals 3 & 6 and inlet circumferential velocity 1. Inlet pressures 1–5 are plotted (see Table 2). Honeycomb stator (left), smooth stator (right).

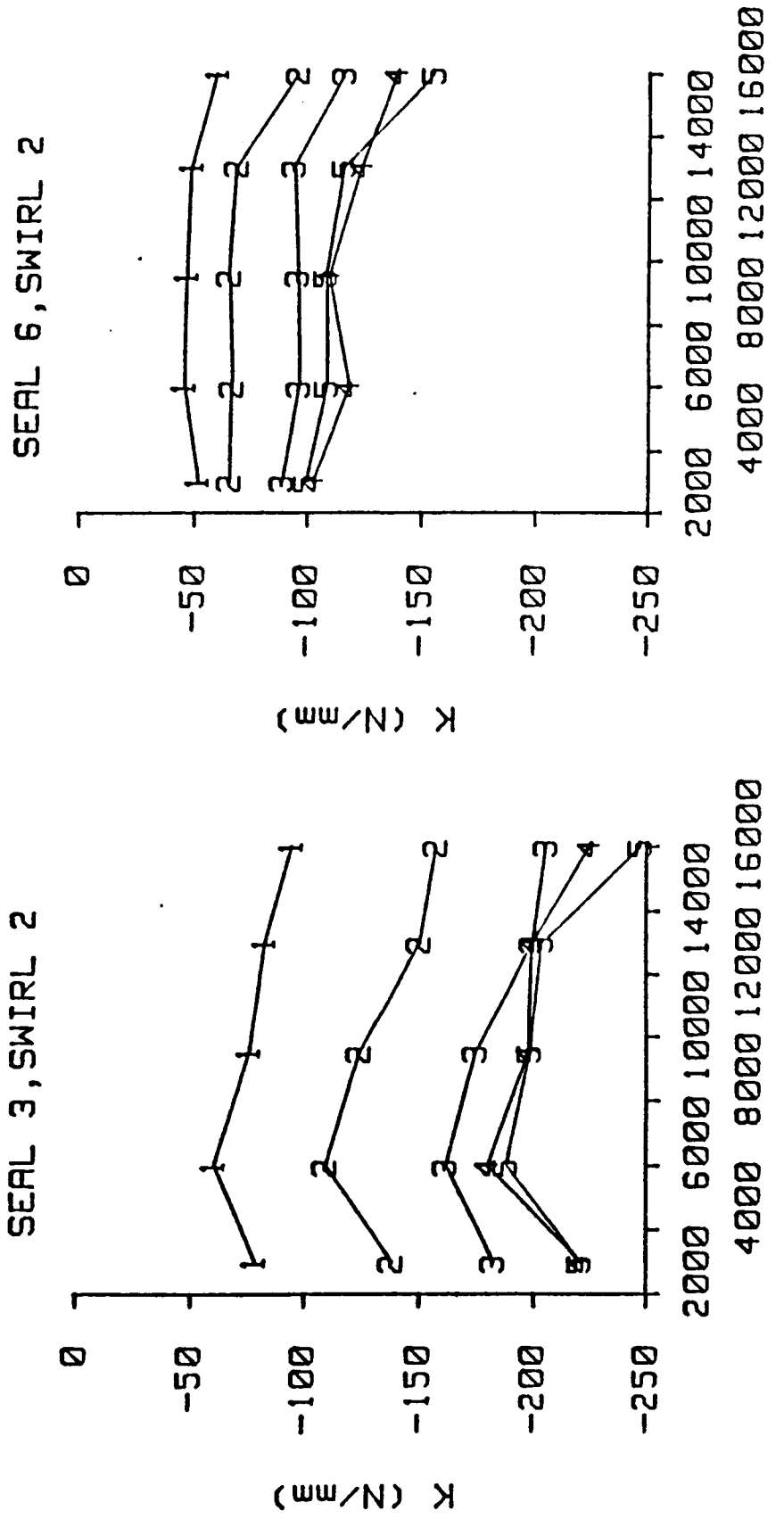

Figure A16. Direct stiffness versus rotor speed for seals 3 & 6 and inlet circumferential velocity 2. Inlet pressures 1–5 are plotted (see Table 2). Honeycomb stator (left), smooth stator (right).

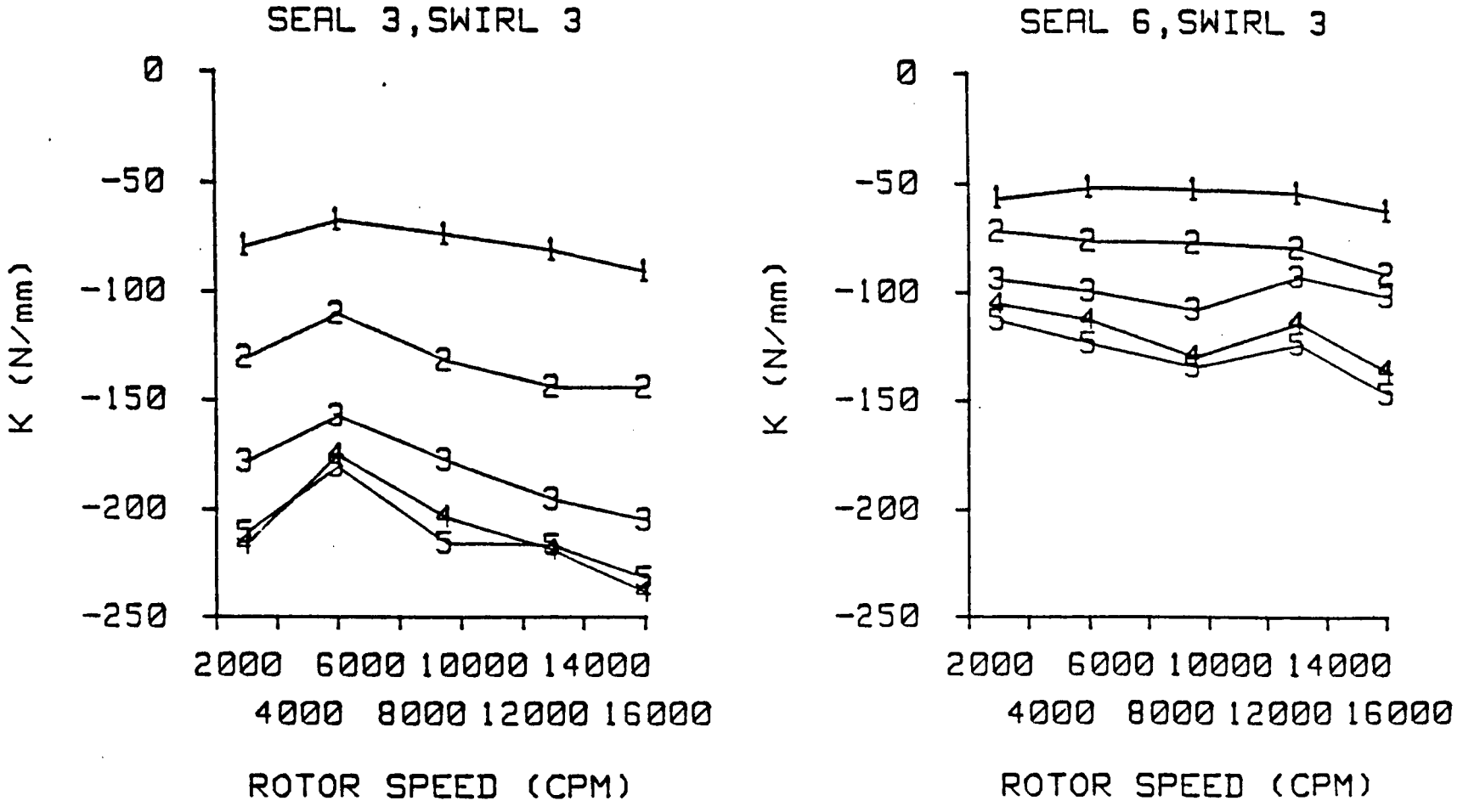

Figure A17. Direct stiffness versus rotor speed for seals 3 & 6 and inlet circumferential velocity 3. Inlet pressures 1–5 are plotted (see Table 2). Honeycomb stator (left), smooth stator (right).

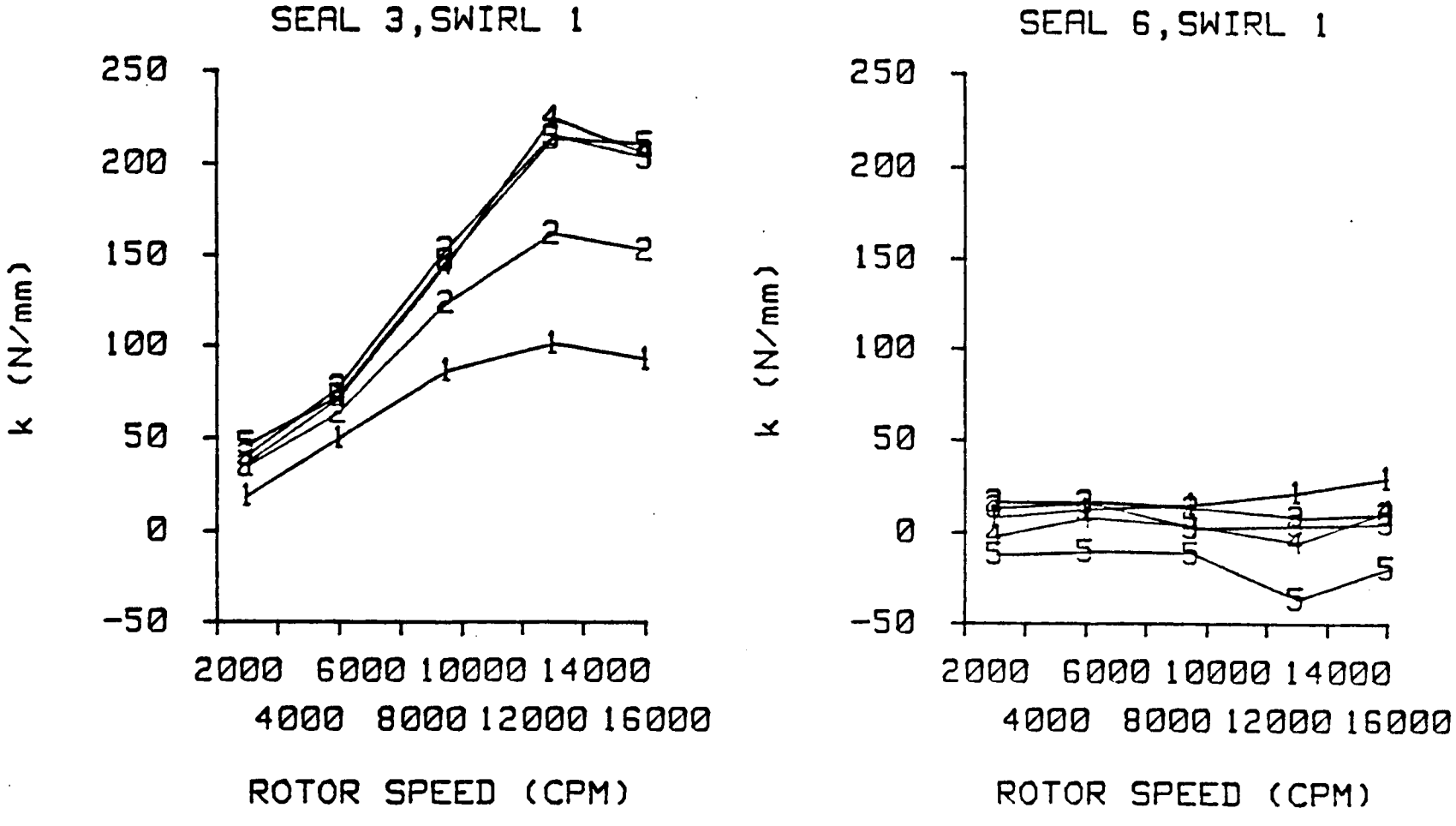

Figure A18. Cross-coupled stiffness versus rotor speed for seals 3 & 6 and inlet circumferential velocity 1. Inlet pressures 1–5 are plotted (see Table 2). Honeycomb stator (left), smooth stator (right).

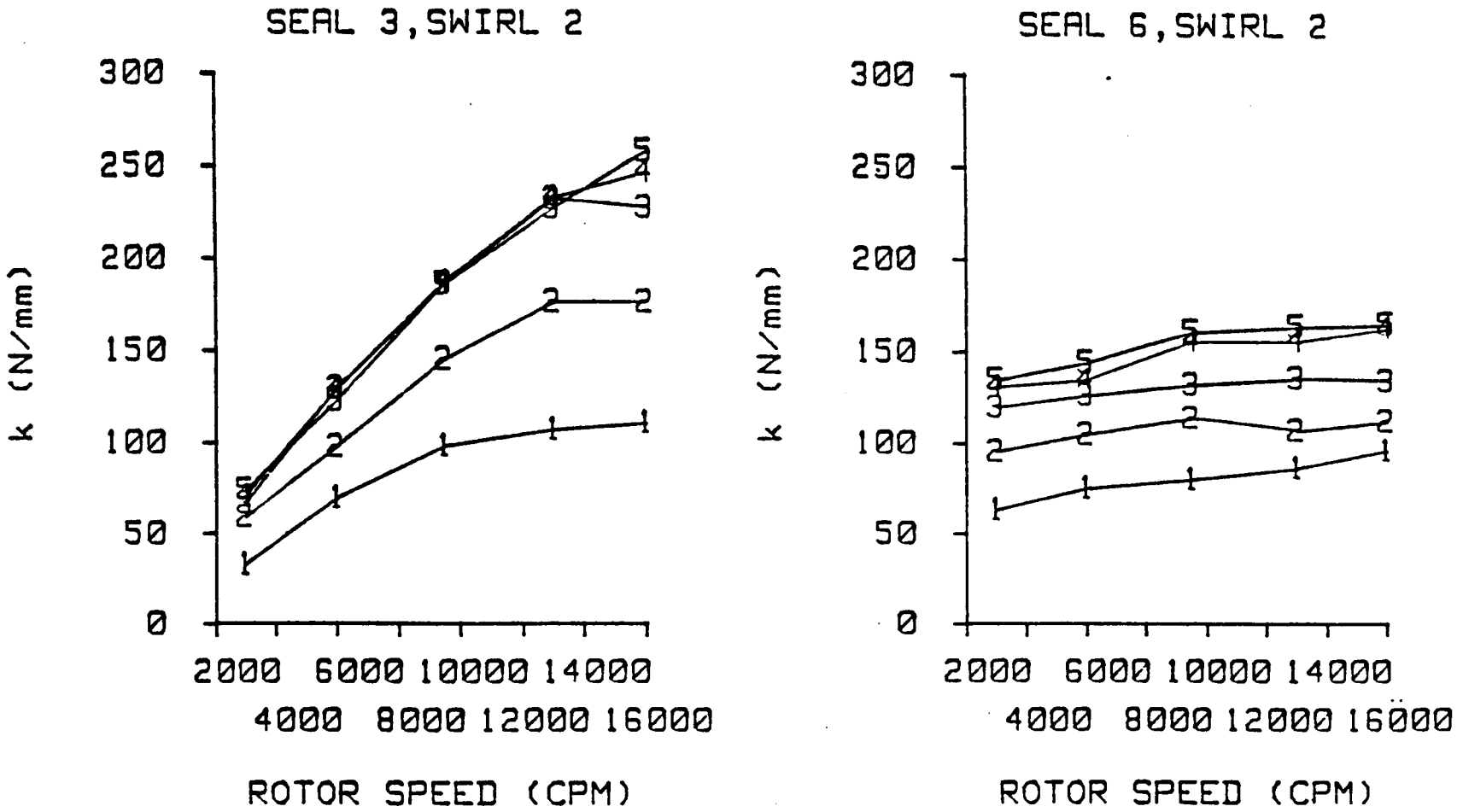

Figure A19. Cross-coupled stiffness versus rotor speed for seals 3 & 6 and inlet circumferential velocity 2. Inlet pressures 1–5 are plotted (see Table 2). Honeycomb stator (left), smooth stator (right).

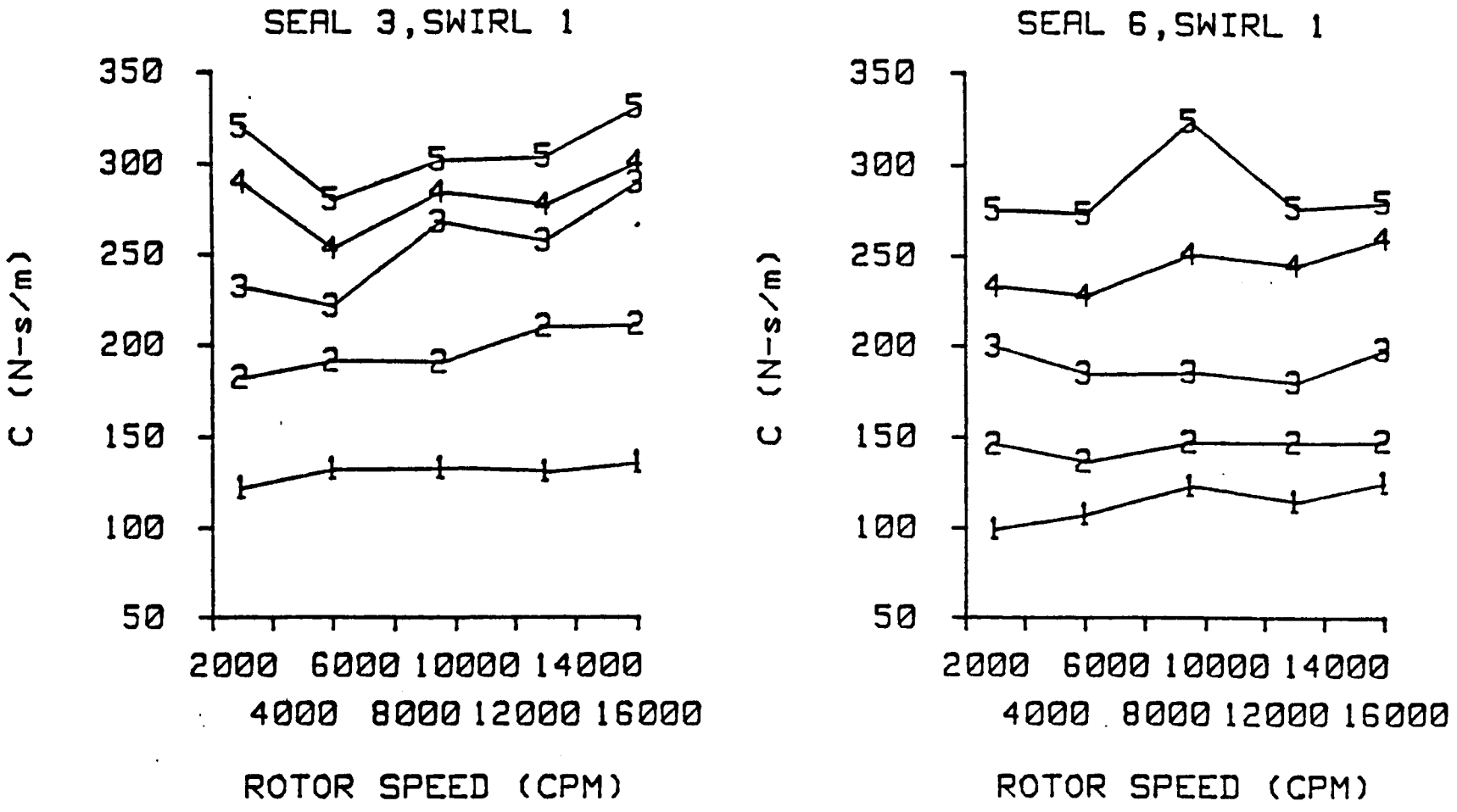

Figure A20. Direct damping versus rotor speed for seals 3 & 6 and inlet circumferential velocity 1. Inlet pressures 1–5 are plotted (see Table 2). Honeycomb stator (left), smooth stator (right).

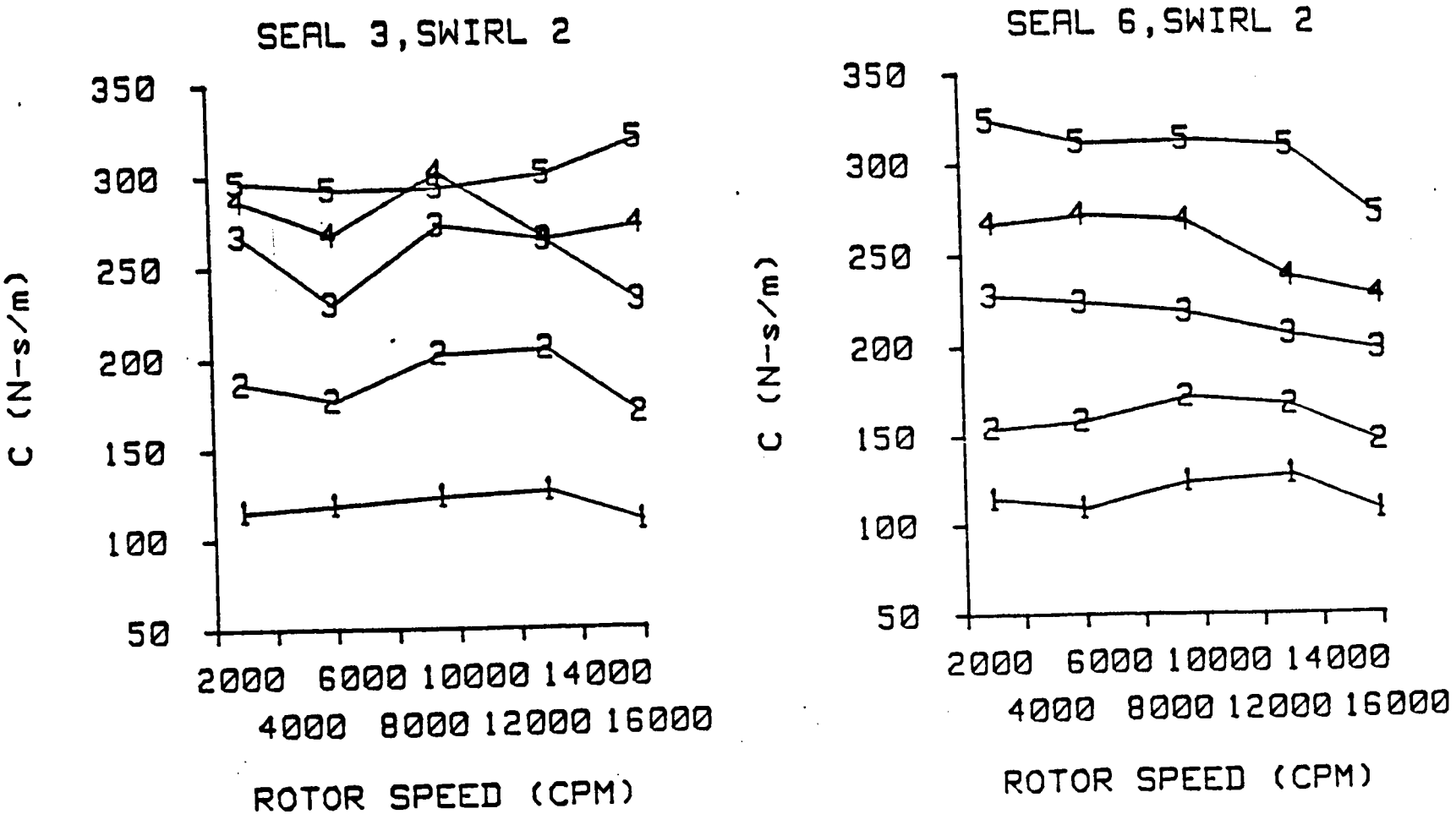

Figure A21. Direct damping versus rotor speed for seals 3 & 6 and inlet circumferential velocity 2. Inlet pressures 1–5 are plotted (see Table 2). Honeycomb stator (left), smooth stator (right).

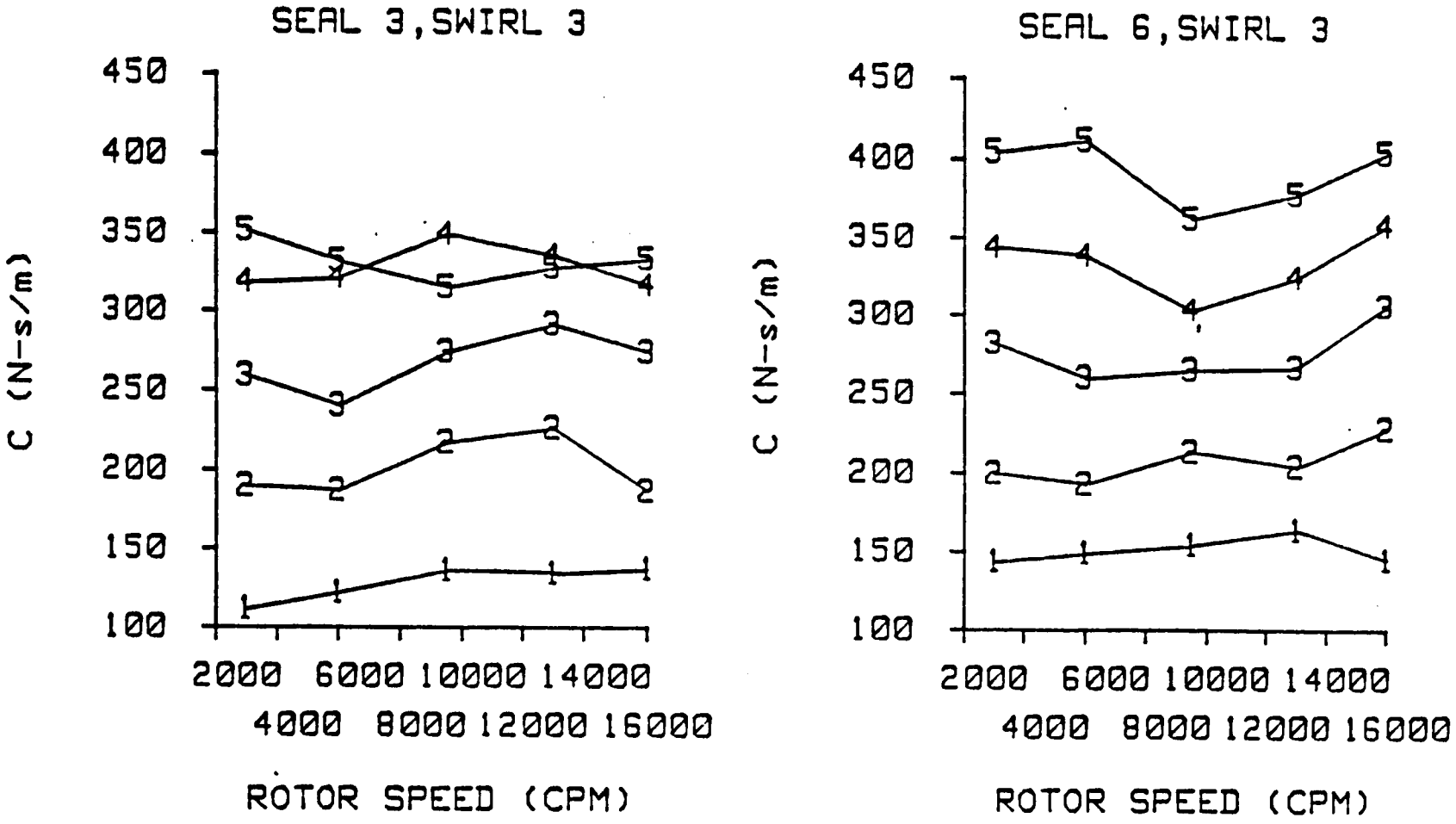

Figure A22. Direct damping versus rotor speed for seals 3 & 6 and inlet circumferential velocity 3. Inlet pressures 1–5 are plotted (see Table 2). Honeycomb stator (left), smooth stator (right).